3. SITE 1075[1]

Shipboard Scientific Party[2]

HOLE 1075A

Position: 4°47.1198′S, 10°4.4989′E

Start hole: 1950 hr, 23 August 1997

End hole: 2340 hr, 24 August 1997

Time on hole: 27.83 hr

Seafloor (drill pipe measurement from rig floor, mbrf): 3007.0

Total depth (drill pipe measurement from rig floor, mbrf): 3208.0

Distance between rig floor and sea level (m): 11.3

Water depth (drill pipe measurement from sea level, m): 2995.7

Penetration (mbsf): 201

Coring totals:
　　Type: APC
　　Number: 22
　　Cored: 201 m
　　Recovered: 213.75 m (106.34%)

Lithology:
　　Unit I: Greenish gray to olive-gray nannofossil-bearing diatomaceous clay and diatomaceous clay

HOLE 1075B

Position: 4°47.1197′S, 10°4.5025′E

Start hole: 2340 hr, 24 August 1997

End hole: 1810 hr, 25 August 1997

Time on hole: 18.50 hr

Seafloor (drill pipe measurement from rig floor, mbrf): 3006.5

Total depth (drill pipe measurement from rig floor, mbrf): 3211

Distance between rig floor and sea level (m): 11.3

Water depth (drill pipe measurement from sea level, m): 2995.2

Penetration (mbsf): 204.5

Coring totals:
　　Type: APC
　　Number: 22
　　Cored: 204.5 m
　　Recovered: 215.03 m (105.15%)

Lithology:
　　Unit I: Greenish gray to olive-gray nannofossil-bearing diatomaceous clay and diatomaceous clay

---

HOLE 1075C

Position: 4°47.1206′S, 10°4.5100′E

Start hole: 1810 hr, 25 August 1997

End hole: 1800 hr, 26 August 1997

Time on hole: 23.83 hr

Seafloor (drill pipe measurement from rig floor, mbrf): 3006.8

Total depth (drill pipe measurement from rig floor, mbrf): 3214

Distance between rig floor and sea level (m): 11.3

Water depth (drill pipe measurement from sea level, m): 2995.5

Penetration (mbsf): 207.2

Coring totals:
　　Type: APC
　　Number: 22
　　Cored: 207.2 m
　　Recovered: 213.47 m (103.03%)

Lithology:
　　Unit I: Greenish gray to olive-gray nannofossil-bearing diatomaceous clay and diatomaceous clay

Principal results: Site 1075 is the deep-water drill site on a depth transect in the Lower Congo Basin. It is located in 2995-m deep water in a complex environment dominated by (1) freshwater input from the Congo River, (2) seasonal coastal upwelling and associated filaments and eddies moving offshore, and (3) incursions of open-ocean waters, especially from the South Equatorial Countercurrent. We expect a close tie-in of climatic records from the continent and the ocean in this area. In the fan-margin deposits, the intercalation of pelagic and terrigenous information provides an excellent opportunity for studying cross-correlations of climatic effects on land and at sea. Site 1075, in connection with the upcoming two sites (1076 and 1077) in the Lower Congo Basin, will allow us to reconstruct the changing influence of Congo River, coastal upwelling, and open-ocean contributions to the dynamics of the region.

　　Three holes were cored with the advanced hydraulic piston corer (APC) at Site 1075 to a maximum depth of 207.2 meters below seafloor (mbsf), which recovered an apparently continuous interval of Pleistocene to upper Pliocene age. Hole 1075A was cored with the APC to 201.5 mbsf. Twenty-two cores were taken at Hole 1075B with the APC to a depth of 204.5 mbsf, and Hole 1075C was cored to 207.2 mbsf.

　　Sediments from Site 1075 consist of one lithostratigraphic unit composed entirely of greenish gray diatomaceous clay and nannofossil-bearing diatomaceous clay. The sediment is bioturbated and shows a gradual increase in lithification with depth but no structural or lithologic change. The sediments have overall low calcium carbonate contents of generally <2.5 wt%. Biogenic portions of the sediment contain abundant diatoms with variable amounts of nannofossils, rare silicoflagellates, siliceous sponge spicules, phytoliths, and traces of radiolarian and foraminiferal fragments. Sedimentation rates for the recovered sequence average 100 m/m.y.

　　Detailed comparisons between the magnetic susceptibility record generated on the multisensor track (MST) and high-resolution color reflectance measured with the Minolta spectrophotometer demonstrated complete re-

covery of the sedimentary sequence down to 234 meters composite depth (mcd).

Calcareous microfossils are poorly preserved, particularly in the lower section. Siliceous microfossils are relatively unaffected by dissolution and are abundant throughout Hole 1075A. An integrated, high-resolution biostratigraphy was developed for the site that is in agreement with paleomagnetic interpretations. No apparent reworking has been identified. Diatoms are represented by marine and freshwater taxa. Clay minerals show varying contributions of kaolinite. Fluctuations of freshwater diatom and phytolith assemblages and kaolinite reflect changing continental climatic conditions.

A complete magnetostratigraphy was determined at Site 1075 after alternating-field (AF) demagnetization at 20 mT. All chrons from the Brunhes (C1n) to the onset of C2n (Olduvai) at 1.95 Ma could be identified. Magnetic intensity is low and decreases with depth, although no decreasing trend was observed in the magnetic susceptibility. This suggests that the magnetic minerals that carry the remanent magnetization differ from those that dominate the magnetic susceptibility.

Interstitial water profiles record the complete consumption of sulfate at 30 mbsf, which is commensurate with increases in alkalinity and ammonium, all of which record the degradation of the abundant sedimentary organic matter. The distribution of dissolved strontium, calcium, and magnesium suggests that the uppermost 50 mbsf is a region of calcite dissolution and dolomite precipitation. A sharp 2%–3% increase in the measured values of dissolved chloride through the upper 20 mbsf appears to reflect a stacked and damped diffusional signal of glacial seawater. We found no chemical evidence of methane hydrates at any depth at Site 1075.

The average concentration of total organic carbon (TOC) is 2.6 wt%, which is rather high for ocean margin areas and reflects a history of elevated primary production in this area. The organic matter appears to be mostly marine in origin. Its microbial degradation in the sediments has fueled a sequence of redox processes. One consequence of the degradation has been the production of moderate amounts of biogenic methane and carbon dioxide and additional dissolution of calcareous sediment components within the sediment.

Physical sediment properties were determined both by high-resolution MST core logging and index properties measurements. Magnetic susceptibility and gamma-ray attenuation porosity evaluator (GRAPE) signals reveal pronounced cyclicities. The high-resolution multichannel seismic record, which was acquired during the presite survey, reveals a reflection pattern that seems to be caused by factors other than those recorded in core log data. Clathrates, dissolved gas, or pore pressure anomalies are potential explanations. High gas concentrations (CO_2 and methane) were found mainly in the interval of higher reflectivity beneath 100 mbsf.

Highlights of Site 1075 results include the complete recovery of an apparently continuous Quaternary record, with a chance for extensive reconstruction of the response of the regional system to climatic forcing. First indications are that all major Milankovitch cycles are represented within the record, but with different spectral power depending on the type of record. For example, a strong 100-k.y. signal may be present in magnetic susceptibility in the upper Quaternary, whereas a strong precessional signal appears in the red/blue ratio in sediment reflectance.

BACKGROUND AND OBJECTIVES

The Lower Congo Basin (set in the northeast corner of the Angola Basin) was the target for three drilling sites (1075, 1076, and 1077), along an east–west transect on the northern rim of the Congo Fan, off the Congo River. The regional environment is dominated by three major influences: (1) the freshwater input from the Congo River (the second largest river in the world), (2) seasonal coastal upwelling and

associated filaments and eddies moving offshore, and (3) incursions of open-ocean waters, especially from the South Equatorial Countercurrent (Fig. 1). According to Jansen (1985), river-induced phytoplankton activity extends ~160 km beyond the shelf edge, which would affect all three sites drilled, where this influence should be seen in high opal content and low-salinity diatoms (among other indicators). River-induced productivity, however, may not be the most important influence. Instead, divergence and doming, as well as cyclic interactions between the South Equatorial Countercurrent and the Benguela Current, may be the dominant factors. In the site closest to shore, the effects of seasonal coastal upwelling should be superimposed on the riverine effects.

We expect a close tie-in of climatic records from the continent and the ocean in this area. In these fan-margin deposits, the intercalation of pelagic and terrigenous information provides an excellent opportunity for studying simultaneous climatic changes on land and at sea. Previous work on Pleistocene sediments in the region (e.g., Jansen et al., 1984; Olausson, 1984; van der Gaast and Jansen, 1984; Zachariasse et al., 1984; Jansen, 1985, 1990; Jansen, et al., 1986, 1989; Jansen and van Iperen, 1991; Schneider et al., 1994, 1996, 1997) have shown that excellent records with high time resolution can be expected.

These previous investigations have clearly demonstrated that sediment records from this region reveal changes not only of the general climatic and oceanographic processes but also reflect variations based on local features, such as coastal or oceanic upwelling, river discharge, surface waters from equatorial or Southern Ocean source regions, as well as prevailing monsoonal or trade-wind influence. For example, export flux or preservation of organic carbon was enhanced during glacials in all areas along the continental margin, reflecting increased surface-water productivity under cold climate conditions off southwest Africa. In contrast, productivity records from the Angola Basin north of the Walvis Ridge reveal a strong 23-k.y. periodicity that is coherent with precessional orbital forcing, which diminishes at the Walvis Ridge (see TOC peaks at 85 and 110 k.y. in Fig. 2). This apparent decline in the 23-k.y. periodicity reflects the southward-decreasing influence of the West African Monsoon system, which modulates trade-wind zonality in step with boreal summer insolation changes and, consequently, the wind-forced coastal upwelling and open-ocean shallowing of the thermocline.

It is also evident that major productivity changes off the Congo follow the pattern determined by wind-forcing and oceanic subsurface nutrient supply rather than merely reflecting fertility changes induced by river discharge of nutrients (Schneider et al., 1994). The Congo Fan sediments are characterized by exceptionally high opal content (Müller and Schneider, 1993), about 10 times higher than that in the slope sediments recovered from elsewhere on the southwest African margin. Only off the Kunene River and on the shelf beneath the coastal upwelling area of Walvis Bay (23°S) does the opal content reach values as high as those in the Congo Fan sediments. Although these high opal values in the Congo Fan presumably are related to riverine input of silicate and to river-induced estuarine upwelling (in addition to a possible role of aluminum in enhancing preservation; van Bennekom, 1996), the opal fluctuations appear controlled by large-scale climatic patterns, judging from the presence of Milankovitch cycles (Fig. 3).

The three sites drilled in the transect allow us to reconstruct the changing influence of Congo River, coastal upwelling, and open-ocean contributions to the dynamics of the region. The influences of these competing subsystems will respond differently to forcing by the dominant climatic cycles (100, 41, 23, and 19 k.y.). The relative strength of the main climate controls (e.g., sea level and general planetary temperature gradient compared with cold water advection and monsoonal variations) should be revealed by spectral analysis. It will
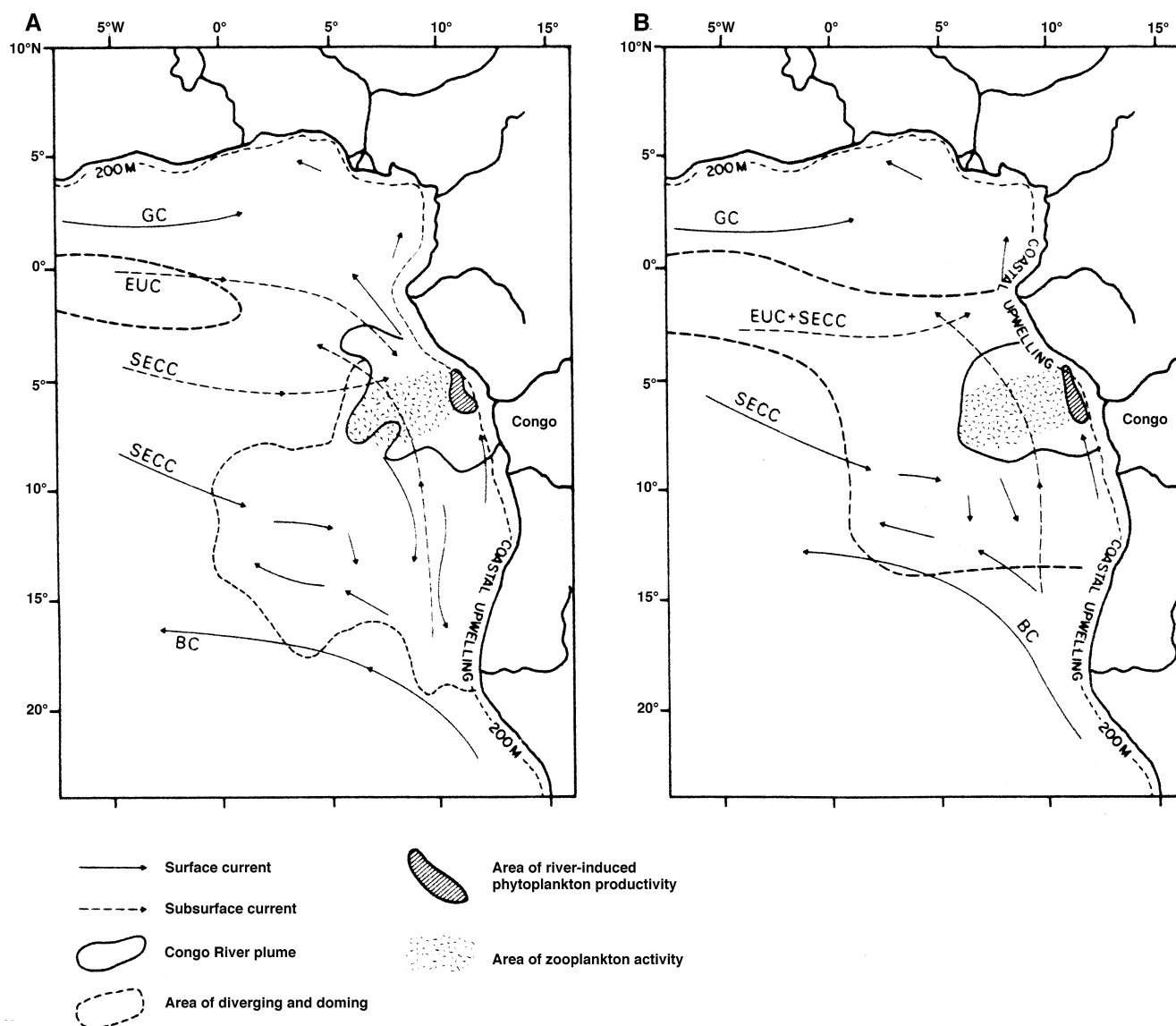
Figure 1. (**A**) Interglacial and (**B**) glacial contrast in the Angola Basin, reflected in the more or less distinct shifts in subsystem boundaries (from Jansen, 1985). BC = Benguela Current; GC = Guinea Current; SECC = South Equatorial Countercurrent; EUC = Equatorial Undercurrent.

be interesting to see how these various controls modify continental climate, particularly within the Congo drainage basin.

OPERATIONS

Las Palmas to Site 1075

The last line in Las Palmas (Canary Islands) cleared the dock at 2000 hr local time on 12 August 1997. The 3019-nmi sea voyage to proposed site LCB-1 took 11 days at an average speed of 11.6 kt. The vessel speed was enhanced by favorable currents (Canary and the Equatorial Countercurrent) and calm environmental conditions. The *JOIDES Resolution* crossed the equator at zero degrees longitude at 0613 hr on 21 August. After a short seismic survey, a Datasonics 354M beacon was deployed at Site 1075 at 1950 hr on 21 August.

Hole 1075A (Proposed Site LCB-1)

Hole 1075A was spudded at 0450 hr on 24 August. The recovery of 1.50 m of sediment established the seafloor depth at 2995.7 meters below sea level (mbsl) by drill-pipe measurement (DPM). APC Cores 175-1075A-1H through 22H were taken from 0 to 201.0 mbsf (Table 1; also see expanded core summary table on CD-ROM, back pocket, this volume), with 201.0 m cored and 215.2 m recovered (106.3% recovery). Cores were oriented starting with Core 4H. The drill string was pulled back, and the bit cleared the mudline at 2340 hr on 24 August, thereby ending Hole 1075A.

Hole 1075B

The vessel was offset 10 m to the east, and Hole 1075B was spudded at 0040 hr on 25 August. The first core indicated a water depth of
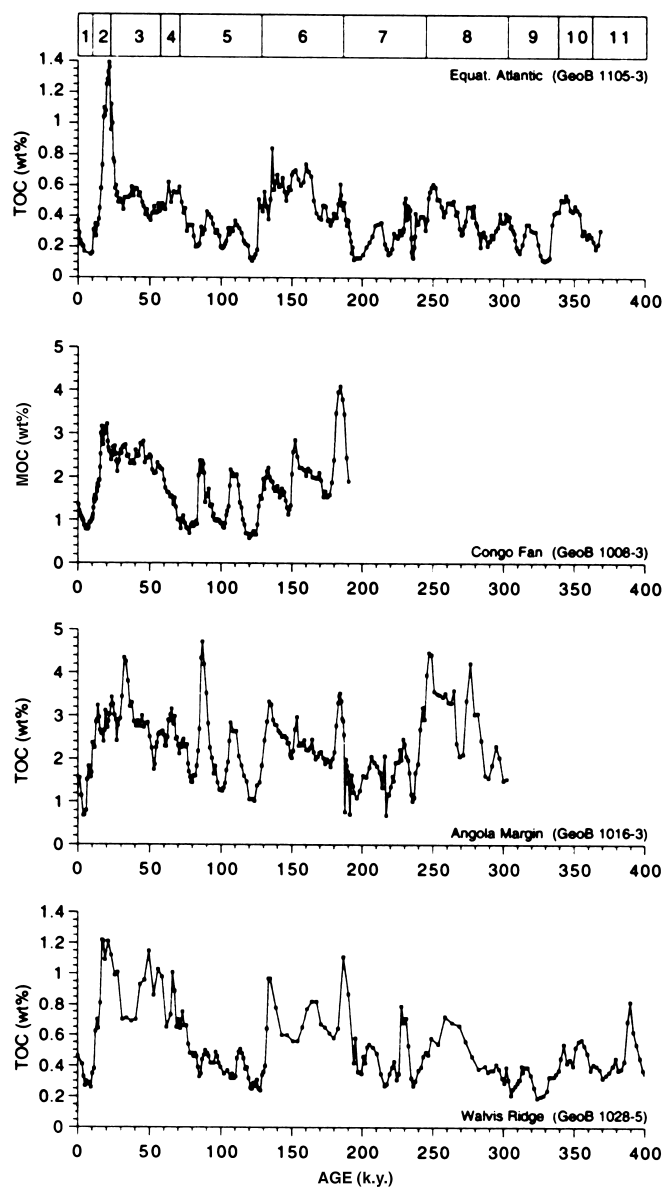
Figure 2. Time series of TOC contents (in weight percent) in late Quaternary sediments in the east-equatorial South Atlantic. MOC = the portion of marine organic carbon estimated from $\delta^{13}C_{org}$ for the Congo Fan core GeoB 1008-3 (from Schneider et al. 1996). The numbers inside the box represent isotope Stages 1–11.

2995.2 mbsl by DPM. APC Cores 175-1075B-1H through 22H were taken from 0 to 204.5 mbsf (Table 1), with 204.5 m cored and 215.0 m recovered (105.1% recovery). Cores were oriented starting with Core 4H. The drill string was pulled back with the bit clearing the mudline at 1810 hr on 25 August, thereby ending Hole 1075B.

Hole 1075C

The vessel was offset another 10 m to the east where the third hole of the site was spudded with the APC at 1855 hr on 25 August. The seafloor depth of Hole 1075C was determined at 2995.5 mbsl by DPM. After coring 22 APC cores (Table 1), the hole was terminated after reaching the depth objective of 207.2 m with 103.0% recovery. Cores were oriented starting with Core 3H. The bit cleared the seafloor at 1220 hr on 26 August. As the drill string was being pulled out

of the hole, the beacon was released and recovered, and the hydrophones and thrusters were retracted and secured.

SITE GEOPHYSICS

Introduction and Strategy

The drill sites in the Lower Congo Basin at ~5°–6°S latitude were the northernmost sites of Ocean Drilling Program (ODP) Leg 175, during which six working areas along the southwest African continental margin were drilled to study the evolution of the Benguela Current system in the late Neogene. To explain the strategy of the site survey (Bleil et al., 1995) a short summary of the evidence existing to date is given regarding the expected sedimentary structures at this part of the continental margin.

The survey area (Fig. 4) is located off the mouth of the Congo River, which is the second largest river of the world with respect to water discharge (Peters, 1978; Eisma and van Bennekom, 1978). Deposition in the Congo Fan area is characterized by significant sediment influx from the continent. A major proportion of the sediment is transported through the Congo Canyon directly into the deep sea (Heezen et al., 1964; Shepard and Emery, 1973; van Weering and van Iperen, 1984; Droz et al., 1996). The canyon extends far into the lower stretches of the river, with water depths of several hundred meters already inshore (Peters, 1978; Eisma and Kalf, 1984). The sediment is guided through the shelf and accumulates in small basins. From time to time, these materials are released and move down the canyon. The narrow, and in some sections more than 1000 m deep, channel opens into the Congo Cone at a water depth below 3000 m, where typical fan deposits and channel/levee systems are commonly associated with chaotic sedimentary structures.

The selection of drill sites in the original proposal was oriented along the seismic Line 62 of Emery et al. (1975), but the data quality was not sufficient to identify fine-scale sedimentary structures and establish the absence of disturbances. Also, we wished to survey the area in greater detail and with higher resolution using digital multichannel seismic lines. Six crossings were derived from analog online seismic records of Lines GeoB (Geosciences Bremen)/AWI 93-001 and 93-002 and were later all proposed as potential drill sites (Fig. 4).

Bathymetric survey data show that the seafloor is rather smooth in the working area. The lower Congo Cone is disrupted, however, by numerous small and a few larger distributary channels. Upslope, the general character of the seafloor changes between 3500 and 2500 m water depth from a rough, diffracting surface to a continuous layering with numerous parallel internal reflectors. No indications of channels, downslope transport, or slumping were found in the surface sediments shallower than 2500 m water depth.

Seismostratigraphy

Altogether, nine seismic lines were recorded in the northern Congo Fan area, with six crossings at potential drill sites in water depths between 1400 and 3000 m (Fig. 4). Connecting profiles will later allow a regional seismic correlation. The first line (GeoB/AWI 93-001; Fig. 5) started at 8°30′E/5°30′S to cover the depositional environment of the fan, particularly its change toward a predominantly (hemi-) pelagic sedimentation at the continental slope.

The area of the seismic survey generally shows similar overall acoustic characteristics. The southern Line GeoB/AWI 93-001 has basically recorded the same features as Line 62 of Emery et al. (1975). The basement near the continent is deeply buried, and no salt diapirs are observed close to the surface. Deep reflectors are undulating, however, indicating minor deformation of deeper layers by salt movement or an early tectonism. These undulations are smoothed out toward the surface and do not control the ocean-floor morphology.
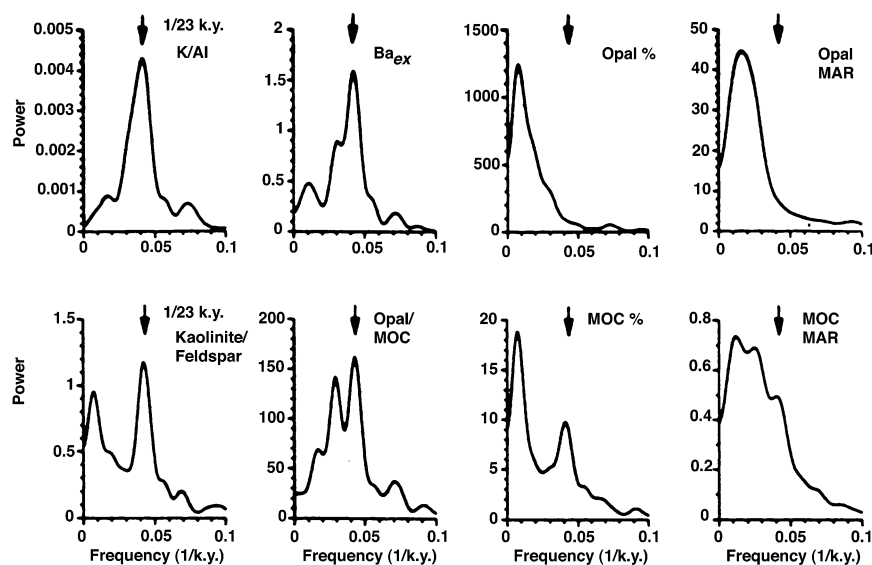
Figure 3. Spectral estimates for harmonic variance in the records of terrigenous river input (kaolinite/feldspar and K/Al ratios), bulk oceanic productivity (barium excess [Ba$_{ex}$], marine organic carbon [MOC] weight percent, and mass accumulation rate [MAR]), opal productivity (opal weight percent and MAR), and excess siliceous productivity (opal/MOC) from the Congo Fan core GeoB 1008-3. Black arrows = precessional frequency band (from Schneider et al., 1997).

On Line GeoB/AWI 93-002 (Fig. 6), which is about 25 nmi farther to the north, intense salt diapirism is apparent, and numerous disturbed sequences are observed near the surface. For this reason, the crossing lines were concentrated on those sections of Lines GeoB/AWI 93-001 and 93-002 where penetration was high and a distinct layering was observed. The general seismostratigraphic characteristics are given in Uenzelmann-Neben et al. (1997) and will be summarized here for the part of the sedimentary column that was cored at Sites 1075 to 1077.

In the survey area, the characteristic pattern of fan deposits has completely disappeared in the upper sedimentary column. Two seismostratigraphic units can be identified in the range of the drill holes. They are distinguished mainly by their reflection amplitudes and reflector coherence, but lack distinct reflectors. These seismostratigraphic units are described below.

Seismostratigraphic Unit 1

Seismostratigraphic Unit 1 is characterized by low reflection amplitudes and a few, partially coherent, weak reflectors. The thickness varies between 100 and 160 ms two-way traveltime (TWT; ~80 to ~120 m). The base of the unit reveals a transition from a completely transparent interval to higher reflection amplitudes. The sedimentary column appears to be heavily faulted. Digital echosounder data, however, indicate only minor vertical offsets of a few meters. The seismic unit commonly cuts across reflectors; the unit represents a zone of modified reflector amplitudes.

Seismostratigraphic Unit 2

Seismostratigraphic Unit 2 shows higher reflection amplitudes, which are still weaker than the surface reflector. The base of the unit is more affected by the undulating deeper structures than its top, which may be caused by differential subsidence and higher sediment accumulation in the "topographic" lows. Accordingly, the thickness varies significantly from 220 to 350 ms TWT (~160 to ~260 m). Because of the pronounced changes in reflectivity, it cannot be excluded that either the top or the base of Unit 2 is an unconformity. Seismic Unit 2 is split, being separated by one or two thin transparent bands (one on Line GeoB/AWI 93-001 and two on Line GeoB/AWI 93-002).

After the safety panel review, only 200 m of drilling was allowed for each of the proposed sites in the Lower Congo Basin area. There-fore, deeper seismostratigraphic units could not be reached by drilling during Leg 175. At the greater depths, evidence was found both in multichannel seismic and digital echosounder data for the existence of gas, gas hydrate, fluid migration, and microfaulting through the entire area. The identification of seismic units based on average reflection amplitudes can be affected by these components. Amplitudes show a strong lateral variation and in many cases do not reflect lithologic boundaries. Commonly, nearly vertical transparent zones are seen in the vicinity of small faults and surface depressions, which in some cases appear as pockmarks.

The basic assumption that the margin is not receiving sediment via distributary channels of the Congo Fan could be confirmed by the seismic survey. Only hemipelagic deposits were found, and slumps or debris flows seem to be absent in the upper sedimentary column. The sedimentation rate appears to be nearly constant within the area and is more influenced by local effects such as subsidence and diapirism.

Seven potential drill sites had been identified in the Upper Congo Fan area north of the Congo Canyon in water depths between 1400 and 3000 m. Six were finally proposed and were approved for drilling down to 200 mbsf. They all represent a similar depositional environment at varying distances to the shelf break and at different water depths and positions with respect to the Congo River plume. Cross profiles were shot for five sites.

Site 1075

Site 1075 is located at the northwestern corner of the survey area, farthest from the river mouth (common depth point [CDP] 9750 of Line GeoB/AWI 93-002) in 2995 m water depth. A crossing single-channel seismic line was shot during the approach to the site with the onboard equipment of the *JOIDES Resolution* to assure the absence of high-amplitude layers indicative of potential gas accumulations. No evidence was found for gas accumulation. Figure 7 shows a 10-km-long seismic section of Line GeoB/AWI 93-002 in the vicinity of Site 1075. Weak reflectors were enhanced by normalization of amplitudes to a constant value. Therefore, the transition between the low reflective seismic Unit 1 and the higher reflective Unit 2 at 150 ms TWT does not appear as pronounced. The figure clearly shows that numerous (weak) reflectors can be found in the upper, mostly transparent unit (Fig. 6). Most reflectors are coherent in the section, but have interruptions that are attributed to small faults. Site 1075 was located between two of those faults to avoid a discontinuous section.

Table 1. Coring summary for Site 1075.

Core	Date (Aug 1997)	Time (UTC)	Interval (mbsf)	Length cored (m)	Length recovered (m)	Recovery (%)
175-1075A-						
1H	24	0500	0.0-1.5	1.5	1.50	100.0
2H	24	0555	1.5-11.0	9.5	9.77	102.8
3H	24	0635	11.0-20.5	9.5	9.95	104.7
4H	24	0725	20.5-30.0	9.5	9.84	103.6
5H	24	0810	30.0-39.5	9.5	10.00	105.3
6H	24	0855	39.5-49.0	9.5	10.00	105.3
7H	24	0935	49.0-58.5	9.5	10.02	105.5
8H	24	1020	58.5-68.0	9.5	10.12	106.5
9H	24	1105	68.0-77.5	9.5	10.24	107.8
10H	24	1145	77.5-87.0	9.5	10.21	107.5
11H	24	1240	87.0-96.5	9.5	9.60	101.1
12H	24	1330	96.5-106.0	9.5	10.33	108.7
13H	24	1420	106.0-115.5	9.5	10.18	107.2
14H	24	1510	115.5-125.0	9.5	10.24	107.8
15H	24	1600	125.0-134.5	9.5	10.26	108.0
16H	24	1650	134.5-144.0	9.5	10.04	105.7
17H	24	1742	144.0-153.5	9.5	10.25	107.9
18H	24	1825	153.5-163.0	9.5	10.10	106.3
19H	24	1925	163.0-172.5	9.5	10.22	107.6
20H	24	2015	172.5-182.0	9.5	10.57	111.3
21H	24	2105	182.0-191.5	9.5	10.17	107.1
22H	24	2155	191.5-201.0	9.5	10.14	106.7
Coring totals:				201.0	213.75	106.3
175-1075B-						
1H	25	0055	0.0-5.0	5.0	5.06	101.2
2H	25	0135	5.0-14.5	9.5	8.34	87.8
3H	25	0215	14.5-24.0	9.5	8.27	87.1
4H	25	0305	24.0-33.5	9.5	9.80	103.2
5H	25	0350	33.5-43.0	9.5	9.91	104.3
6H	25	0430	43.0-52.5	9.5	9.23	97.2
7H	25	0515	52.5-62.0	9.5	10.22	107.6
8H	25	0555	62.0-71.5	9.5	10.19	107.3
9H	25	0650	71.5-81.0	9.5	10.07	106.0
10H	25	0735	81.0-90.5	9.5	10.16	106.9
11H	25	0815	90.5-100.0	9.5	10.18	107.2
12H	25	0900	100.0-109.5	9.5	10.25	107.9
13H	25	0940	109.5-119.0	9.5	10.29	108.3
14H	25	1025	119.0-128.5	9.5	10.12	106.5
15H	25	1115	128.5-138.0	9.5	10.48	110.3
16H	25	1155	138.0-147.5	9.5	10.39	109.4
17H	25	1245	147.5-157.0	9.5	10.27	108.1
18H	25	1335	157.0-166.5	9.5	10.59	111.5
19H	25	1425	166.5-176.0	9.5	10.12	106.5
20H	25	1510	176.0-185.5	9.5	10.69	112.5
21H	25	1600	185.5-195.0	9.5	10.49	110.4
22H	25	1645	195.0-204.5	9.5	9.91	104.3
Coring totals:				204.5	215.03	105.2
175-1075C-						
1H	25	1915	0.0-7.7	7.7	7.70	100.0
2H	25	1955	7.7-17.2	9.5	9.53	100.3
3H	25	2045	17.2-26.7	9.5	9.64	101.5
4H	25	2130	26.7-36.2	9.5	6.11	64.3
5H	25	2215	36.2-45.7	9.5	6.59	69.4
6H	25	2305	45.7-55.2	9.5	10.06	105.9
7H	26	0005	55.2-64.7	9.5	10.09	106.2
8H	26	0050	64.7-74.2	9.5	10.17	107.1
9H	26	0135	74.2-83.7	9.5	10.20	107.4
10H	26	0220	83.7-93.2	9.5	10.17	107.1
11H	26	0300	93.2-102.7	9.5	10.27	108.1
12H	26	0345	102.7-112.2	9.5	10.12	106.5
13H	26	0430	112.2-121.7	9.5	10.14	106.7
14H	26	0510	121.7-131.2	9.5	10.40	109.5
15H	26	0555	131.2-140.7	9.5	10.21	107.5
16H	26	0640	140.7-150.2	9.5	10.14	106.7
17H	26	0725	150.2-159.7	9.5	10.24	107.8
18H	26	0810	159.7-169.2	9.5	10.21	107.5
19H	26	0850	169.2-178.7	9.5	10.19	107.3
20H	26	0935	178.7-188.2	9.5	10.18	107.2
21H	26	1020	188.2-197.7	9.5	10.67	112.3
22H	26	1105	197.7-207.2	9.5	10.44	109.9
Coring totals:				207.2	213.47	103.0

Notes: UTC = Universal Time Coordinated. An expanded version of this coring summary table that includes lengths and depths of sections and comments on sampling is included on CD-ROM (back pocket, this volume).

The transition to seismic Unit 2, however, is marked by a reflector of higher amplitude. Most faults can be traced down to the base of Unit 2.

Figure 8 shows a close-up of about 1-km length from the vicinity of the drill site in comparison with the wet bulk density profile for Hole 1075A, plotted against sub-bottom depth for a sound velocity of 1500 m/s. Seismograms are plotted as wiggle traces with gray-scaled amplitudes as background. The lateral amplitude changes can be clearly identified, as well as the transition between seismic Units 1 and 2 at ~85 mbsf. Numerous reflectors can be correlated with changes in wet bulk density. Velocity variation is expected to be <40 m/s (<3%) and therefore can be disregarded as the main origin of acoustic impedance changes, compared with density variations of as much as 20%. An explanation for the mostly transparent upper seismic unit from the density log is not evident, although changes are generally small in the upper unit and increase with depth.

It is clear from the comparison that the main frequency of the seismic signal is not sufficiently high to resolve individual changes in the downhole physical properties and, therefore, changes in interference from consecutive layers occur. Calculation of synthetic seismograms from calibrated and spliced GRAPE data sets is required for more detailed analyses. The required thorough editing and quality control can only be carried out on shore.

Site 1076

Site 1076 is the shallowest site in the transect, with a water depth of 1403 m at the southeastern edge of the survey area. Figure 9 shows a 10-km-long section of seismic Line GeoB/AWI 93-001 close to the drill site at CDP 22,990. From this site, the hemipelagic sequence can be correlated to the other sites. At greater depth, disturbed intervals, hyperbolic echoes, and vertical amplitude anomalies can be identified in the unmigrated seismic section at a distance of several kilometers. The reflectors appear coherent, however, within 1 km around the drill site on the scale of this seismic image.

At the drill site, the two seismic units within a mostly undisturbed sequence can be clearly distinguished with a transition at 160 ms TWT. Reflectors of seismic Unit 2 show a toplap with Unit 1, which might be caused either by an erosional contact or by an overprint of reflection amplitudes in Unit 1.

The close-up section of 1-km length in the vicinity of the drill site is shown in Figure 10. A transition between the mostly transparent seismic Units 1 and 2 occurs between 110 and 140 mbsf, with lateral variation of reflection amplitudes. A comparison with the wet bulk density profile derived from index properties measurements (see "Physical Properties" section, "Site 1076" chapter, this volume) allows the assignment of sharp density changes to several reflectors, although a unique solution cannot be provided at this time because of the limited resolution of the data set and the limited quality of the available core log data. Further refinement will be achieved with the calculation of synthetic seismograms in shore-based studies.

Biostratigraphic data (see "Biostratigraphy and Sedimentation Rates" section, "Site 1076" chapter, this volume) revealed a break in continuous deposition at about 120 mbsf, which could be associated with the observed toplap interval. Alternatively, a nearby fault zone with a 10-m vertical offset could explain a missing interval at Site 1076. Because of the low reflection amplitudes in the upper seismic unit, further processing is required to elucidate the seismic features at the depth of the identified hiatus.

Site 1077

Site 1077 lies between Sites 1075 and 1076 on seismic Line GeoB/AWI 93-001 at CDP 17,000 in 2381 m water depth. This site
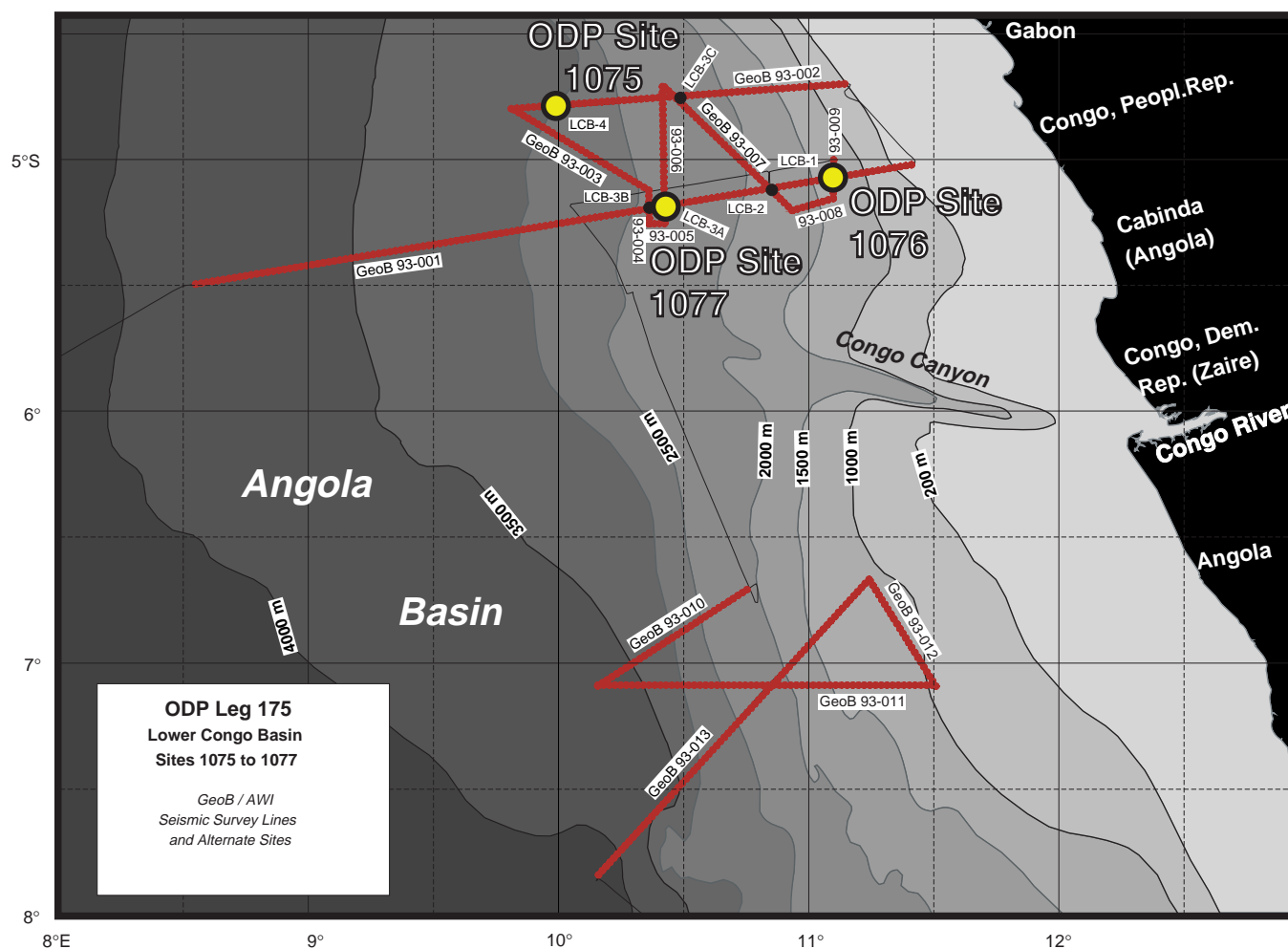
Figure 4. Map of seismic presite survey lines, proposed site locations, and ODP Leg 175 drill Sites 1075 to 1077 in the Lower Congo Basin. Bathymetry was derived from Gebco Digital Dataset on CD-ROM.

was used specifically to investigate the origin of the acoustic transparent interval (perhaps indicating the presence of gas hydrate) with a limited suite of downhole logging tools (see "Downhole Logging" section, "Site 1077" chapter, this volume) and a detailed high-resolution sampling for interstitial water analyses across the crucial interval.

Figure 11 shows a 10-km-long section of seismic Line GeoB/AWI 93-001 around the drill site. Seismic Units 1 and 2 are clearly identified with a transition at 120 ms TWT. Besides several coherent reflectors of several kilometers extent within Unit 1, a strong reflector that was not found at the other two sites is present at 40 ms TWT. The transitional zone between both seismic units is characterized by a completely transparent band of ~10-ms TWT thickness.

Figure 12 shows a close-up of 1-km length in the vicinity of the drill site compared with a density profile derived from downhole logging, which is available beneath 76 mbsf. This data set is in very good agreement with GRAPE density logs measured on whole cores, although GRAPE density reveals pronounced minima at core breaks beneath 50 mbsf because of gas expansion. The wet bulk density profile derived from index properties measurements (see "Physical Properties" section, "Site 1077" chapter, this volume) shows a gradual increase down to 100 mbsf, with less scatter than beneath this depth. However, these density changes alone probably cannot ex-

plain the distinct difference in reflection amplitudes. The existence of gas hydrate at layers within the section was tested as a possible explanation for higher reflection amplitudes by detailed high-resolution pore-water analyses (see "Inorganic Geochemistry" section, "Site 1077" chapter, this volume). No evidence for gas hydrate was found. The gas content in the sediment, which was first observed in high concentration at ~50 mbsf, will be further investigated as a potential cause for a decrease in amplitudes.

Downhole logging information from density, velocity, and temperature also confirmed the absence of massive clathrate layers. Although the instruments were operating at their limits of resolution in these sediments with high porosity, the derived density and velocity profiles compare well with core and discrete measurements and can be further used for precise calculation of synthetic seismograms.

LITHOSTRATIGRAPHY

Introduction

Three holes with a maximum penetration of 201 mbsf were drilled at Site 1075 (Fig. 13). In the upper 50 m of all three holes, the sediments had a distinct hydrogen sulfide smell, suggesting bacterial oxidation of organic matter. Below 50 mbsf, the hydrogen sulfide smell
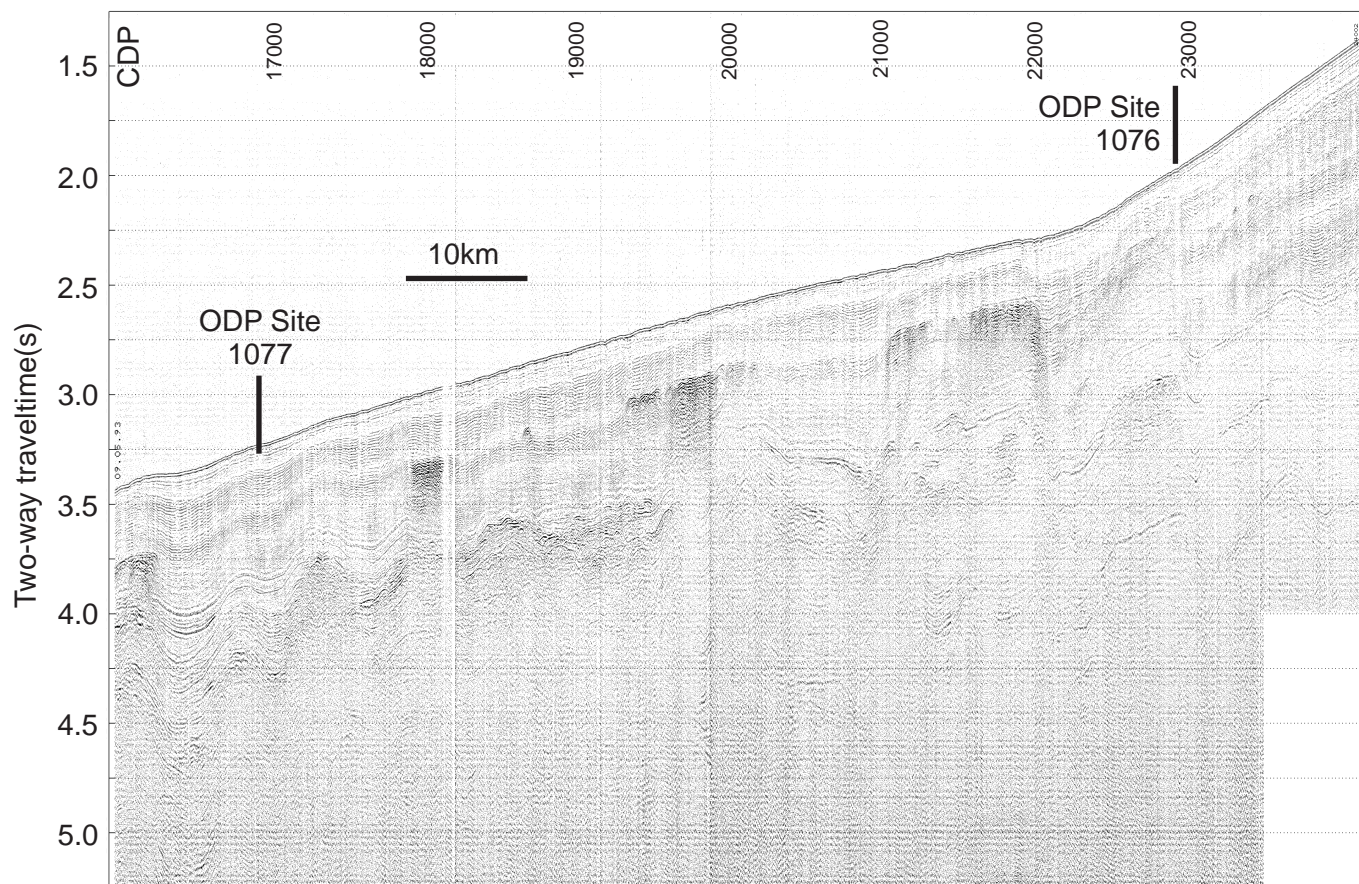
Line GeoB/AWI 93-001

Figure 5. Seismic Line GeoB/AWI 93-001 with Sites 1076 and 1077. Vertical axis is given in two-way traveltime. CDP interval is 12.5 m for a shotpoint spacing of 25 m. Seismic data is twelvefold stacked and not migrated. Site 1076 is located at CDP 22,990; Site 1077 at CDP 17,000.

gradually disappeared. Many cores contain gas voids that were produced by the release of carbon dioxide trapped in the sediment (see "Organic Geochemistry" section, this chapter).

Description of Lithostratigraphic Unit

The lithostratigraphic description for the sedimentary sequence from Site 1075 is based on data from the following sources: (1) visual core description, (2) smear-slide examination, (3) color reflectance measurements, (4) bulk calcium carbonate measurements, and (5) X-ray diffraction (XRD) measurements.

Sediments from Site 1075 form one lithostratigraphic unit composed entirely of greenish gray (5GY 5/1) to olive-gray (5Y 3/2) nannofossil-bearing diatomaceous clay and diatomaceous clay (Fig. 13). Most of the sediment is moderately to extensively bioturbated. Bioturbation is most clearly seen as mottled intervals in which there is a change in sediment color. Visual examination of the sediments revealed that subtle color changes are common throughout the core. A sharp color change in Section 175-1075C-5H-3 accompanies the appearance of nannofossils (Fig. 14). The sediments become increasingly compacted downhole. No change in lithology was observed. The sediments have overall low calcium carbonate contents of generally <2.5 wt% $CaCO_3$ (see "Organic Geochemistry" section, this chapter). Between 40 and 100 mbsf, narrow intervals have calcium carbonate contents as high as 17.3 wt%. Evidence from smear-slide and micropaleontological analyses suggests that increases in the abundance of nannofossils and/or foraminifers are responsible for the increase in $CaCO_3$ (see "Biostratigraphy and Sedimentation Rates" section, this chapter).

Synthesis of Smear-Slide Analyses

Smear-slide analyses indicate that the clastic component is dominated by clay minerals with trace amounts of quartz and feldspar. Biogenic portions of sediments contain abundant diatoms (10%–35%) with variable amounts of nannofossils (0%–10%), rare silicoflagellates, siliceous sponge spicules, phytoliths, and traces of radiolarian and foraminiferal fragments.

Authigenic components are dominated by the ubiquitous presence of iron sulfides, primarily in the form of disseminated pyrite and framboidal pyrite, confirming the process of bacterial sulfate reduction (see "Inorganic Geochemistry" section, this chapter). Framboidal pyrite is also frequently found in the tests of diatom shells. Rare, friable whitish gray nodules, possibly phosphatic, are disseminated throughout the core. Nodules range in diameter from 1 to 3 mm and envelope the surrounding sediment. Small shell fragments are present in many intervals.

X-ray Diffraction Analysis

The XRD patterns of Hole 1075A represent five major minerals: smectite, kaolinite/illite, quartz, calcite, and pyrite. The smectites are generally poorly crystallized. Shipboard XRD spectra for Site 1075 are not precise enough to determine the smectite crystallinity. Van
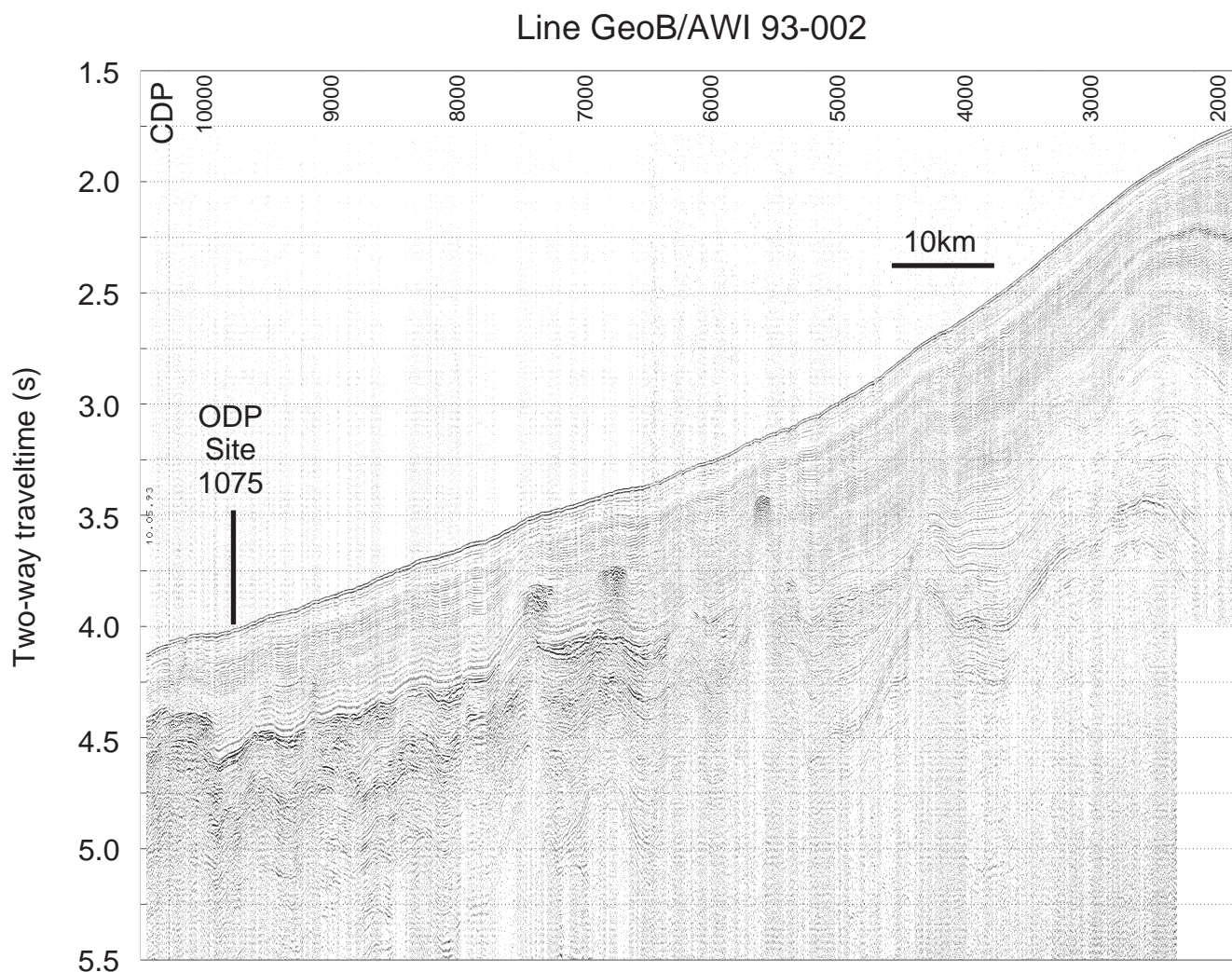
Line GeoB/AWI 93-002

Figure 6. Seismic Line GeoB/AWI 93-002 with Site 1075. Vertical axis is given in two-way traveltime. Common depth point (CDP) interval is 12.5 m for a shotpoint spacing of 25 m. Seismic data is twelvefold stacked and not migrated. Site 1075 is located at CDP 9750.

der Gaast and Jansen (1984) found that in the Congo Basin area, the peak height of smectite covaries with its crystallinity. High and low values correspond to higher and lower crystallinities, respectively. They inferred that the main source of variations in clay mineral associations is the varying contribution of poorly crystallized smectites. Consequently, low measured smectite values may represent a large contribution of this mineral to the mineral association.

In the upper 100 m of Hole 1075A, most kaolinite peaks coincide with low smectite counts, suggesting little dilution by low-crystallinity smectite and large contributions of kaolinite. There is one clear exception: at 119 m, high kaolinite intensity coincides with a high smectite intensity. Most kaolinite low counts correspond to relatively well-crystallized smectite. The relative contributions of poorly crystallized smectite (Sm) and kaolinite (K) can be expressed by their K/(K+Sm) ratio. Kaolinite is a known product of chemical weathering of igneous rocks in the tropical rain forest (Singer, 1984). High ratios, except the one at 119 m, may suggest humid periods in the Congo drainage area. Lower ratios between 30 and 130 m represent more arid periods (Fig. 15).

Spectrophotometry

Visible light reflectance was measured every 2 cm for Hole 1075A and in the upper 12 cores from Hole 1075B. The lower sec-

tions of Holes 1075B and 1075C were measured at 4-cm intervals. This decreased resolution was matched to the stratigraphic resolution used for the MST data. The variations in total visible light reflectance levels are low (20%–50%) and differ slightly among the three holes. The red/blue ratio displays a pronounced periodicity in all three holes (Fig. 16). Preliminary biostratigraphic analysis suggests that this periodicity corresponds to the 23-k.y. precession cycle (see "Biostratigraphy and Sedimentation Rates" section, this chapter). Variations in the ratio of the red-to-blue wavelengths are weakly correlated with the concentration of organic carbon but show no covariation with concentrations of $CaCO_3$ or total sulfur (Fig. 17). The ratio between the red (650 nm) and blue (450 nm) end-member reflectance levels at this site may be attributed to the presence of iron sulfides (e.g., pyrite) in the sediment. High abundances of pyrite in clays tend to decrease the reflectance of sediment at 650 nm and would lower the red/blue ratios (Mix et al., 1992). By contrast, a greater amount of diatoms would enhance the reflectance at 650 nm and would thus lead to higher red/blue ratios.

BIOSTRATIGRAPHY AND SEDIMENTATION RATES

A relatively continuous section spanning the Pleistocene and penetrating into the upper Pliocene was recovered from Site 1075. Core-

Line GeoB/AWI 93-002

Figure 7. Seismic section of Line GeoB/AWI 93-002 at Site 1075. Vertical axis is given in two-way traveltime. CDP interval is 12.5 m for a shotpoint spacing of 25 m. Site 1075 is located at CDP 9750. The box indicates the approximate penetration of the borehole of 200 m.

catcher samples were examined for all microfossil groups, and additional smear slides from within the cores were examined for calcareous nannofossils and diatoms. Biostratigraphic analysis focused on Hole 1075A, although samples from Holes 1075B and 1075C were used to supplement interpretations for Hole 1075A.

Calcareous microfossil floras and faunas are poorly preserved in much of the section, particularly in the lower portion. Siliceous microfossils show good preservation at Site 1075 and are abundant throughout Hole 1075A. Diatoms are represented by marine and freshwater taxa. Fluctuations in freshwater diatom and phytolith assemblages reflect changes in the continental supply. Pyrite is common throughout the core in the form of pyritized borrows and pyrite grains in foraminifers and diatoms, and this affects the stratigraphic resolution. Thus, both datums and environmental interpretations of the calcareous microfossil groups should be used with caution. Nevertheless, we were able to develop an integrated, high-resolution biostratigraphy for the site that is in agreement with paleomagnetic interpretations (Fig. 18). No apparent reworking has been identified.

Calcareous Nannofossils

Because of the low overall abundance and generally poor preservation of the nannofossil assemblages contained within the bottom part of Hole 1075A, additional core-catcher samples from Holes 1075B and 1075C were studied in an attempt to provide stratigraphic information for the base of Site 1075.

Nannofossil assemblages generally show low diversity and are mostly poorly preserved and sparse, especially toward the lower part of the section. Most of the samples investigated from Core 175-1075A-15H through 22H (bottom of Hole 1075A) are barren, which affects the estimates of the mean depth of the datums within Hole 1075A (Table 2). The range over which the datums could exist varies from ~3 m at the Zone NN21a/NN20 boundary to 20 m for the last occurrence (LO) of *Helicosphaera sellii.*

Within the resolution of the datums, the nannofossil biostratigraphy suggests that drilling at Site 1075 recovered a continuous stratigraphic record from the upper part of the upper Pliocene to the Holocene (Zone NN18/NN19 boundary to upper Zone NN21b). The oldest recognized datums were identified at Hole 1075B (LO of *Calcidiscus macintyrei*) and Hole 1075C (LO of *Discoaster brouweri,* zonal marker for the Zone NN18/NN19 boundary).

Zone NN21b

The acme interval of *Emiliania huxleyi* defines the top 90 k.y. of the Pleistocene and Holocene periods. Nannofossil assemblages from Cores 175-1075A-1H and 2H are dominated by this species.

Figure 8. Close-up of Line GeoB/AWI 93-002 near Site 1075. Amplitudes are grayscaled. For comparison, wet bulk density data from index properties measurements are shown, and main reflectors are correlated with local extremes in the density log. For depth determination, a sound velocity (V_p) of 1500 m/s was used.
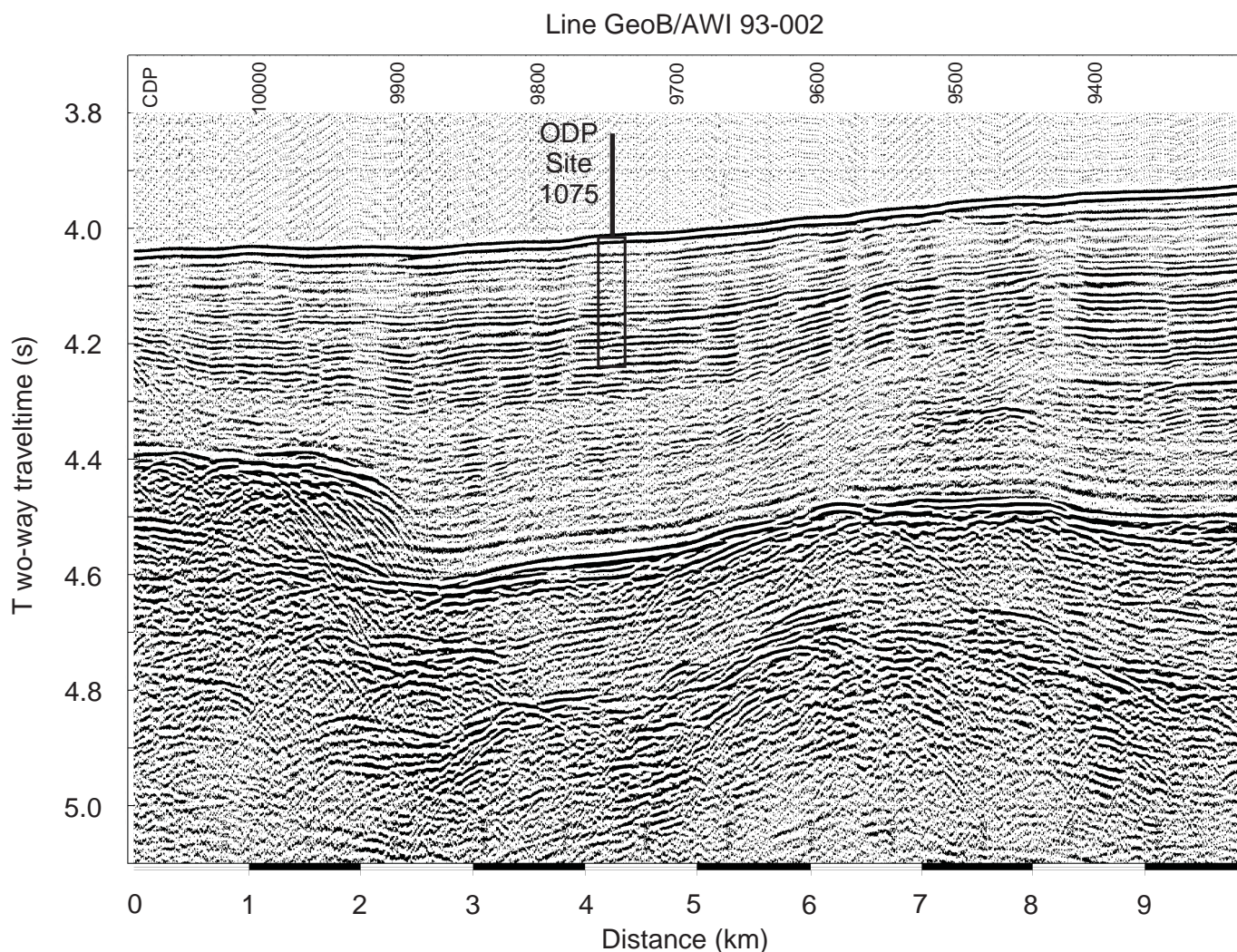
Line GeoB/AWI 93-001

Figure 9. Seismic section of Line GeoB/AWI 93-001 at Site 1076. Vertical axis is given in two-way traveltime. CDP interval is 12.5 m for a shotpoint spacing of 25 m. Site 1076 is located at CDP 22,990. The box indicates the approximate penetration of the borehole of 200 m.

Zone NN21a

The lower boundary of this zone is defined as the first occurrence (FO) of *E. huxleyi*. This event is difficult to recognize with light microscopy, particularly in poorly preserved assemblages. Since the LO of the *Gephyrocapsa caribbeanica* acme is synchronous with the *E. huxleyi* datum, the LO of *G. caribbeanica* was used instead to locate the Zone NN21a/NN20 boundary at 41.3 mbsf (Sample 175-1075A-5H-CC to Sample 6H-3, 1 cm). Nannofossil assemblages representative of this zone are characterized by the overall dominance of small *Gephyrocapsa* spp. (*G. aperta* acme Zone; Weaver, 1993).

Zone NN20

The LO of *Pseudoemiliania lacunosa,* the lower boundary marker for this zone, was identified within Core 175-1075A-7H at a mean depth of 55.6 mbsf. *G. caribbeanica* is the dominant calcareous nannofossil species within Zone NN20, but this acme interval also extends to the top of Zone NN19. The Zone NN20/NN19 boundary and its associated datum event occur within isotope Stage 12, as shown by Thierstein et al. (1977).

Zone NN19 and NN19/NN18 Boundary

This zone spans the upper part of the upper Pliocene and the lower and middle Pleistocene sequences. Site 1075 did penetrate the Zone NN19/NN18 boundary. The LO of *Discoaster brouweri,* the bound-

ary marker for this event, was identified at the base of Hole 1075C (Sample 175-1075C-22H-CC). Poorly preserved (and sometimes barren) assemblages made it impossible to recognize this datum event at Holes 1075A and 1075B. The short age range of *Reticulofenestra asanoi* was used to further constrain the stratigraphy of Zone NN19 and to compare the nannofossil chronology to the paleomagnetic time frame (see Fig. 18 and the "Paleomagnetism" section, this chapter). The top and bottom boundaries of the Small *Gephyrocapsa* acme Zone (Gartner, 1977) could not be identified, probably because of the generally poor preservation of the nannofossil assemblages within the bottom cores at Site 1075. The LO of *Helicosphaera sellii* was found at Holes 1075A and 1075B at mean depths of 142.1 and 138.7 mbsf, respectively. The presence of *C. macintyrei* in Sample 175-1075B-18H-CC provides an additional datum (1.67 Ma) for the lower part of Site 1075.

Planktonic Foraminifers

The planktonic foraminifers have limited biostratigraphic utility in the Pleistocene. The only datum for the Pleistocene, the LO of *Globorotalia tosaensis,* occurs above the Matuyama/Brunhes boundary at 0.65 Ma (Berggren et al., 1995). One specimen of *G. tosaensis* was identified at Hole 175-1075A (5H-CC), although the depth of this datum is not in agreement with the detailed age model developed using calcareous nannofossil datums (Fig. 18). The species was not found in the overlying or underlying core-catcher samples. The specimen in question may be reworked. In any case, high abundances of
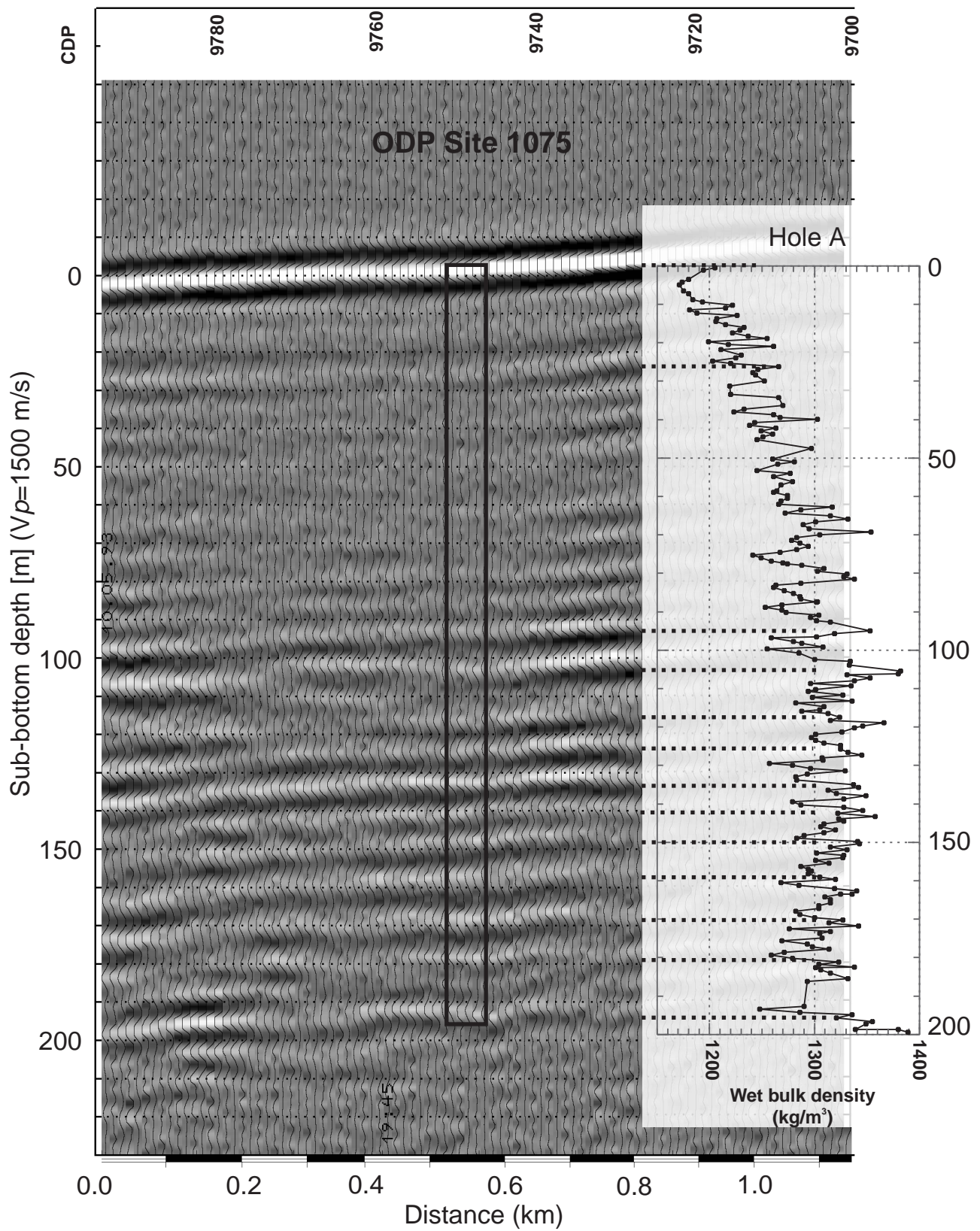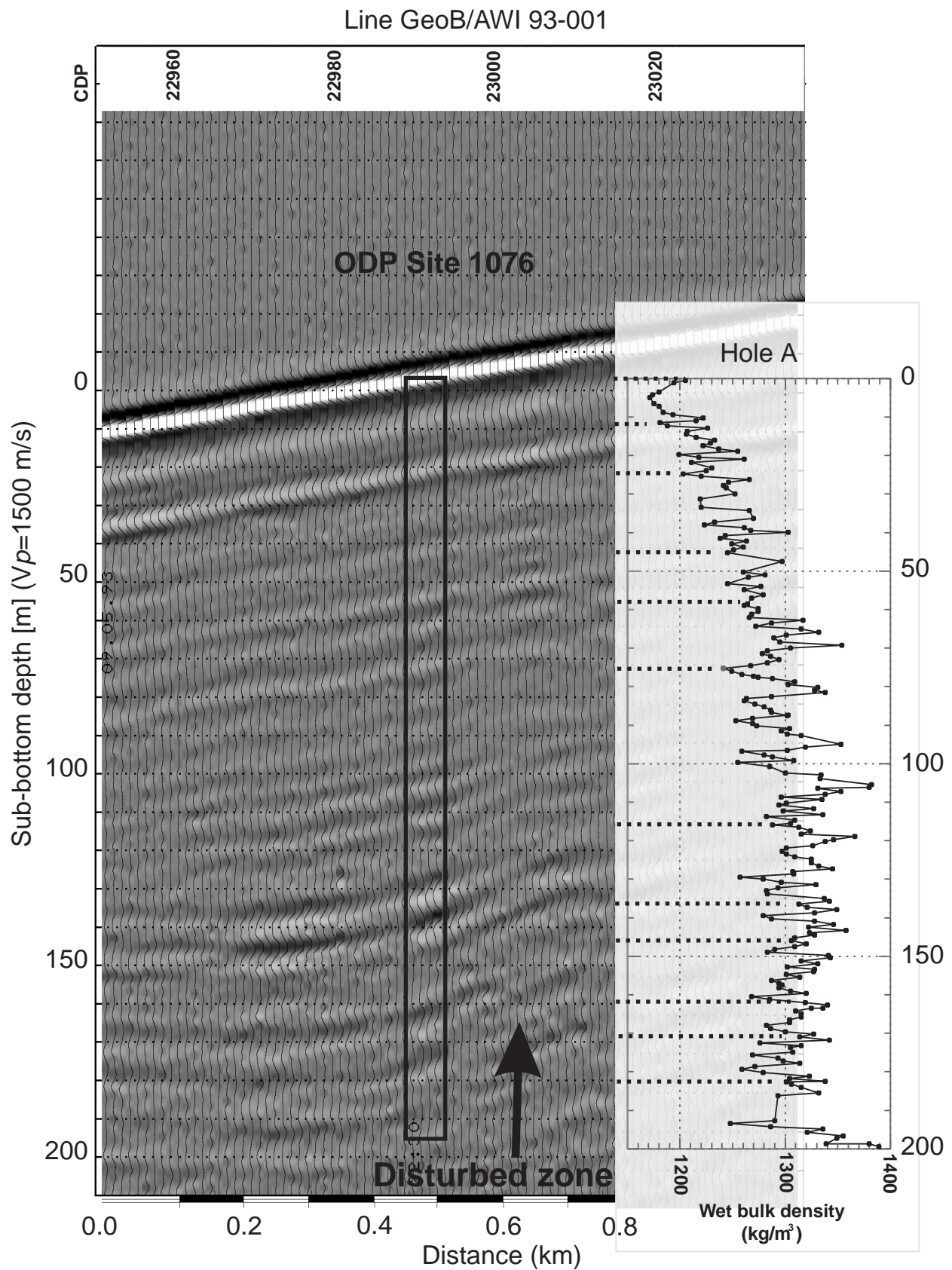
Figure 10. Close-up of Line GeoB/AWI 93-001 near Site 1076. Amplitudes are grayscaled. For comparison, wet bulk density data from index properties measurements are shown, and main reflectors are correlated with local extremes in the density log. For depth determination, a sound velocity (V_p) of 1500 m/s was used.
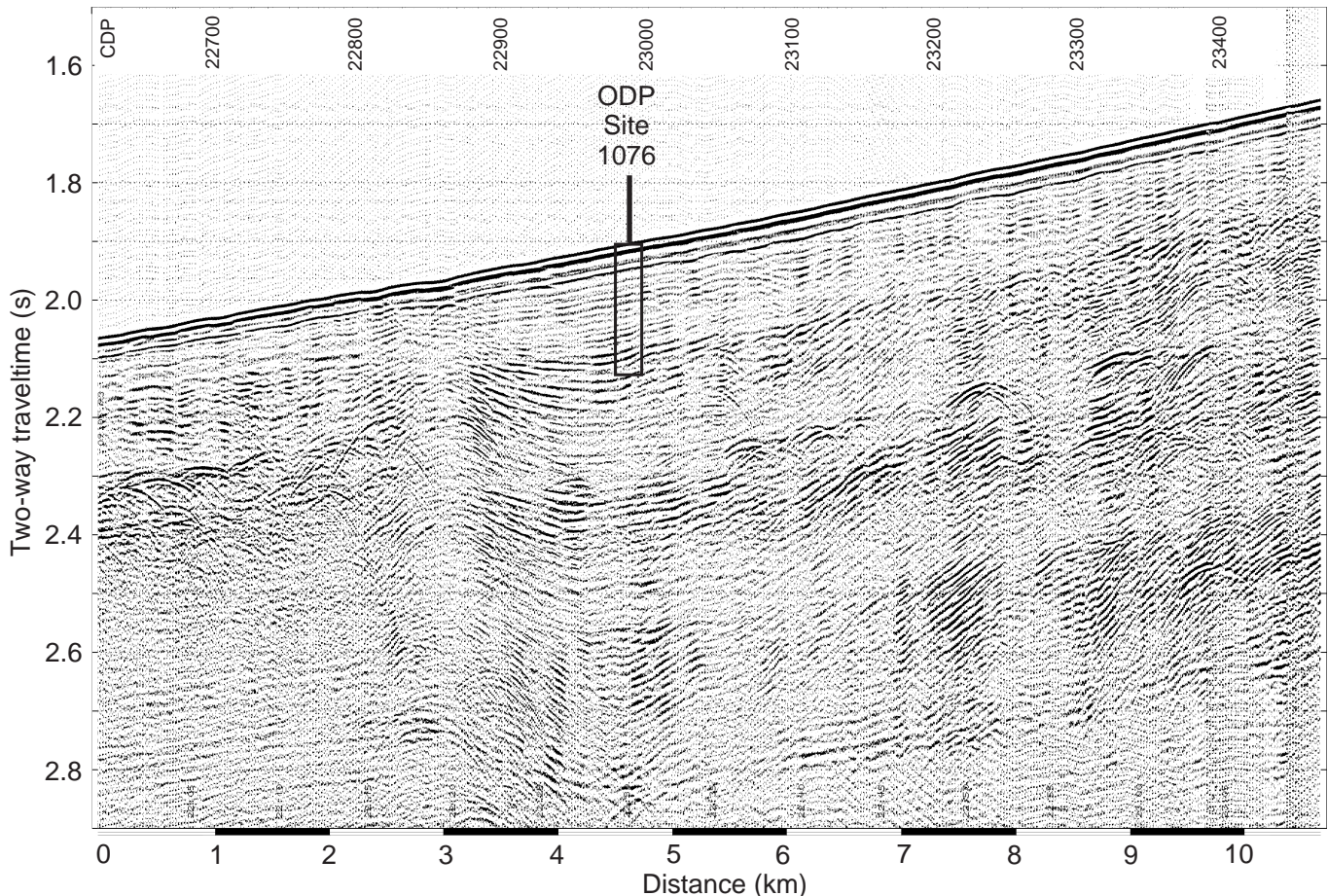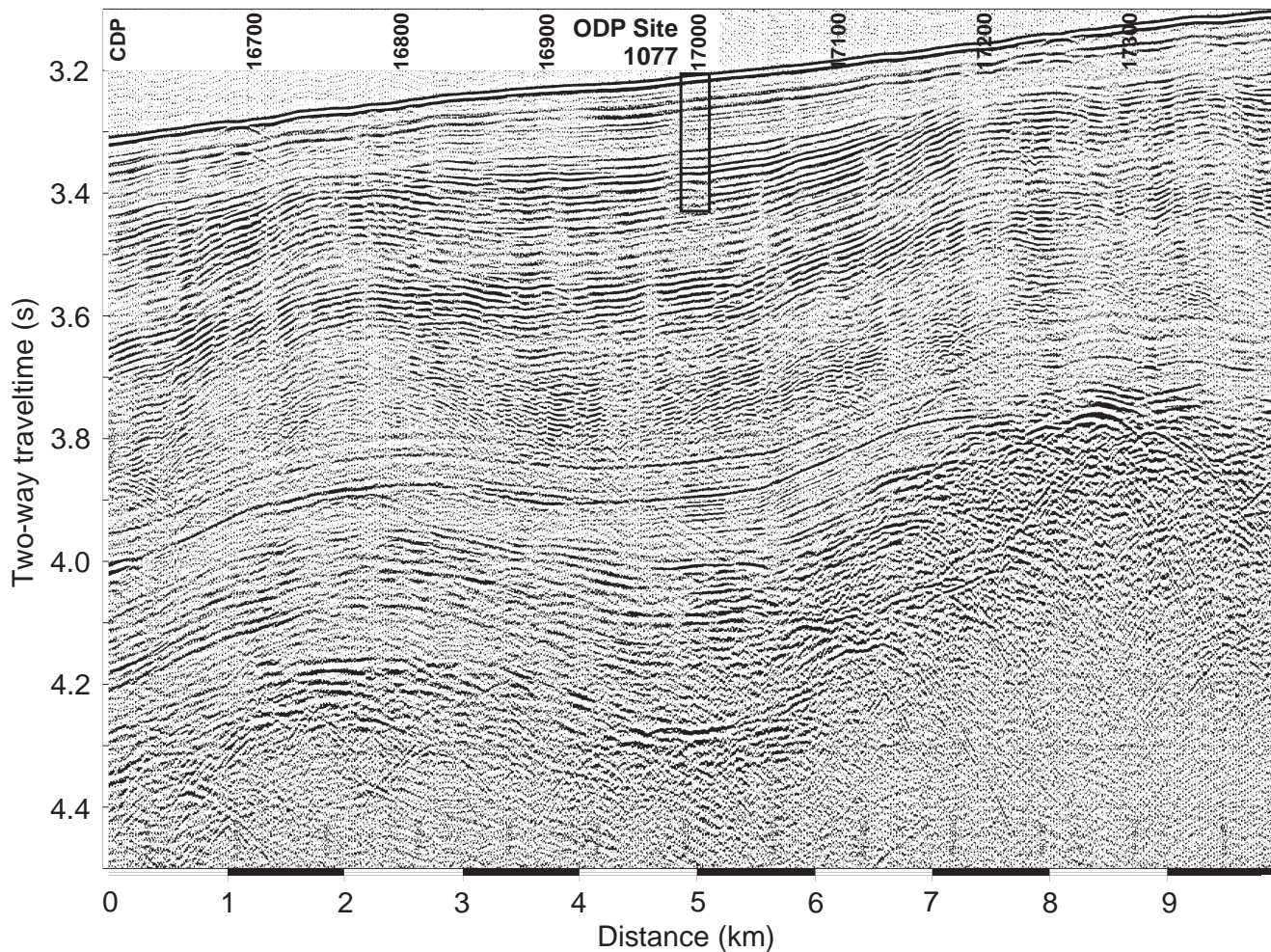
Line GeoB/AWI 93-001

Figure 11. Seismic section of Line GeoB/AWI 93-001 at Site 1077. Vertical axis is given in two-way traveltime. CDP interval is 12.5 m for a shotpoint spacing of 25 m. Site 1077 is located at CDP 17,000. The box indicates the approximate penetration of the borehole of 200 m.

G. tosaensis are not anticipated at Site 1075 because the species is ancestral to *Globorotalia truncatulinoides* (Blow, 1969), and *G. truncatulinoides* is not a significant component of the fauna in this region (Parker, 1971). Zonation schemes based on faunal changes within the Pleistocene (e.g., changes in the presence/absence of *Globorotalia menardii* and the coiling direction of *G. truncatulinoides*) are not readily applicable at Site 1075 because of dissolution. Dissolution is selective, which makes it difficult to identify faunal changes caused by hydrographic changes (Berger, 1970). Samples from 175-1075A-17H-CC through 22H-CC are barren of planktonic foraminifers, and Samples 175-1075A-11H-CC, 14H-CC, and 15H-CC show low abundances.

The uppermost core-catcher (175-1075A-1H-CC) assemblage is dominated in the coarse fraction (>250 μm) by *Globigerinoides ruber* (pink and white), *Orbulina universa,* and *Globigerina bulloides.* Other common species include *Neogloboquadrina pachyderma* (dextral), *Hastigerina siphonifera, Globorotalia crassaformis,* and the *Globigerinoides immaturus–G. sacculifer–G. quadrilobatus* series. *Globorotalia tumida, Globorotalia scitula, G. truncatulinoides, Pulleniatina obliquiloculata,* and *Globigerinita glutinata* are present but not common. This faunal distribution may be related to the presence of two water masses in the study area: the Equatorial Atlantic Undercurrent (EUC), which flows south at depth, and the overlying Angola Current. *G. ruber* and *G. crassaformis* are common components of the EUC fauna, and *G. crassaformis* is also characteristic of deeper water (Bé and Tolderlund, 1971). The high relative abundances of *G. bulloides* presumably are related to the enhanced primary productivity induced by inputs from the Congo River and seasonal coastal upwelling.

There is a downcore shift in the assemblage toward dominance of more temperate species (e.g., *N. pachyderma* and *G. inflata*), particularly in Samples 175-1075A-5H-CC and deeper. This may reflect climatic influences associated with glaciation (e.g., the northward migration of cooler surface waters of the Benguela Current). For example, there is a change to a more temperate fauna in Sample 175-1075A-2H-CC, which is, in turn, underlain by a fauna in Sample 175-1075A-3H-CC that is similar to the uppermost assemblage (Sample 175-1075A-1H-CC). Alternatively, the faunal shift may be a function of the greater resistance of these species to dissolution rather than to a hydrographic change. For example, Sample 175-1075A-14H-CC is poorly preserved and dominated by species that are very resistant to dissolution: *G. crassaformis* and *N. pachyderma* (dextral). Table 3 lists the dominant species for Site 1075 according to decreasing susceptibility to dissolution. The codominance of dissolution-resistant
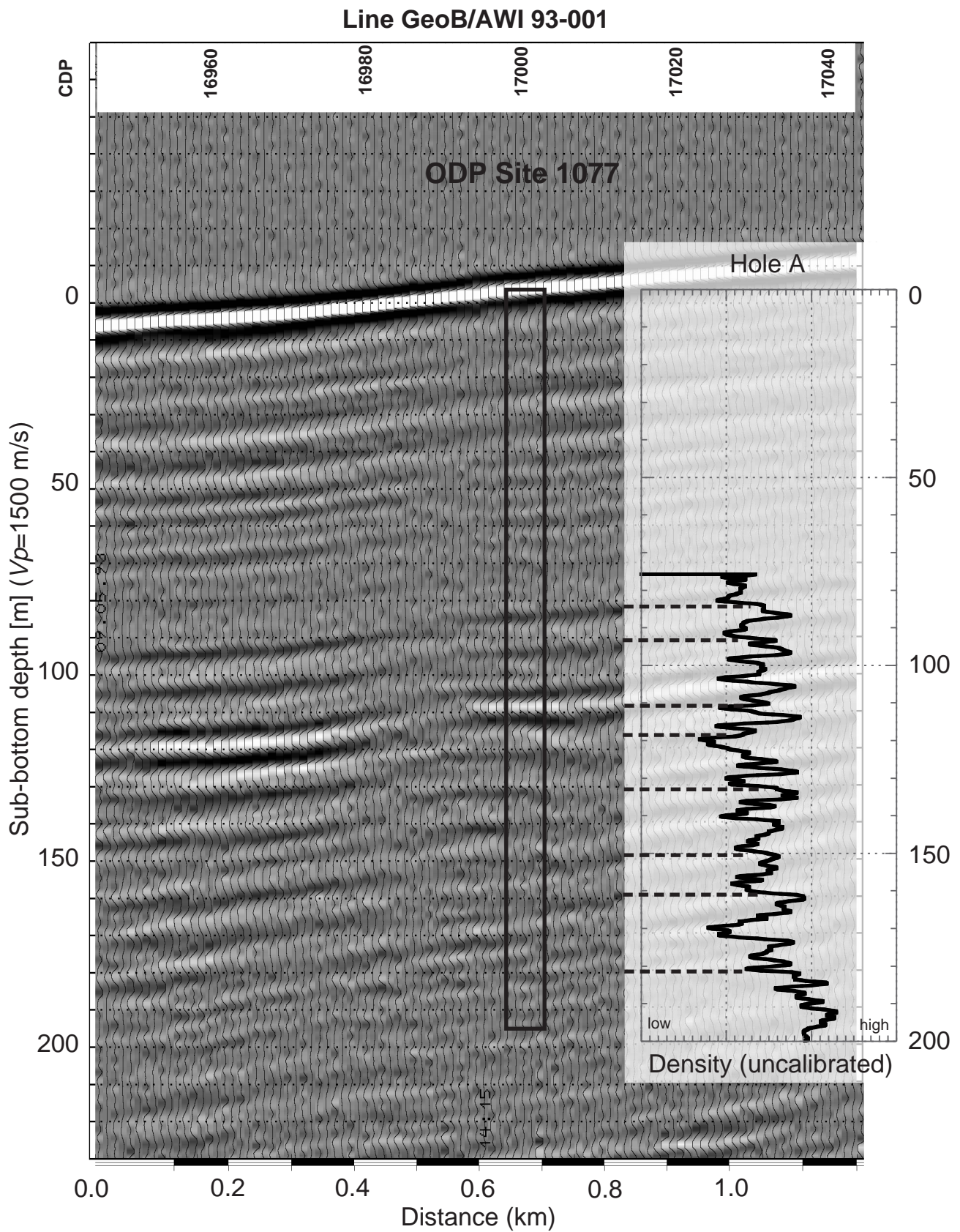
Figure 12. Close-up of Line GeoB/AWI 93-001 near Site 1077. Amplitudes are grayscaled. For comparison, the resistivity data from downhole logging are shown, which are inversely proportional to density. Main reflectors are correlated with local extremes in the density log. For depth determination, a sound velocity (V_p) of 1500 m/s was used.
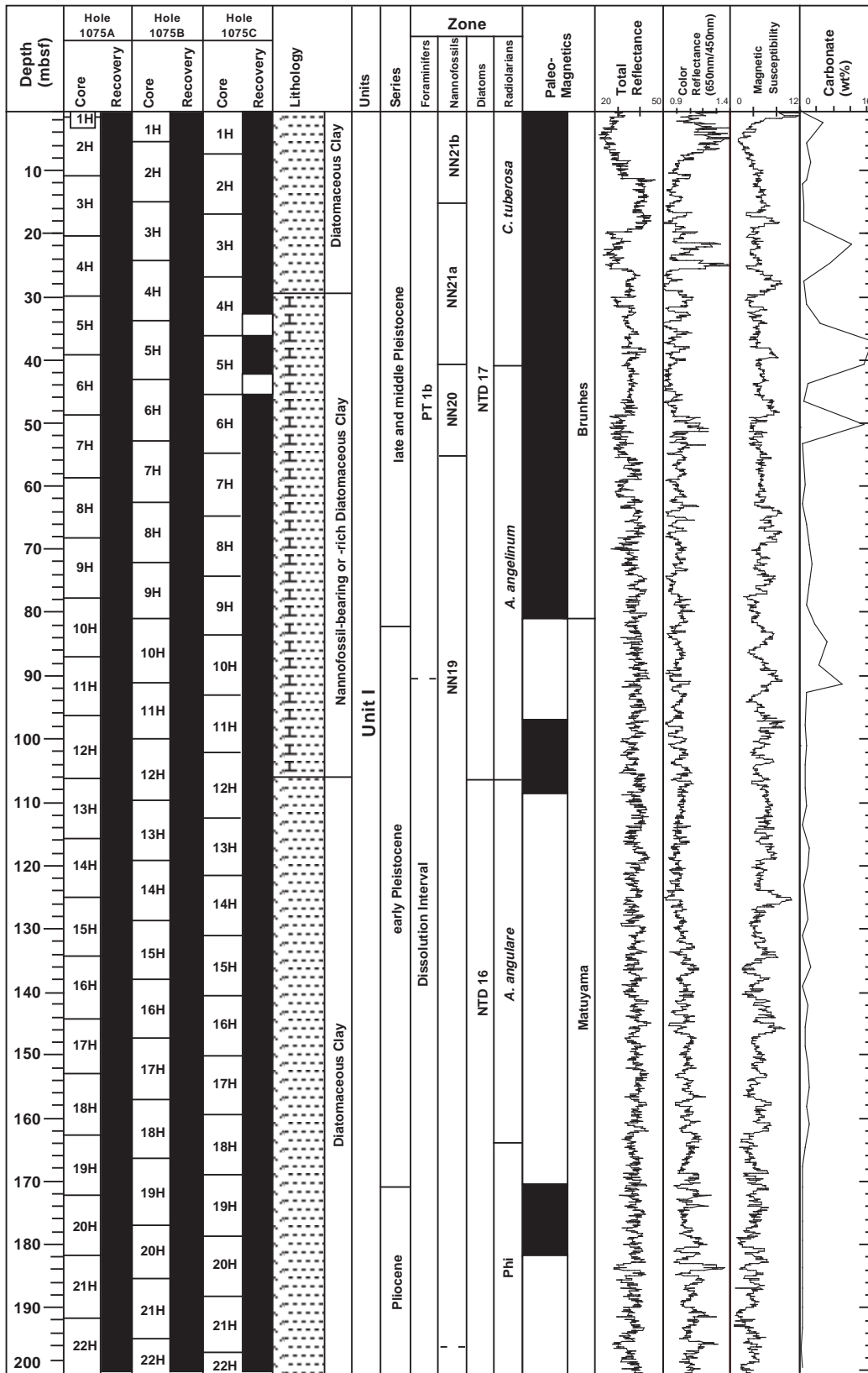
Figure 13. Composite stratigraphic section for Site 1075 showing core recovery in all holes, a simplified summary of lithology, age, calcium carbonate content, total reflectance, color reflectance (650 nm/450 nm), and magnetic susceptibility.
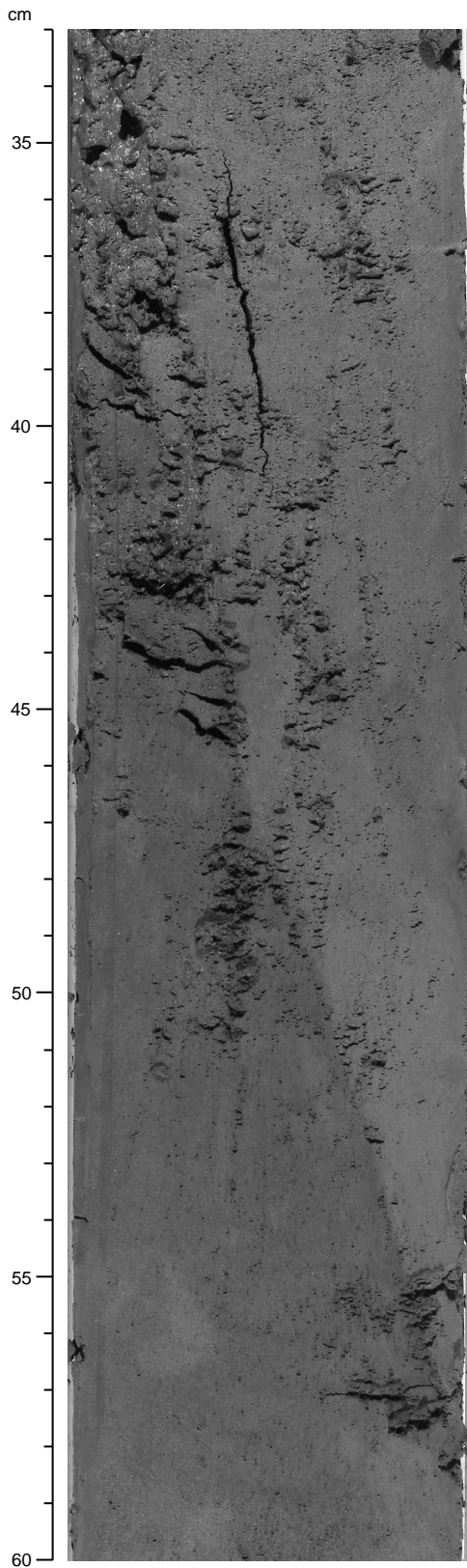
Figure 14. Sharp contact in Section 175-1075C-5H-3 marking the transition from olive-gray diatomaceous clay to very dark gray nannofossil-bearing diatomaceous clay.
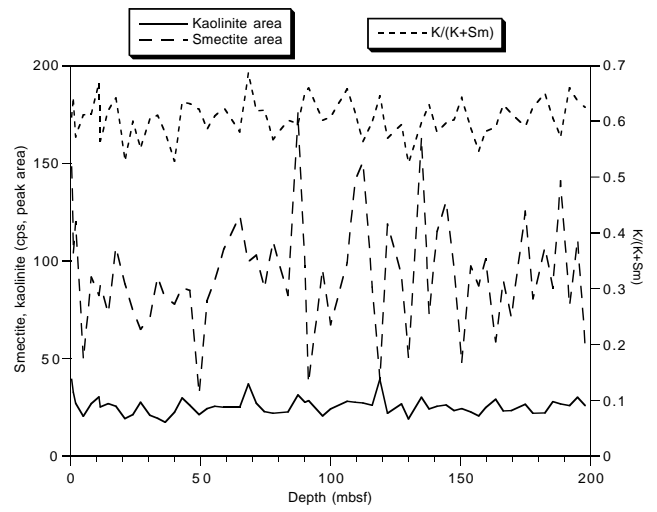
Figure 15. Stratigraphic variation in the ratio of smectite (Sm) to kaolinite (K), expressed as K/(Sm+K). Cps = counts per second.
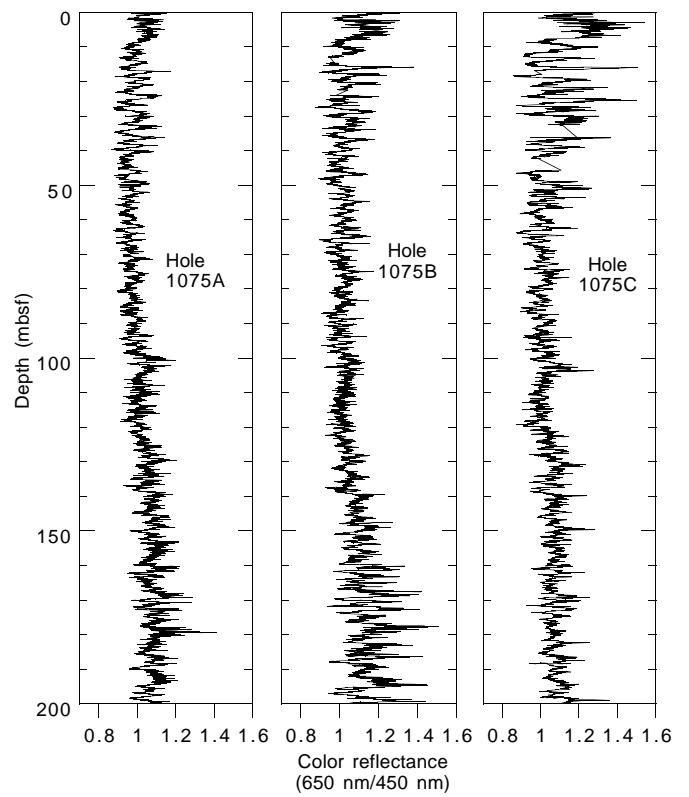
Figure 16. Stratigraphic variation in the ratio of the red (650 nm) to blue (450 nm) wavelength end-member at Holes 1075A, 1075B, and 1075C, displaying a pronounced periodicity possibly corresponding to the 23-k.y. precession cycle.

species, such as *N. pachyderma,* and dissolution susceptible species, such as *G. ruber,* indicates that the faunal response to the multiple factors controlling distribution (e.g., glacially induced changes in riverine input, hydrographic variation, and resuspension and deposition of shelf sediments) results in a complex assemblage.
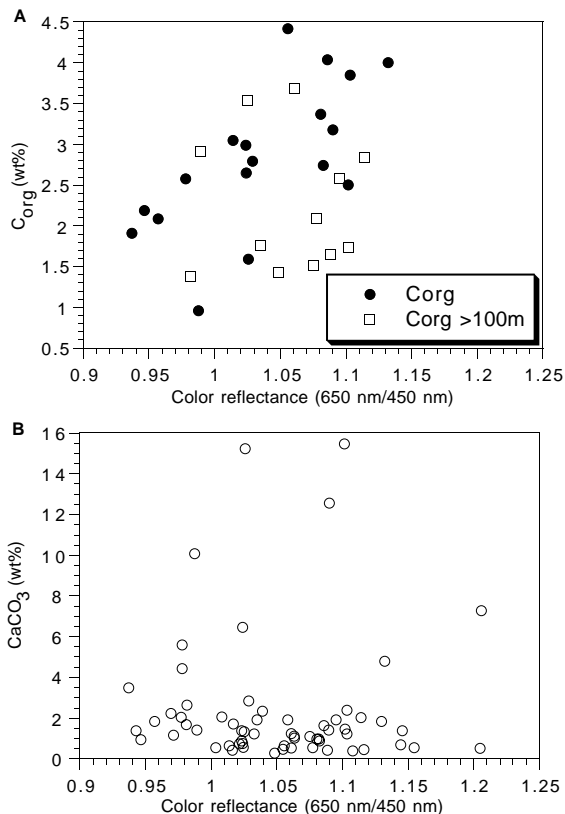
Figure 17. Relationship between the red/blue wavelength spectral ratio and the concentrations of (**A**) organic carbon and (**B**) calcium carbonate at Hole 1075A.

Benthic Foraminifers

The benthic foraminiferal fauna in the upper part of Site 1075 is characterized by low abundance and relatively low diversity. Below Sample 175-1075A-9H-CC, the benthic foraminiferal fauna is very sparse, and a marked decrease in the abundance of benthic foraminifers occurs. Below Sample 175-1075A-14H-CC, the core catchers are essentially barren, probably a result of dissolution. The preservation is good to moderate in the upper part of Site 1075 with the exception of Sample 175-1075A-4H-CC, which is essentially barren. Farther down the hole, preservation deteriorates.

The relative abundance of the benthic foraminifers found at Site 1075 is presented in Table 4. The dominant species in the uppermost two core catchers (175-1075A-1H-CC and 2H-CC) are the *Melonis barleeanum/M. pompilioides* group and *Uvigerina peregrina;* in the uppermost sample, the fragile *Chilostomella ovoidea* predominates. Farther downcore, in the interval 175-1075A-3H-CC through 9H-CC, the *Praeglobobulimina/Globobulimina* group, together with *Melonis barleeanum* and *M. pompilioides,* are the dominant species, with strong contributions from *Bulimina exilis* and various uvigerinids. Below Sample 175-1075A-10H-CC, there is a marked decrease in total abundance of benthic foraminifers, which makes comments on the assemblages unreliable. The species *Melonis barleeanum* is not present in the lower part of the hole, and *Epistominella exigua* is restricted to the lower part. The uvigerinids as well as *Melonis pompilioides* and the *Praeglobobulimina/Globobulimina* group are present throughout the hole, with the exception of those core catchers that are barren.

An important factor to consider is the variation in susceptibility to dissolution of different benthic foraminiferal species. The overall downcore increase in dissolution not only decreases the abundance but also modifies the composition of the benthic foraminiferal assemblages.

Radiolarians

Hole 1075A contains abundant, well-preserved radiolarians (Table 5). The absence of *Axoprunum angelinum* indicates that the uppermost cores (Samples 175-1075A-1H-CC through 5H-CC) are within either the Pleistocene *Collosphaera tuberosa* Zone or the
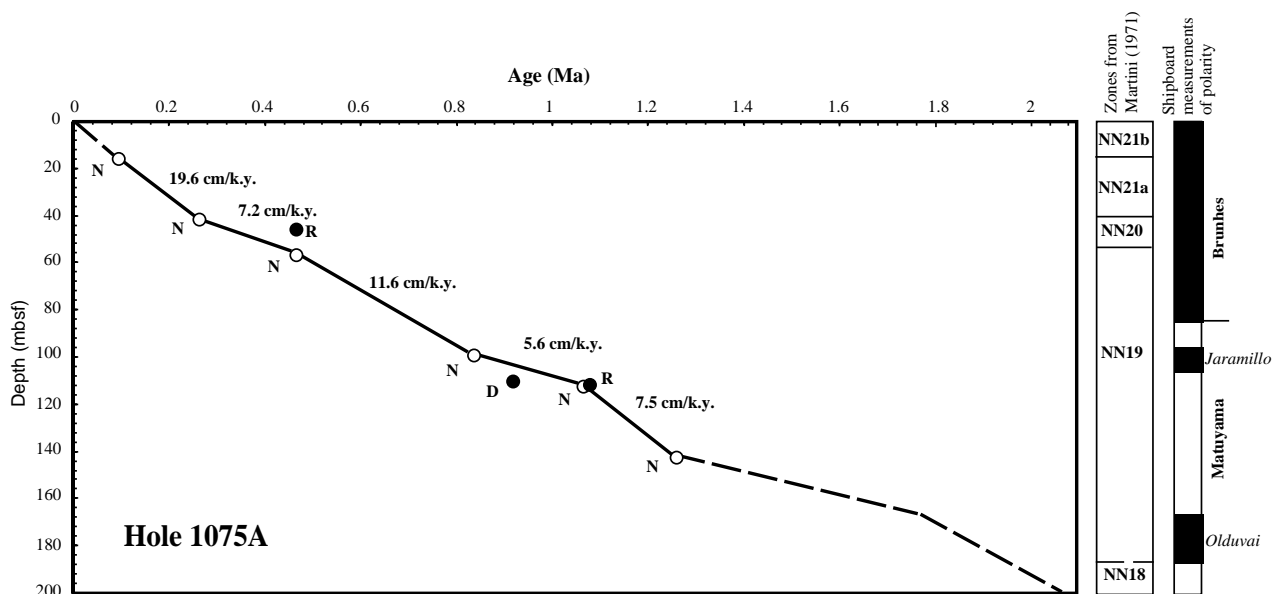
Figure 18. Age-depth plot and sedimentation rates for Hole 1075A estimated from calcareous microfossils (open circles; N = calcareous nannofossils) and siliceous microfossils (closed circles; D = diatoms and R = radiolarians).

Table 2. Microfossil datums at Holes 1075A, 1075B, and 1075C.

Fossil group	Event	Age (Ma)	Zone (base) A	Zone (base) B	Core, section, interval (cm) Top	Core, section, interval (cm) Bottom	Depth (mbsf) Top	Depth (mbsf) Bottom	Depth (mbsf) Mean
					175-1075A-	175-1075A-			
N	FO *Emiliania huxleyi* acme	0.09	NN21b		2H-CC	3H-5, 138	11.23	18.38	14.8
N	FO *Emiliania huxleyi*	0.26	NN21a	CN15	5H-CC	6H-3, 1	39.95	42.60	41.3
N	LO *Gephyrocapsa caribbeanica* acme	0.26	NN21a	CN15	5H-CC	6H-3, 1	39.95	42.60	41.3
N	LO *Pseudoemiliania lacunosa*	0.46	NN20	CN14b	7H-3, 10	7H-CC	52.13	59.05	55.6
R	LO *Axoprunum angelinum*	0.46			5H-CC	6H-CC	39.95	49.45	44.7
N	LO *Reticulofenestra asanoi*	0.83			11H-CC	12H-3, 33	97.12	99.83	98.5
D	LO *Nitzschia fossilis*	0.92			12H-CC	13H-CC	106.84	116.19	111.5
N	FO *Reticulofenestra asanoi*	1.06			12H-CC	13H-CC	106.84	116.19	111.5
R	LO *Lamprocyrtis neoheteroporos*	1.07			12H-CC	13H-CC	106.84	116.19	111.5
N	LO *Helicosphaera sellii*	1.25			15H-6, 40	17H-6, 130	131.38	152.80	142.1
					175-1075B-	175-1075B-			
N	LO *Helicosphaera sellii*	1.25			14H-CC	16H-CC	129.07	148.35	138.7
N	LO *Calcidiscus macintyrei*	1.67			17H-CC	18H-CC	157.72	167.54	162.6
					175-1075C-	175-1075C-			
N	LO *Discoaster brouweri*	1.95	NN19	CN13a	Not sampled	22H-CC	No data	208.09	<208.1

Notes: Fossil group: N = calcareous nannofossils; D = diatoms; and R = radiolarians. FO = first occurrence and LO = last occurrence. Zonal codes refer to the standard zonations of (A) Martini (1971) and (B) Okada and Bukry (1980).

Table 3. The dominant and abundant planktonic foraminiferal species at Hole 1075A.

Core, section, interval	Dissolution intervals	*Globigerinoides ruber* (pink)	*Globigerinoides ruber*	*Orbulina universa*	*Globigerinoides trilobus*	*Globigerina bulloides*	*Globorotalia inflata*	*Neogloboquadrina dutertrei*	*Neogloboquadrina pachyderma* (dextral)	*Globorotalia crassaformis*
175-1075A-										
1H-CC		A	A	A		A				
2H-CC		A		A		D		A		A
3H-CC		A	A	A	A					
4H-CC	DISS									
5H-CC				A	A			A		
6H-CC		A		D			A			
7H-CC			A					D		
8H-CC				A		A		D		
9H-CC				D		A	A	A		
10H-CC			A		A			A		
11H-CC	DISS									
12H-CC			A	A	A	A		A		
13H-CC			D				A	A	A	
14H-CC								A	D	
15H-CC	DISS									
16H-CC			A				A	D		

Notes: The species are arranged by decreasing susceptibility to dissolution, from left to right, according to the Berger (1970) scale. Note the downcore change to more dissolution resistant species such as *G. crassaformis* and *N. pachyderma*. Core-catcher samples from Cores 175-1075A-16H through 22H are essentially barren of planktonic foraminifers. A = abundant (10%–30%); D = dominant (>30%); and DISS = barren or very few specimens (dissolution interval).

Pleistocene to Holocene *Buccinosphaera invaginata* Zone of Moore (1995). A finer zonal resolution could not be obtained because of the absence of *B. invaginata*.

Although the diagnostic species *Anthocyrtidium angulare* is absent from the core, Samples 175-1075A-6H-CC through 12H-CC are approximately assigned to the Pleistocene *A. angelinum* Zone or the *Amphirhopalum ypsilon* Zone of Moore (1995) based on the presence of *A. angelinum* and the absence of *Lamprocyrtis neoheteroporos.* The diagnostic species *C. tuberosa* used to recognize the *A. angelinum* and *A. ypsilon* Zones are absent. The LO of *L. neoheteroporos*

is found in Sample 175-1075A-13H-CC, indicating an age older than 1.07 Ma for Samples 13H-CC through 22H-CC.

The last consistent occurrence of *Eucyrtidium calvertense* in Sample 19H-CC is correlative to the extinction of *E. calvertense* at the base of the Olduvai magnetic polarity event in the southern high-latitude oceans (Hays, 1965; Hays and Opdyke, 1967). This indicates that regardless of the absence of the diagnostic species *Pteropcanium prismatium,* Samples 13H-CC through 18H-CC are approximately assigned to the *A. angulare* Zone of Moore (1995) and that the lowermost cores (Samples 19H-CC through 22H-CC) belong to the Pliocene Phi Zone of Hays (1965). The presence of *Cycladophora davisiana* throughout the core indicates an age of <2.71 Ma for the lowermost cores.

The rare sporadic occurrences following the last consistent occurrence of *E. calvertense* may not be evidence of reworking. Instead, this species may have a longer range in this region, similar to its sporadic occurrence through the Pleistocene in the North Pacific (Kling, 1973).

A preliminary examination of core-catcher samples indicates the presence of faunal fluctuations. The ratio of upwelling index species to circum-tropical warm-water index species shows significant variation from sample to sample.

The upwelling index consists of five species: *Acrosphaera murrayana, Cycladophora davisiana, Botryostrobus auritus/australis, Lamprocyrtis neoheteroporos,* and *L. nigriniae.* This upwelling index has been established in the Peru margin upwelling region and the Oman margin upwelling region (Nigrini, 1991). The species *Didymocyrtis tetrathalamus, Dictyocoryne* spp., *Euchitonia* spp., *Octopyle stenozona, Tetrapyle octacantha,* and *Acanthodesmia viniculata* (= *Giraffospyris angulata*) have been selected as species representing the warm-water index. All of these species, except for *Euchitonia* spp., are species with well-known ecologies (Lombari and Boden, 1985). The ratio of the upwelling species to warm-water species was estimated by counting 100 specimens of the index species in core-catcher samples. Figure 19 shows the variations in relative abundances of the upwelling index species at Hole 1075A. The relative abundance of upwelling species ranges from 3% (Samples 175-1075A-3H-CC and 10H-CC) to 64% (Sample 2H-CC). This suggests that the strength of upwelling in the water column above Hole 1075A has changed significantly throughout the Pleistocene.

Diatoms

Diatoms were the dominant microfossil group at Hole 1075A. Species counts and identification were carried out on smear slides. In

Table 4. Relative abundance of benthic foraminiferal species and overall abundance of benthic foraminifers at Hole 1075A.

Core, section, interval	Depth (mbsf)	Abundance	Bolivina seminuda	Bulimina aculeata	Bulimina exilis	Bulimina truncana	Cassidulina minuta	Cassidulina laevigata	Chilostomella oolina	Chilostomella ovoidea	Cibicidoides wuellerstorfi	Eggerella bradyi	Epistominella exigua	Fissurina spp.	Globocassidulina subglobosa	Gyroidinoides soldani	Hoeglundina elegans	Melonis barleeanum	Melonis pompilioides	Nonionella turgida	Oolina spp.	Oridorsalis umbonatus	Praeglobo-/Globobulimina group	Pullenia bulloides	Pullenia subcarinata	Pyrgo spp.	Quadromorphina allomorphoides	Quinqueloculina spp.	Robertinoides bradyi	Sigmoilinopsis schlumbergeri	Sphaeroidina bulloides	Stilostomella spp.	Triloculina trigonula	Uvigerina auberiana	Uvigerina hispidocostata	Uvigerina peregrina	Unidentified	Number of specimens counted
175-1075A-																																						
1H-CC	1.47	F		+				7	5	15			4	4	4		+	26					+	2	+	4	1		+	+	+			1		17	5	167
2H-CC	11.23	F	16			1	2	6			2	+	+	1	1			2	17					5	3	4	3		+	+	+			3	5	14	11	140
3H-CC	20.91	F	2				1	2	2		4	+		1				15	7	+			40	3	1	1			+				3	+	+	4	14	163
4H-CC	30.29	T																P					P											P				3
5H-CC	39.95	F		3	1	+		+	2	+	11			3		2	2	6	23	1		4	19	3	1	+			+							4	10	159
6H-CC	49.45	C	1		3		2	+	2		3			2				21	10		+	4	1	22	1	2	7	+					+	5	1	3	12	278
7H-CC	59.05	C			18			2		2	+			1		+	+	6	30				5	12	2		+							5		6	9	296
8H-CC	68.74	F	8		4		+	10		+	2			2				10	10				3	18	2	+	3	2				+			8	2	3	9	115
9H-CC	78.27	C			+		+	+	+		4			2				19	26			+	2	18	2	+	2				+			15	5		3	329
10H-CC	87.84	R						2	6		4		19		2				10			2	4	15	2	4	4					8		2	4	6	8	52
11H-CC	97.12	R											6						52			2		4								2	2	15	10		8	52
12H-CC	106.84	T													P																P							3
13H-CC	116.19	F		+									+	4	2				60			2	+	10	2	+						2		3	4	+	8	136
14H-CC	125.69	R		6							15			6	4				4			2	6	7	4	2	2					11		15	9	6	4	54
15H-CC	135.21	T									P								P																			3
16H-CC	154.20	T											P						P				P	P													P	27
17H-CC	154.20	T											P						P				P									P		P		P		10
18H-CC	163.68	B																																				0
19H-CC	173.17	B																																				0
20H-CC	183.16	T												P					P				P									P		P		P		7
21H-CC	192.12	B																																				0
22H-CC	201.59	T							P																													0

Notes: The relative abundance of benthic foraminiferal species is given as a percentage, where + = <1% and P = present (the relative abundance was not calculated because of small sample size). Absolute abundance (per ~20 cm³ of sediment) of benthic foraminifers is given as A = abundant (>500 specimens); C = common (250–500 specimens); F = few (100–249 specimens); R = rare (50–99 specimens); T = trace (1–49 specimens); and B = barren (no specimens).

Table 5. Stratigraphic distribution of radiolarians at Hole 1075A.

Age	Zone	Core, section, interval (cm)	Depth (mbsf)	Abundance	Preservation	Acanthodesmia viniculata	Cycladophora cornutoides	Cycladophora davisiana	Didymocyrtis tetrathalamus tetrathalamus	Eucyrtidium anomalum	Lamprocyclas hannai	Lamprocyrtis nigriniae	Phormostichoartus corbula	Pterocanium praetextum eucolpum	Pterocanium trilobum	Spongaster tetras tetras	Theocorythium trachelium trachelium	Eucyrtidium calvertense	Lamprocyrtis neoheteroporos	Amphirhopalum ypsilon	Pterocanium praetextum praetextum	Axoprunum angelinum	Lithopera (Lithopera) bacca	Lamprocyrtis heteroporos
		175-1075A-																						
Pleistocene	*B. invaginata–C. tuberosa*	1H-CC, 49-52	1.47	A	G	P	P	P	P	P	P	P	P	P	P	P	P							
Pleistocene	*B. invaginata–C. tuberosa*	2H-CC, 11-15	11.23	A	G		P	P	P	P	P	P	P	P	P				+					
Pleistocene	*B. invaginata–C. tuberosa*	3H-CC, 16-20	20.91	A	G	P	P	+	P	P			P	P	P	P	P	+		P	P			
Pleistocene	*B. invaginata–C. tuberosa*	4H-CC, 19-24	30.29	A	G	P	P	P	P					P	P			P	+		P			
Pleistocene	*B. invaginata–C. tuberosa*	5H-CC, 16-21	39.95	A	G	P	P	P	P		P	P	P	P	P	P				P	P			
Pleistocene	*A. angelinum–A. ypsilon*	6H-CC, 20-25	49.45	A	G		P	P	P	P	P	P	P	P	P	P	P			P		P	P	
Pleistocene	*A. angelinum–A. ypsilon*	7H-CC, 15-19	59.05	A	G	P		P	P		P	P	P	P	P	P		+				P		
Pleistocene	*A. angelinum–A. ypsilon*	8H-CC, 22-27	68.75	A	G			P	P		P	P		P	P	P		P				P		
Pleistocene	*A. angelinum–A. ypsilon*	9H-CC, 26-31	78.27	A	G	P	P	P	P		P			P	P	P						P		
Pleistocene	*A. angelinum–A. ypsilon*	10H-CC, 26-31	87.84	A	G	P	P	P	P		P	P	P	P	P	P		+		P		P	P	
Pleistocene	*A. angelinum–A. ypsilon*	11H-CC, 34-40	97.12	A	G	P	P	P	P		P	P	P	P	P	P						P		
Pleistocene	*A. angelinum–A. ypsilon*	12H-CC, 28-33	106.84	A	G	P	P	P	P	P	P			P	P	P						P		
Pleistocene	*A. angulare*	13H-CC, 18-23	116.19	A	G		P	P	P		P			P	P	P	P					P		
Pleistocene	*A. angulare*	14H-CC, 29-34	125.69	A	G		P	P	P		P			P	P	P		+		+		P		
Pleistocene	*A. angulare*	15H-CC, 33-38	135.21	A	G	P	P	P	P	P	P				P		P	P	+	P	P	P		P
Pleistocene	*A. angulare*	16H-CC, 19-24	144.49	A	G	P	P	P	P		P		P	P	P	P		P		P	P	P		+
Pleistocene	*A. angulare*	17H-CC, 24-29	154.20	A	G	P	P	P	P				P	P	P			P		P		P		+
Pleistocene	*A. angulare*	18H-CC, 15-20	163.68	A	G	P	P	P	P				P	P	P					P		P		+
late Pliocene	Phi	19H-CC, 25-30	173.17	A	G		P	P	P		P		P	P	P			P		P		P		+
late Pliocene	Phi	20H-CC, 19-24	183.16	A	G		P	P	P		P	P	P	P	P			P		P	P	P	P	P
late Pliocene	Phi	21H-CC, 21-26	192.12	A	G		P	P	P		P		P	P	P			P		P	P	P		P
late Pliocene	Phi	22H-CC, 19-24	201.59	A	G		P	P	P	P	P		P		P			P		P	P	P		P

Notes: Abundance is indicated by A = abundant; P = present; and + = one specimen per slide. Preservation is indicated by G = good. Phi refers to the Pliocene Phi Zone of Hays (1965).
B. invaginata = Buccinosphaera invaginata; C. tuberosa = Collosphaera tuberosa; A. angelinum = Axoprunum angelinum; A. ypsilon = Amphirhopalum ypsilon; and *A. angulare = Anthocyrtidium angulare.*

addition, opaline phytoliths and silicoflagellates were also counted without distinction of species or morphotypes. Diatoms are abundant and well preserved throughout Hole 1075A, except for Sample 175-1075A-10H-CC (Table 6; Fig. 20). Examination of the core-catcher samples indicates a Pleistocene age for this hole. Samples 175-1075A-1H-CC through 12H-CC are assigned to the *Pseudoeunotia doliolus* Zone, and Samples 175-1075A-13H-CC through 21H-CC to the *Nitzschia rheinholdii* Zone. A biostratigraphic marker species is lacking from Sample 175-1075A-22H-CC. Pliocene species are not found in Hole 1075A.

The flora is dominated by upwelling-indicator species (>50% of total diatom assemblage consists of *Thalassionema nitzschioides* var. *nitzschioides* and *Chaetoceros* resting spores and setae; Table 6), ac-

companied by freshwater taxa (e.g., *Aulacoseira granulata, A. islandica,* and *Cyclotella* spp.), neritic species (e.g., *Actinoptychus senarius*), and species characteristic of oceanic conditions (e.g., *Alveus* [= *Nitzschia*] *marinus* and *Rhizosolenia robusta*). In general, indicator species characterize Hole 1075A as upwelling-dominated with variable freshwater input (Fig. 20).

The presence of freshwater diatoms at Hole 1075A is attributed to supply by the Congo River, and high abundances may be interpreted as signals for humid intervals on the African continent (e.g., Jansen et al., 1989). The contribution of the freshwater assemblage is moderately high in Samples 175-1075A-4H-CC (~5%), 10H-CC (~10%), and 15H-CC (~6%) and is high in Sample 22H-CC (~27%). Opaline phytoliths, the second continental signal, are present in low numbers in almost all core-catcher samples; highest relative abundances are seen in Sample 10H-CC.

PALEOMAGNETISM

The investigation of magnetic properties at Site 1075 included the measurement of bulk susceptibility of whole-core sections and the natural remanent magnetization (NRM) of archive-half sections. AF demagnetization at 10 mT and 20 mT was conducted for Hole 1075A and AF demagnetization at 20 mT was conducted for Holes 1075B and 1075C. The Tensor tool was used to orient Holes 1075A and 1075B, starting with Core 4H, and Hole 1075C, starting with Core 3H (Table 7). Cores 175-1075A-21H and 22H and 175-1075B-16H through 22H were not oriented because of technical problems with the Tensor tool.

Natural Remanent Magnetization and Magnetic Susceptibility

Intensity of NRM after 20-mT demagnetization from all three holes is similar in magnitude, ranging from ~10^{-5} to ~10^{-3} A/m (Fig. 21, left panel). Within the upper 40 mbsf, the intensity is on the order of 10^{-4} A/m, except for the uppermost part where intensities are an or-

Figure 19. Relative abundance of radiolarian upwelling index species to the total upwelling and radiolarian warm-water index species in core-catcher samples from Hole 1075A.

Table 6. Overall diatom abundance and relative contribution of the dominant species or assemblages at Hole 1075A.

Core, section, interval (cm)	Depth (mbsf)	Overall abundance	Overall preservation	*Thalassionema nitzschioides* (%)	*Chaetoceros* resting spores (%)	Freshwater assemblage (%)	*Aulacoseira granulata/islandica*	*Cyclotella* spp.	Phytoliths	Ratio PhFD	Silicoflagellates
175-1075A-											
1H-CC	1.47	A	G	68.7	30.1	0.7	T	R	T	4.8	R
2H-CC	11.23	A	G	44.8	49.0	2.6	R	F	T	10.0	T
3H-CC	20.91	A	M	64.6	31.0	3.4	T	F	T	3.6	T
4H-1, 70	21.20	A	M	68.3	25.4	3.2	T	C	T	3.9	T
4H-CC	30.29	A	M	50.8	42.1	5.2	T	C	T	1.0	T
5H-CC	39.95	A	M	47.4	51.1	0.5	T	T	T	43.7	T
6H-CC	49.45	A	M	74.2	24.7	0.6	T	R	T	4.5	R
7H-CC	59.05	A	M	54.9	34.8	0.2	T		T	33.3	T
8H-CC	68.74	A	M	59.9	38.0	1.0	R	T	T	16.0	T
9H-CC	78.27	A	M	56.3	41.9	0.8	T	T	T	1.5	R
10H-CC	87.84	F	P	56.5	31.5	10.3	T	T	R	50.0	T
11H-CC	97.12	C	M	61.0	36.6	1.0	T	R	T	0.8	R
12H-CC	106.84	A	M	74.9	23.6	0.5	T	T	T	28.6	F
13H-CC	116.19	A	M	73.7	24.4	0.5	T	T	T	27.3	R
14H-CC	125.69	A	M	49.4	47.8	0.8	T	T		0.0	R
15H-CC	135.21	C	M	47.6	40.4	5.6	T	R	T	3.4	T
16H-CC	154.20	A	M	53.4	31.3	1.5	T	R	T	5.9	T
17H-CC	154.20	C	M	39.3	47.2	2.6	T	T		0.0	T
18H-CC	163.68	C	P	67.6	27.8	1.3	T	T	T	9.0	T
19H-7, 80	172.80	A	M	24.8	52.1	6.5	T	T		0.0	T
20H-CC	183.16	A	M	46.8	30.2	2.1	T		T	40.0	T
21H-7, 15	191.15	C	M	15.7	52.2	2.2		T		0.0	T
22H-CC	201.59	C	M	38.1	7.4	27.3	T	C		0.0	T

Notes: Includes diatom upwelling and freshwater assemblages, opaline phytoliths, and silicoflagellates (in percentages). Abundance: A = abundant; F = few; C = common; T = trace; and R = rare. Preservation: G = good; M = moderate; and P = poor. PhFD = the ratio of opal phytoliths to freshwater diatoms, calculated as [phytoliths/(freshwater + phytoliths)] × 100 (Jansen et al., 1989).
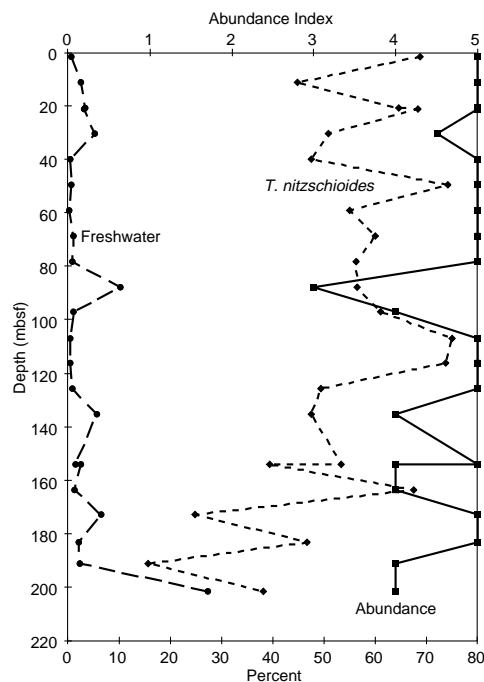

Figure 20. Diatom abundance (z-axis) and percent *T. nitzschioides* and freshwater diatoms (x-axis) at Hole 1075A. Abundance index: 5 = abundant, 4 = common, 3 = few, 2 = rare, 1 = trace, 0 = barren. *T. nitzschioides* is an upwelling indicator in the Congo Fan area.

Table 7. Tensor tool–orientation data for cores from Holes 1075A, 1075B, and 1075C.

Core, section	MTF (°)	Inclination angle
175-1075A-		
4H	203	0.35
5H	304	1.27
6H	356	0.55
7H	356	0.54
8H	327	0.46
9H	39	0.63
10H	194	0.38
11H	126	0.57
12H	19	0.52
13H	334	0.41
14H	68	0.46
15H	83	0.33
16H	101	0.29
17H	55	0.41
18H	314	0.48
19H	56	0.41
20H	355	0.50
21H	119	0.39
22H	34	0.53
175-1075B-		
4H	311	0.41
5H	302	0.61
6H	273	0.42
7H	241	0.34
8H	266	0.52
9H	13	0.50
10H	188	0.37
11H	340	0.37
12H	336	0.13
13H	189	0.32
14H	97	0.55
15H	97	0.39
16H	73	0.45
17H	225	0.42
18H	100	0.55
19H	155	0.52
20H	301	0.28
175-1075C-		
3H	321	3.35
4H	31	2.21
5H	307	2.78
6H	145	2.68
7H	143	2.41
8H	360	2.47
9H	39	2.10
10H	335	2.24
11H	319	2.02
12H	271	1.95
13H	203	1.74
14H	74	1.70
15H	272	1.91

Notes: The orientation parameter (MTF) is the angle in degrees between magnetic north and the double line marked on the center of the working half of the core. The local declination anomaly is 6°W.

der of magnitude stronger. Between 40 and 80 mbsf, the intensity decreases from ~10^{-4} to ~10^{-5} A/m with depth, although no decreasing trend was observed in the magnetic susceptibility. Instead, the magnetic susceptibility gradually decreases with depth below 100 mbsf (Fig. 22). The disagreement of the trend between the remanent intensity and magnetic susceptibility suggests that the magnetic minerals that carry the NRM differ from those that dominate the magnetic susceptibility.

In spite of the overall low intensities of magnetization, a relatively stable magnetic component was preserved in sediments from all three holes, which allows the determination of magnetic polarity. The magnetic moments of the cores were one or two orders of magnitude higher than the noise level of the magnetometer. A magnetic overprint with steep positive inclinations, which was probably acquired during drilling, was usually erased by up to 20-mT demagnetization. However, directions of the NRM show relatively large scatter. This suggests that secondary magnetizations still remain and are probably a viscous remanent magnetization and/or chemical remanent magnetization caused by diagenetic growth or dissolution of magnetic minerals.

Magnetic susceptibility measurements were made on whole cores from all three holes as part of the MST analysis (see "Physical Properties" section, this chapter), except for Core 175-1075C-5H, which was not measured because of deformation of the core liner. Magnetic susceptibility was relatively low, on the order of 10^{-5} (SI volume units; Fig. 22).

Magnetostratigraphy

We identified the polarity of the NRM from the declinations. Because the data from the Tensor orientation tool were available for many cores, we were able to more confidently interpret reversals in terms of the geomagnetic-polarity time scale (Berggren et al., 1995). Changes of inclination with polarity transitions were vague because of the low latitude of this site (an inclination of –10° is expected from the geocentric axial dipole model) and the magnetic overprint (Fig. 21, right panel).

The Brunhes/Matuyama polarity transition (0.78 Ma) occurs between 81 and 86 mbsf at Hole 1075A, 82–84 mbsf at Hole 1075B, and 84–89 mbsf at Hole 1075C (Fig. 21, middle panel). The polarity transition should occur over an interval of ~1 m, assuming a sedimentation rate of ~100 m/m.y. and a polarity transition with 10 k.y. duration. However, the large scatter of the remanent directions made it difficult to determine the exact position of the boundary. The record of Hole 1075B is least affected by the magnetic overprint and gives the clearest polarity boundaries. The termination and beginning of the Jaramillo Subchron (C1r.1n), the ages of which are 0.99 and 1.07 Ma, respectively, occur at ~96.5 mbsf (Core 175-1075A-11H/12H boundary) and 109–113 mbsf at Hole 1075A, at ~98 mbsf and 110–112 mbsf at Hole 1075B, and at 97–98 mbsf and 108–111 mbsf at Hole 1075C. We interpret the normal polarity interval ~170–180 mbsf at Holes 1075A and 1075B as the Olduvai Subchron (C2n, 1.77–1.95 Ma): the upper boundary (termination) at 167–170 mbsf in Hole 1075B and the lower boundary at 182–185 mbsf at Hole 1075A. The upper boundary is unclear for Hole 1075A (between 154 and 176 mbsf) because of the extremely large scatter of the remanent directions. The lower boundary for Hole 1075B and both the upper and lower boundaries for Hole 1075C could not be determined because of the lack of Tensor tool data.

In spite of the high sedimentation rates of ~100 m/m.y., we obtained no evidence for short-duration polarity flips and/or excursions, such as the Blake event, in the Brunhes Chron. Some data points showing anomalous directions can be seen in Figure 21, but they occur at or near the boundaries of cores and/or sections and most probably are caused by disturbance of the sediments.

COMPOSITE SECTION

Continuity of the sedimentary sequence was established over the entire 200 mbsf drilled for three holes at Site 1075. The physical properties data set for Site 1075 included GRAPE density, *P*-wave velocity, and magnetic susceptibility, which were measured on the MST at 2-cm (Hole 1075A) and 4-cm intervals (Holes 1075B and 1075C). Color reflectance data were measured at 2-cm intervals for Hole 1075A and at 4-cm intervals at Holes 1075B and 1075C. At Site 1075, magnetic susceptibility and color reflectance (chromaticity b*) were evaluated as most useful parameters to determine depth offsets between adjacent holes. Sedimentary features common to physical properties measurements of adjacent holes were graphically correlated and aligned to establish a composite depth scale (expressed as mcd), which approximates depth parity at all holes. From the top of the hole, core depths are adjusted by a constant offset relative to mbsf to establish mcd for each core. The depth offsets are tabulated for reference to mbsf in each core (Table 8).

The sediments drilled at Site 1075 contained a high amount of gas that causes numerous voids in and considerable expansion of the
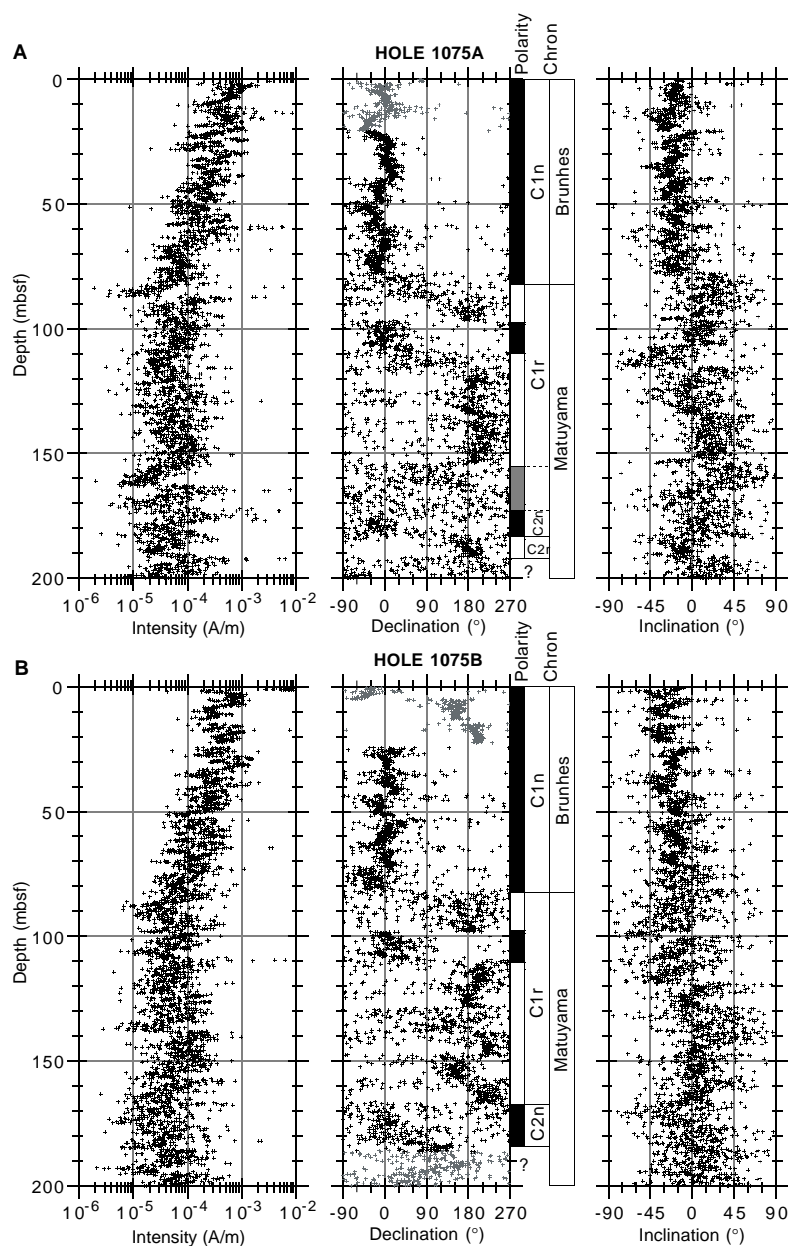
Figure 21. NRM intensity, declination, inclination, and magnetostratigraphic interpretation after 20-mT demagnetization. Black symbols = Tensor corrected; gray symbols = uncorrected. Polarity shading: black = normal, white = reversed, and gray = ambiguous. **A.** Hole 1075A. **B.** Hole 1075B. (Continued on next page.)

cores. Extremely high variability exists in GRAPE densities because of these voids and depth intervals of reduced density, presumably caused by gas bubbles. The gas content also affected *P*-wave measurements. Therefore, GRAPE data were not used to establish the composite depth scale.

The total color reflectance data (lightness L*) of Site 1075 showed small variations but a high noise level. However, chromaticity parameter b* better distinguishes sedimentary features found in the color reflectance record. This parameter also reproduced many of the characteristic features observed in the magnetic susceptibility data from Site 1075 (Figs. 23, 24).

Magnetic susceptibility and chromaticity b* were the key parameters in establishing interhole depth continuity. To generate downhole logs suitable for correlation purposes, the records were extensively filtered. Invalid measurements were eliminated by thresholding the data, followed by additional processing using a linear approximation filter algorithm. For intervals of 10 measurements taken over an interval of 20 to 40 cm, a linear regression and the standard deviation of the data were calculated. Measurements with values outside twice the

standard deviation were reassigned the linearly approximated value. Finally, the data were smoothed using a Gaussian filter with a length of 12 cm. All data shown in Figures 23 and 24 were processed as described above.

The correlation between Holes 1075A and 1075B for the chosen parameters was good or, in some depth intervals, excellent. In a few cases (i.e., Cores 175-1075C-2H and 3H, 175-1075A-4H and 5H, and 175-1075B-3H and 4H), the composite depth scale yields an overlap between successive cores from the same hole (Fig. 23). The gaps between successive cores average ~1.5 m. Large gaps were found between Cores 175-1075B-2H and 3H (~5 m) and 175-1075C-4H, 5H, and 6H (8 and 9 m, respectively).

The spliced record for magnetic susceptibility and color reflectance (b*) is given in Figure 24 (also see Table 9). The two parameters show an excellent correlation in some depth intervals. The growth of the mcd scale compared with the mbsf scale is documented in Figure 25. The spliced section extends to 234.5 mcd (top of Section 175-1075C-22H-CC), which is an ~14% increase to the mbsf scale (top of Section 175-1075C-22H-CC at 207.8 mbsf). Considering the
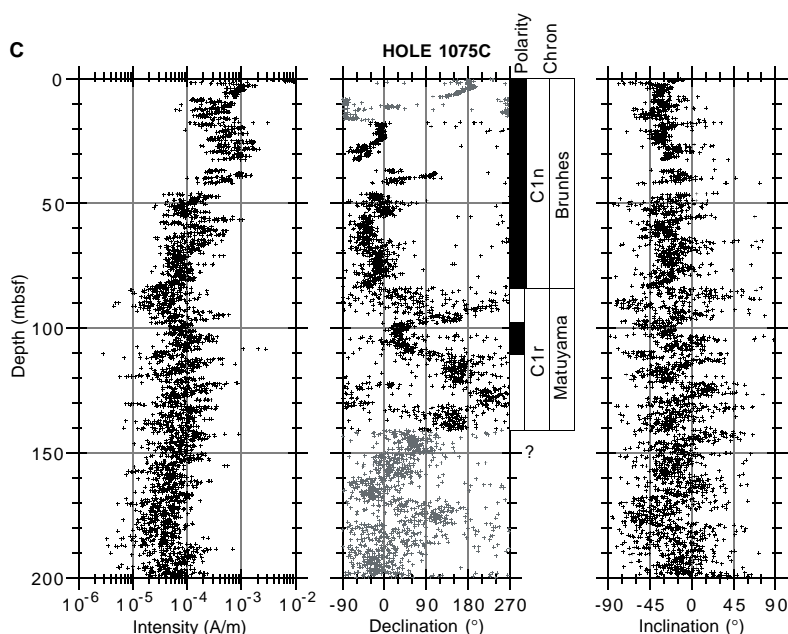
C

HOLE 1075C

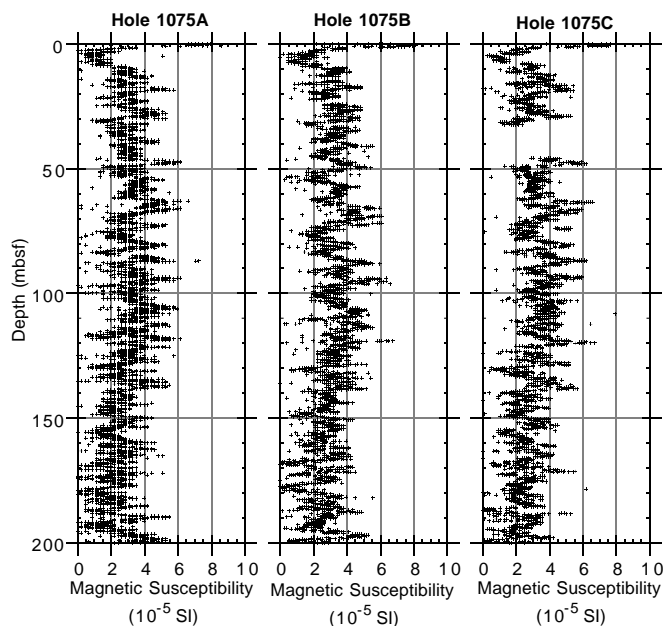Figure 21 (continued). **C.** Hole 1075C.

Figure 22. Magnetic susceptibilities (volume corrected) for Holes 1075A, 1075B, and 1075C.

abundance of voids resulting from gas expansion found at Site 1075 cores, this increase has to be termed "moderate." It should be noted that in the first ~50 mbsf, core expansion is <10%. Below this depth, it is almost 20%. This trend may be related to a higher gas content in the more consolidated sediments below ~50 mbsf.

INORGANIC GEOCHEMISTRY

A total of 44 interstitial water samples were collected from Hole 1075A and analyzed (Table 10). The sampling protocol called for gathering one 10-cm-long whole-round interval from each section of core for the uppermost 60 mbsf, one 10-cm-long whole-round interval from each core from 60 to 100 mbsf, and one 10-cm-long whole-round interval from approximately every third core thereafter. The

shallowest sample was taken from 0.88 mbsf and the deepest from 190.9 mbsf. Headspace samples (see "Organic Geochemistry" section, this chapter) were taken immediately adjacent to each interstitial water whole-round sample, thereby providing a comparable high-resolution data set for volatile hydrocarbons.

Alkalinity, Sulfate, and Ammonium

Downcore profiles of alkalinity, sulfate, and ammonium (Fig. 26) indicate the extent and timing of the degradation of organic matter. As described in the "Organic Geochemistry" section for this site, the sediments from Site 1075 contain elevated levels of TOC, with concentrations averaging 2.6 wt%. This high TOC level is responsible for the high levels of alkalinity within interstitial waters, with a maximum of ~40 mM at 42.4 mbsf. These high alkalinity values are maintained to ~90 mbsf, below which they decrease, perhaps reflecting uptake during diagenetic clay mineral formation or authigenic (Mg-rich) carbonate formation (note that calcium concentrations increase slightly through these depths, as described below). The rate of increase in ammonium is also greatest through the upper 40 mbsf, with continuing increases to the bottom of the hole recording continued degradation of organic matter.

Dissolved sulfate becomes entirely depleted within the uppermost two sections of Core 175-1075A-5H at a depth of ~31 mbsf (Fig. 26). The sharp decrease from seawater values (~29 mM; Millero and Sohn, 1992) at the sediment/water interface to null values at 31 mbsf indicates that the degradation of organic matter has progressed beyond the consumption of oxygen, nitrate, iron, and manganese oxides (e.g., Froelich et al., 1979). Shore-based analyses of dissolved Fe and Mn will lend further insight into the rate of this process.

Calcium, Magnesium, and Strontium

The processes of organic degradation described above also drive carbonate dissolution and precipitation, as monitored by concentration profiles of dissolved Ca^{2+}, Mg^{2+}, and Sr^{2+} (Fig. 27). The strong decreases in Ca^{2+} and Mg^{2+} through the upper 30 mbsf records the presence of a sink for these elements. Likely phases responsible include Mg-rich calcite, dolomite, clays, and authigenic apatite. The increase in dissolved Sr^{2+} over the uppermost 30 mbsf is most likely caused by the dissolution of biogenic calcite, which appears to be less important deeper in the section because Sr^{2+} concentrations increase

Table 8. Offsets applied to cores from Holes 1075A, 1075B, and 1075C.

Core	Depth (mbsf)	Offset (m)	Composite depth (mcd)
175-1075A-			
1H	0.0	0.00	0.00
2H	1.5	0.00	1.50
3H	11.0	0.00	11.00
4H	20.5	1.26	21.76
5H	30.0	0.68	30.68
6H	39.5	1.10	40.60
7H	49.0	2.36	51.36
8H	58.5	3.90	62.40
9H	68.0	5.14	73.14
10H	77.5	6.38	83.88
11H	87.0	7.50	94.50
12H	96.5	9.28	105.78
13H	106.0	10.87	116.87
14H	115.5	11.27	126.77
15H	125.0	13.21	138.21
16H	134.5	14.79	149.29
17H	144.0	15.63	159.63
18H	153.5	17.35	170.85
19H	163.0	19.45	182.45
20H	172.5	20.62	193.12
21H	182.0	22.55	204.55
22H	191.5	25.48	216.98
11H	93.2	7.85	101.05
175-1075B-			
1H	0.0	0.00	0.00
2H	5.0	0.00	5.00
3H	14.5	1.38	15.88
4H	24.0	−0.58	23.42
5H	33.5	−0.28	33.22
6H	43.0	0.40	43.40
7H	52.5	0.19	52.69
8H	62.0	0.90	62.90
9H	71.5	5.66	77.16
10H	81.0	6.37	87.37
11H	90.5	7.23	97.73
12H	100.0	8.71	108.71
13H	109.5	10.20	119.70
14H	119.0	10.91	129.91
15H	128.5	12.46	140.96
16H	138.0	14.30	152.30
17H	147.5	14.97	162.47
18H	157.0	17.78	174.78
19H	166.5	19.83	186.33
20H	176.0	21.84	197.84
21H	185.5	24.51	210.01
22H	195.0	26.73	221.73
175-1075C-			
1H	0.0	0.00	0.00
2H	7.7	1.23	8.93
3H	17.2	0.17	17.37
4H	26.7	−0.14	26.56
5H	33.5	−0.28	33.22
6H	45.7	2.01	47.71
7H	55.2	3.13	58.33
8H	64.7	3.51	68.21
9H	74.2	6.36	80.56
10H	83.7	7.45	91.15
12H	102.7	8.15	110.85
13H	112.2	11.16	123.36
14H	121.7	12.13	133.83
15H	131.2	14.13	145.33
16H	140.7	14.49	155.19
17H	150.2	16.41	166.61
18H	159.7	18.62	178.32
19H	169.2	20.01	189.21
20H	178.7	22.47	201.17
21H	188.2	23.91	212.11
22H	197.7	26.78	224.48

Note: The offsets transform ODP standard depth values in meters below seafloor (mbsf) to meters composite depth (mcd).

only minimally downhole. The degradation of the organic matter provides the alkalinity necessary for the precipitation of diagenetic carbonate phases. Considering the strong decreases in dissolved Ca^{2+} and Mg^{2+}, it appears that dolomite may be forming throughout the uppermost portions of the section. The molar consumption of Ca^{2+} and Mg^{2+} during dolomite formation should be the same. The potential involvement of dual mechanisms causing the drawdown of dissolved Mg^{2+} (described below) makes it unclear at this point whether additional authigenic phases are precipitating. The most likely potentially additional precipitating phase is authigenic apatite.

To separate the potential Mg^{2+} sinks of dolomitization and clay formation from each other we have extended the deeper trend (at depths >100 mbsf) of Mg^{2+} depletion stratigraphically up to the bottom-water value of 53 mM (Fig. 27). We suggest that this trend reflects the Mg^{2+} sink from clay mineral uptake; if so, the extent of Mg^{2+} drawdown in excess of this (represented in Fig. 27 by the shaded region sandwiched between the "clay uptake line" and the observed data) would be caused by dolomite formation. Postcruise mass balance calculations of the Ca^{2+}, Mg^{2+}, and Sr^{2+} budgets will provide constraints on authigenic carbonate formation.

Silica and Phosphate

Diagenetic changes involving biogenic and organic matter are also recorded by the downcore profiles of dissolved silica and phosphate (Fig. 28). The concentration of dissolved silica increases dramatically through the uppermost 10 m of sediment, recording the dissolution of opal-A, which is predominantly supplied to these sediments by diatoms (see "Lithostratigraphy" and "Biostratigraphy and Sedimentation Rates" sections, this chapter). The concentration of dissolved silica continues to gradually increase downcore, recording the continued dissolution of opal, which remains present into the deepest sections of the sequence (see "Biostratigraphy and Sedimentation Rates" section, this chapter).

Dissolved phosphate increases to maximum values between 50 and 60 mbsf and decreases to the bottom of the hole. Although more sharply defined than the broad alkalinity maximum (Fig. 26), the general correspondence between the phosphate and alkalinity profiles indicates that the phosphate is being released from organic matter during degradation. If authigenic apatite is forming within the upper 60 mbsf, it must do so at a rate that removes dissolved phosphate more slowly than it is being released by organic degradation. The decrease in concentration from 60 to 190 mbsf records uptake either into authigenic phosphate phases or by adsorption onto other mineral surfaces. Very fine-grained authigenic sedimentary phases (see "Lithostratigraphy" section, this chapter) could not be uniquely identified as phosphatic minerals; additional shore-based analyses will specifically target identification of the precise sink for the dissolved phosphate at this site.

Sodium and Potassium

Concentrations of both dissolved Na^+ and K^+ increase with depth downcore (Fig. 29). The concentration of Na^+ shows a rapid increase near the surface. It is important to recall, however, that Na^+ is determined via charge balance, and this increase may merely reflect the paired increase in dissolved Cl^-, as discussed below.

Salinity and Chloride

The downcore profiles of salinity and dissolved Cl^- show subtle variations (Fig. 30). The decrease in salinity is slight, from values of 35.5‰ near the sediment/water interface to 34‰ at depth. (The resolution of the hand-held refractometer is 0.5‰; thus, a smooth decrease appears as a stepped change.) The stepwise decrease in data shown probably represents a smooth decrease from values of 35.5‰ near the sediment/water interface to 34‰ at depth. The decrease in salinity appears to be caused by the decrease in dissolved sulfate, Ca^{2+}, and Mg^{2+}; note that chlorinity does not follow the trend. Despite the high methane concentrations at this site (see "Organic Geochemistry" section, this chapter), the decrease in salinity is in all probability not related to decomposition of solid methane hydrate. Decomposition of hydrate typically causes a far greater decrease in salinity (to values <28‰) than is observed.

Chloride concentrations increase sharply to maximum values at ~40 mbsf before becoming essentially constant for the rest of the profile (Fig. 30). Chloride concentrations are derived from the highly
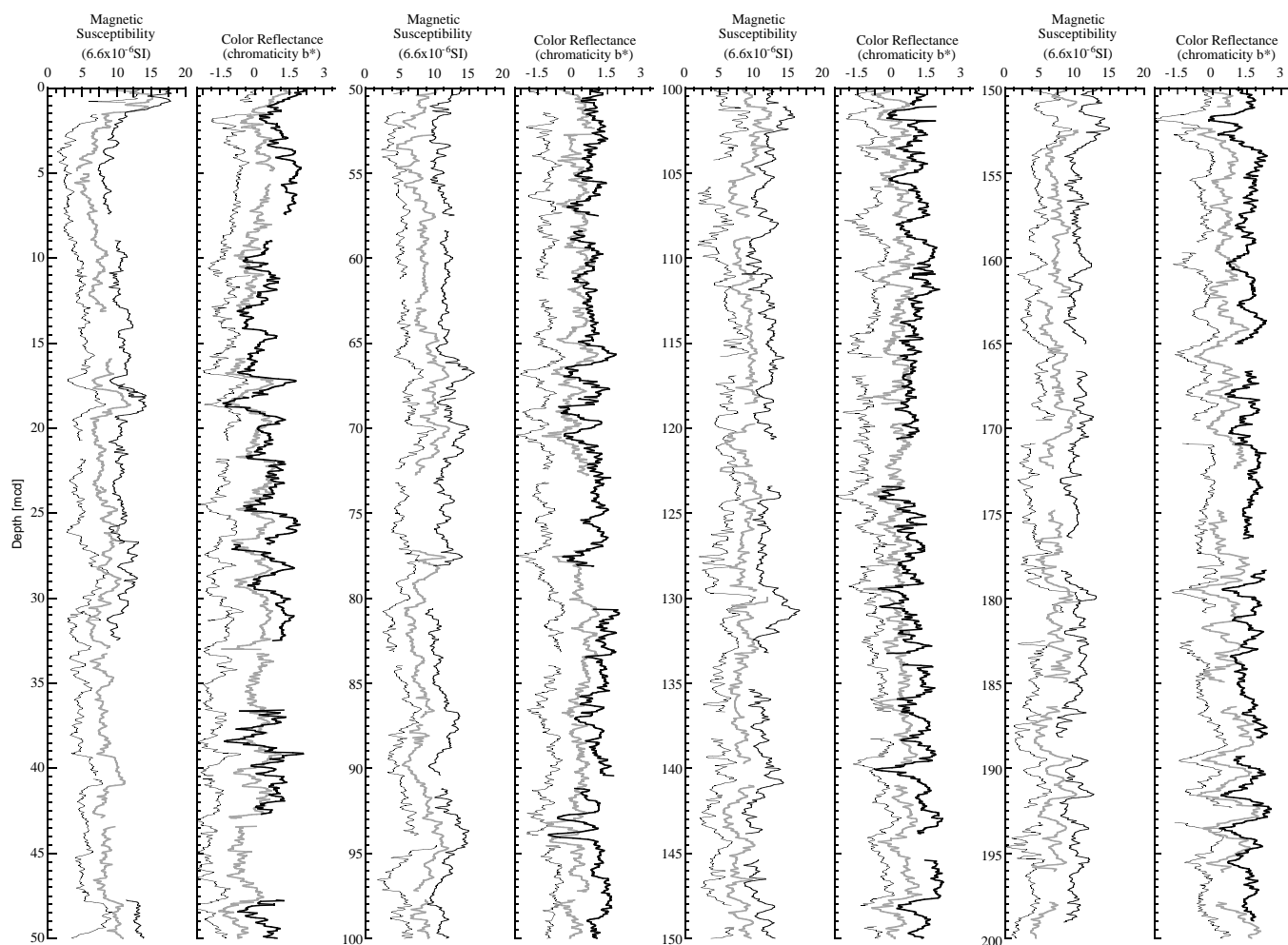
Figure 23. Composite section for Site 1075. Magnetic susceptibility and color reflectance (chromaticity b*) are plotted for Holes 1075A (thin black line), 1075B (gray line), and 1075C (thick black line). Downhole logs are shown in meters composite depth (mcd). Offsets have been applied for clarity.

precise titration method; measurements using the less precise but similarly accurate Dionex instrument (Table 10) confirm this pattern. This increase is not caused by brine formation or other simple subseafloor dilution effects, nor is it monitoring substantial diagenetic release(s) because Cl^- is known to behave largely conservatively. Instead, the increase most likely reflects a stacked diffusional signal of seawater Cl^- from glacial periods where seawater had higher salinity because of the formation of the ice caps. The increase in dissolved Cl^- is ~2%–3% of the measured value, which compares well with the volume of water removed from the oceans and transferred to the ice caps. This effect does not show in the salinity measurements because the pore-water salinity is a summation of all dissolved constituents. Previous ODP legs have also documented a marked increase in dissolved Cl^- through the uppermost sections, with maximum values approximately comparable to those observed here. Shore-based analyses with greater analytical precision will further quantify the extent of salinity changes during glaciations.

ORGANIC GEOCHEMISTRY

Calcium carbonate and organic carbon concentrations were measured on sediment samples from Hole 1075A (Table 11). Organic matter atomic carbon/nitrogen (C/N) ratios and Rock-Eval pyrolysis analyses were employed to determine the type of organic matter contained within the sediments. High headspace and core void gas contents were encountered, and routine monitoring of the sedimentary gases was done for drilling safety.

Inorganic and Organic Carbon Concentrations

Concentrations of carbonate carbon are low in Site 1075 sediments. They vary between 2.1 and <0.1 wt% (Table 11). The maximum carbonate carbon concentration is equivalent to 17 wt% sedimentary $CaCO_3$, and most sediment samples contain less than a few weight percent $CaCO_3$. These generally low concentrations agree with the paucity of coccoliths and the high abundances of opaline material and continental clastic sediments at this site (see "Biostratigraphy and Sedimentation Rates" section, this chapter). The range in concentrations reflects a varying combination of changes in biological production of calcareous material, dilution by noncalcareous components, and carbonate dissolution fueled by oxidation of organic matter.

TOC determinations were done on a smaller number of Hole 1075A sediment samples than carbonate determinations because of time constraints. TOC values range from 4.42 to 0.96 wt% (Table 11)
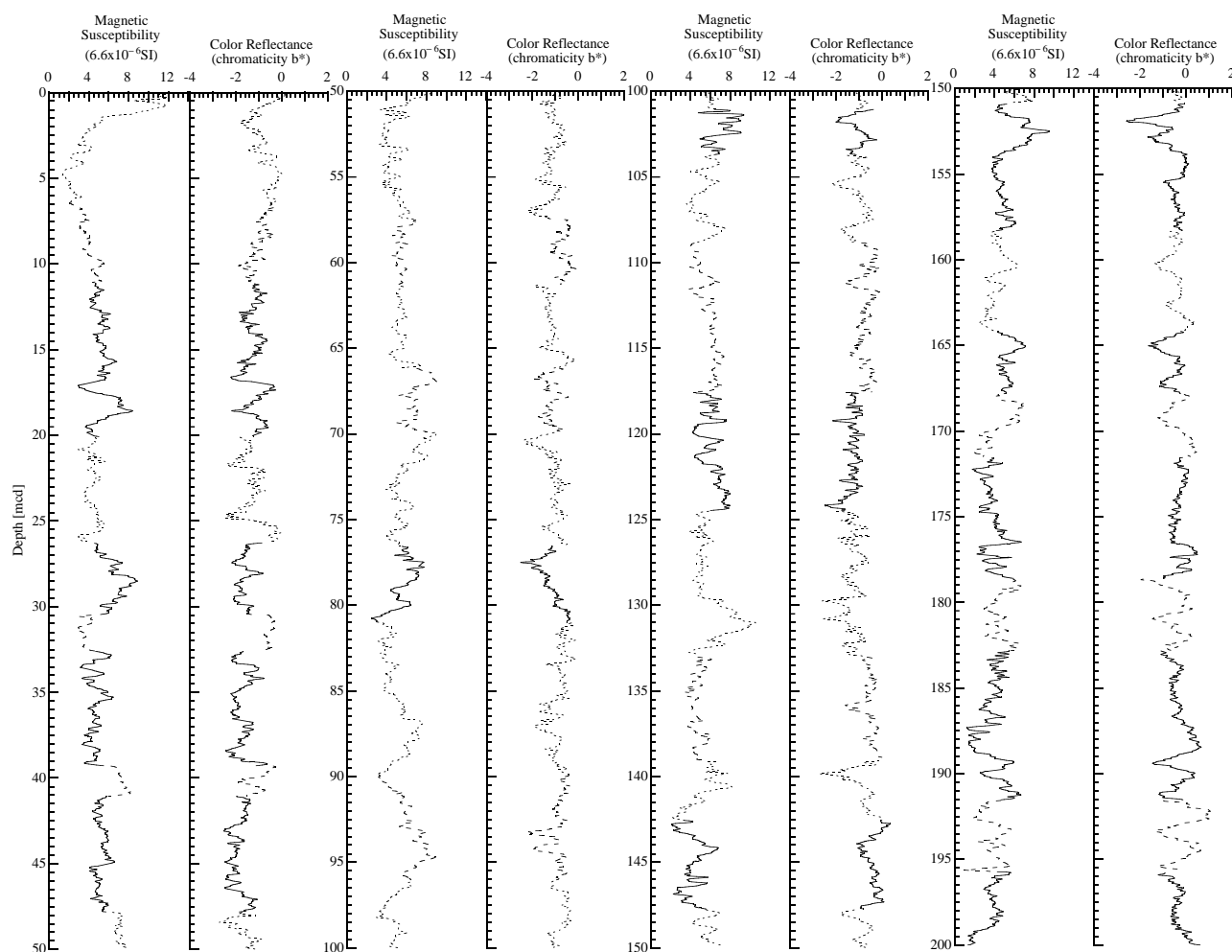
Figure 24. Spliced records for magnetic susceptibility and color reflectance (chromaticity b*) plotted in meters composite depth (mcd). Cores from all three holes at Site 1075 have been used for the spliced record: solid line = Hole 1075A, dashed line = Hole 1075B, and dotted line = Hole 1075C.

and average 2.60 wt%. The concentrations are ~10 times greater than the average of 0.3 wt% given by McIver (1975), based on Deep Sea Drilling Project (DSDP) Legs 1–33, a value that can be considered representative of typical deep-sea sediments. The high TOC concentrations at this site may be ascribed to a combination of high supply from elevated paleoproductivities and a high accumulation rate of sediments enhancing organic matter preservation.

Organic Matter Source Characterization

Organic C/N ratios were calculated for Site 1075 samples using TOC and total nitrogen concentrations to help identify the origin of their organic matter. Site 1075 C/N ratios vary from 21.2 to 6.6 (Table 11). Lower C/N ratios occur in samples that contain less organic carbon; these values may be biased by the tendency of clay minerals to absorb ammonium ions generated during the degradation of organic matter (Müller, 1977; see "Inorganic Geochemistry" section, this chapter).

The C/N ratios average 12.6, a value that is intermediate between unaltered algal organic matter (5–8) and fresh land-plant material (25–35; e.g., Emerson and Hedges, 1988; Meyers, 1994). These organic carbon–rich sediments probably contain a mixture of partially degraded algal material and detrital continental organic matter. Pref-

erential loss of nitrogen-rich, proteinaceous matter can elevate the C/N ratios of algal organic matter during settling to the seafloor (Meyers, 1997).

A Van Krevelen–type plot of the hydrogen index (HI) and oxygen index (OI) values indicates that the sediments contain a mixture of type II (algal) and type III (land-derived) organic matter (Fig. 31). This source assignment for the organic matter is consistent with the intermediate C/N ratios for these samples, which also suggest that the organic matter is a mixture of marine and continental material. A more likely possibility, however, is that the sediments principally contain algal-derived organic matter that has been altered by microbial processing during early diagenesis. Well-preserved type II organic matter has high HI values (Peters, 1986), which can be lowered by microbial oxidation (Meyers, 1997). The low HI values of fresh type III organic matter, however, cannot become elevated by post-depositional alteration. In general, Hole 1075A sediments having higher Rock-Eval TOC values also have higher HI values (Table 12). This relationship confirms that the algal organic matter has been oxidized. Variable T_{max} values reflect poorly defined S_2 peaks and not actual thermal maturities of organic matter. Those samples in which the geometry of S_2 peaks was sharp have relatively low T_{max} values (Table 12), showing that organic matter is thermally immature with respect to petroleum generation (Peters, 1986) and therefore contains

Table 9. List of splice tie points used to create the continuous "spliced" stratigraphic sequence for Site 1075.

Hole, core, section, interval (cm)	Depth (mbsf)	Composite depth (mcd)	Whether tied	Hole, core, section, interval (cm)	Depth (mbsf)	Composite depth (mcd)	Offset (m)
1075C-1H-5, 40	6.40	6.40	Tie to	1075B-2H-1, 116	6.16	6.40	0.24
1075B-2H-4, 138	10.88	11.12	Tie to	1075A-3H-1, 14	11.14	11.12	–0.02
1075A-3H-7, 10	20.10	20.08	Tie to	1075C-3H-2, 120	19.90	20.08	0.18
1075C-3H-6, 132	26.02	26.20	Tie to	1075A-4H-3, 144	24.94	26.20	1.26
1075A-4H-6, 120	29.20	30.46	Tie to	1075B-4H-5, 104	31.04	30.46	–0.58
1075B-4H-7, 16	33.16	32.58	Tie to	1075A-5H-2, 40	31.90	32.58	0.68
1075A-5H-6, 110	38.60	39.28	Tie to	1075B-5H-5, 5	39.56	39.28	–0.28
1075B-5H-6, 32	41.32	41.04	Tie to	1075A-6H-1, 44	39.94	41.04	1.10
1075A-6H-5, 122	46.72	47.82	Tie to	1075C-6H-1, 10.5	45.81	47.82	2.01
1075C-6H-7, 76	55.46	57.47	Tie to	1075B-7H-4, 20	57.20	57.47	0.27
1075B-7H-6, 100	61.00	61.27	Tie to	1075C-7H-2, 144	58.14	61.27	3.13
1075C-7H-6, 32	63.02	66.15	Tie to	1075B-8H-3, 23.5	65.25	66.15	0.90
1075B-8H-5, 100	69.00	69.90	Tie to	1075C-8H-2, 18.5	66.39	69.90	3.51
1075C-8H-6, 84	73.04	76.55	Tie to	1075A-9H-3, 40.5	71.41	76.55	5.14
1075A-9H-6, 28	75.86	81.00	Tie to	1075C-9H-1, 44	74.64	81.00	6.36
1075C-9H-7, 32	83.52	89.88	Tie to	1075B-10H-2, 99.5	83.51	89.88	6.37
1075B-10H-6, 104	89.54	95.91	Tie to	1075C-10H-4, 4	88.24	95.91	7.67
1075C-10H-7, 68	93.38	101.05	Tie to	1075A-11H-5, 106	93.56	101.05	7.49
1075A-11H-7, 84	96.22	103.71	Tie to	1075C-11H-2, 112	95.82	103.71	7.89
1075C-11H-6, 24	100.94	108.83	Tie to	1075B-12H-1, 20	100.20	108.83	8.63
1075B-12H-6, 144	108.92	117.55	Tie to	1075A-13H-1, 50	106.50	117.55	11.05
1075A-13H-5, 142	113.42	124.47	Tie to	1075C-13H-1, 80	113.00	124.47	11.47
1075C-13H-7, 32	121.52	132.99	Tie to	1075B-14H-3, 36	122.36	132.99	10.63
1075B-14H-7, 44	128.44	139.07	Tie to	1075B-14H-4, 100	127.18	139.07	11.89
1075C-14H-6, 144	130.62	142.51	Tie to	1075A-15H-4, 126	129.44	142.51	13.07
1075A-15H-8, 70	134.68	147.75	Tie to	1075C-15H-2, 108	133.78	147.75	13.97
1075C-15H-4, 116	136.86	150.83	Tie to	1075A-16H-1, 146	135.96	150.83	14.87
1075A-16H-6, 144	143.44	158.31	Tie to	1075C-16H-3, 20	143.90	158.31	14.41
1075C-16H-7, 4	149.74	164.15	Tie to	1075A-17H-4, 66	149.16	164.15	14.99
1075A-17H-6, 132	152.82	167.81	Tie to	1075B-17H-5, 116	153.50	167.81	14.31
1075B-17H-8, 32	157.16	171.47	Tie to	1075A-18H-1, 144	154.94	171.47	16.53
1075A-18H-6, 134	162.07	178.60	Tie to	1075B-18H-4, 84	161.62	178.60	16.98
1075B-18H-7, 56	165.84	182.82	Tie to	1075A-19H-1, 52	163.52	182.82	19.30
1075A-19H-7, 22	172.22	191.52	Tie to	1075B-19H-4, 88	171.88	191.52	19.64
1075B-19H-7, 56	176.06	195.70	Tie to	1075A-20H-3, 28	174.69	195.70	21.01
1075A-20H-8, 34	182.22	203.23	Tie to	1075B-20H-5, 24	181.27	203.23	21.96
1075B-20H-8, 28	185.81	207.77	Tie to	1075A-21H-3, 64	185.64	207.77	22.13
1075A-21H-6, 42	189.92	212.05	Tie to	1075B-21H-3, 44	188.04	212.05	24.01
1075B-21H-7, 132	194.92	218.93	Tie to	1075A-22H-2, 106	194.06	218.93	24.87
1075A-22H-6, 132	200.32	225.19	Tie to	1075B-22H-3, 64	198.64	225.19	26.55
1075B-22H-5, 112	202.12	228.67	Tie to	1075C-22H-4, 128	202.17	228.67	26.50
1075C-22H-8, 84	207.73	234.23					

Note: The tie points are listed in standard ODP meters below seafloor (mbsf) and meters composite depth (mcd).

little detrital organic matter derived from erosion of ancient sediments and transported to this site by the Congo River.

Headspace Gases

Sediments from Hole 1075A were very gaseous. Gas pressures became great enough in sediments below Core 175-1075A-15H (125 mbsf) to require perforating the core liner to relieve the pressure and alleviate core expansion. Natural gas analyses determined that much of this gas was CO_2 (Table 13). Hydrogen sulfide could be detected by nose, but not by hydrogen sulfide–sensing instruments having a sensitivity of ~1 ppm, in Cores 175-1075A-3H through 6H (12.5–48.5 mbsf).

Methane (C_1) first appears in headspace gas samples in Hole 1075A sediments at 12.5 mbsf. Concentrations gradually increase and become significant in sediments below 30 mbsf (Fig. 32). Two sources of the gas are possible. First, gas from some deeper origin may have migrated into the unit. Evidence for migration of methane into porous sediments from deeper sources has been found at Sites 762 and 763 on the Exmouth Plateau where a thermogenic source exists in underlying Jurassic rocks (Meyers and Snowdon, 1993). Mesozoic sources of thermogenic gas are known on the southwest African margin from ongoing exploration. A second possible source is in situ formation by methanogenic microorganisms. High methane/ethane (C_1/C_2) ratios and the absence of major contributions of higher molecular weight hydrocarbon gases (Table 13) indicate that the gas is biogenic, as opposed to thermogenic, in origin. The origin of the

methane is probably from in situ microbial fermentation of the marine organic matter present in the sediments. Similar microbial production of methane from marine organic matter has been inferred from high biogenic gas concentrations in Pliocene–Pleistocene sediments from DSDP Site 532 on the Walvis Ridge (Meyers and Brassell, 1985), Sites 897 and 898 on the Iberian Abyssal Plain (Meyers and Shaw, 1996), and also in middle Miocene sediments from Site 767 in the Celebes Sea (Shipboard Scientific Party, 1990). A biogenic origin of the methane is supported by the disappearance of interstitial sulfate at approximately the same sub-bottom depth where methane concentrations begin to rise (see "Inorganic Geochemistry" section, this chapter). As noted by Claypool and Kvenvolden (1983), the presence of interstitial sulfate inhibits methanogenesis in marine sediments.

PHYSICAL PROPERTIES

An intensive physical properties program was conducted at Site 1075. Sound velocity, gamma ray-attenuation, and magnetic susceptibility were measured with the MST (see "Explanatory Notes" chapter, this volume). Thermal conductivity was measured with the needle probe on every second section of each core. On split cores, discrete measurements of ultrasonic velocities and shear strength were carried out. Two discrete sediment samples per section were taken for index properties analysis such as porosity and wet bulk density. The results were compared with seismic profiles obtained from previous
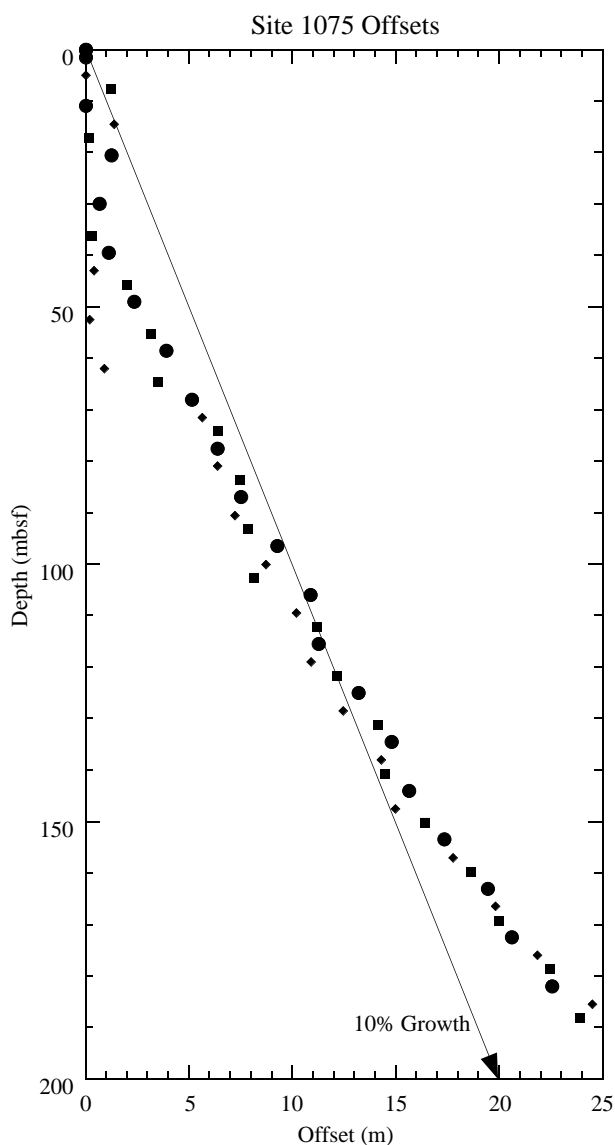
Figure 25. Core offsets applied to Site 1075 plotted against standard ODP meters below seafloor (mbsf). A linear 10% growth of meters composite depth (mcd) compared with mbsf is indicated by an arrow. Offsets are plotted for Holes 1075A (circles), 1075B (diamonds), and 1075C (squares).

investigations in this area (see "Site Geophysics" sections, "Site 1075," "Site 1078," "Site 1080," "Site 1081," "Site 1084," "Site 1085," and "Site 1086" chapters, this volume).

Multisensor Track

All core sections were routinely measured on the MST. Hole 1075A was measured at 2-cm intervals, and Holes 1075B and 1075C were measured at 4-cm intervals because of time constraints. MST data are included on CD-ROM (back pocket, this volume). The top and bottom 4 cm of each core were not measured. The large scatter in GRAPE density data below 50 mbsf is caused by the large number of small gas voids. The data were despiked and smoothed to prepare for visual inspection. An example of the data quality and the improvement by data processing is given (Fig. 33) for unfiltered and filtered GRAPE density.

Filtered GRAPE density data are compared with discrete wet bulk density data (see below; Fig. 34). Density values obtained with the MST system and from index properties measurements correlate well. All major features of density variations are also seen in index properties and also correlate with other physical and lithologic parameters and observations. Density increases gradually between 0 and 90 mbsf because of sediment compaction and dewatering. Below 100 mbsf, discrete density values decrease. GRAPE density shows large variations, but values are lower than the discrete density values. This is explained by an increasing proportion of gas charge of the sediment pores and/or the presence of small voids and cracks and/or air between the sediment and the core liner. A careful reconstruction and splice of undisturbed intervals is required from core photos, visual inspection, and by comparison with other MST data to provide optimum records and data sets suitable for calculation of synthetic seismograms and studies of sedimentary cycles.

Toward the bottom of the hole, a significant density increase is observed, which can be tentatively correlated with the strongest seismic reflector in the vicinity of the drill site within the cored depth range (see "Site Geophysics" section, this chapter). The characteristics of the average density profile correspond with the P-wave velocities, which could be measured at this site down to ~120 mbsf (Fig. 35). MST records of P-wave velocity are thoroughly filtered and limited to values in the expected range.

Magnetic susceptibility (Fig. 36A) is positively correlated with GRAPE and wet bulk density (Fig. 34), which may be attributed to a varying proportion of biogenic opal vs. clay in the sediment. Also, a good correlation of magnetic susceptibility and reflectance measurements, mainly the chromaticity (b*), can be found (see "Lithostratigraphy" and "Composite Section" sections, this chapter). Magnetic susceptibility reveals a pronounced cyclicity, which could be further used to identify astronomically controlled depositional processes in the region of the Congo River.

Velocity

Compressional ultrasonic (P-wave) velocities were obtained on the split-core sections. The discrete measurements were performed with the digital sediment velocimeter (DSV1; see "Explanatory Notes" chapter, this volume) at a sample frequency of two per section. This system was used down to ~45 mbsf. Below that depth, the transducer arms could not penetrate the sediment without creating fractures, which inhibited the undisturbed sound transmission. Below 45 mbsf, the modified Hamilton Frame was used. Signals were completely attenuated at a depth of ~120 mbsf. In general, signal attenuation was observed to be higher in the upper sections of each core than in the lower portion.

As expected for the sediment type, velocities vary between 1460 m/s in the soft surface sediments and 1570 m/s in the more consolidated sediments. The peak in velocities corresponds to the peak in vane shear strength at 70 mbsf. Detailed analyses of velocity profiles will be possible after shore-based investigation of grain size, carbonate content, and crystallinity. Vane shear strength, velocity, and porosity are sensitive indicators for the change in rigidity of the sediment matrix caused by a different degree of cementation. A comparison of the continuous velocity profile obtained with the MST and discrete values is shown in Figure 35.

Thermal Conductivity

Thermal conductivity was measured in every second section of each core (Fig. 36B). Values decrease with depth, corresponding to the decreasing porosity (Fig. 37B).

Table 10. Interstitial water composition for Hole 1075A.

Core, section, interval (cm)	Depth (mbsf)	pH	Alkalinity (mM)	Salinity	Cl⁻ (titr) (mM)	Cl⁻ (IC) (mM)	SO_4^{2-} (mM)	Na^+ (mM)	Mg^{2+} (mM)	Ca^{2+} (mM)	K^+ (mM)	H_4SiO_4 (µM)	NH_4^+ (µM)	PO_4^{3-} (µM)	Sr^{2+} (µM)
175-1075A-															
1H-1, 88-98	0.88	7.83	1.776	35.5	552	550	27.76	470	52.6	10.3	13.1	511	206	6	91
2H-1, 140-150	2.90	7.78	4.281	35.5	553	550	27.51	474	52.6	9.9	12.5	683	322	10	92
2H-1, 140-150	4.40	7.65	4.697	35.5	554	553	28.35	476	53.5	9.9	12.8	750	375	13	91
2H-3, 140-150	5.90	7.72	5.524	35.5	555	548	26.44	477	52.3	9.8	12.2	779	542	26	93
2H-4, 140-150	7.40	7.71	7.132	35.5	558	553	25.56	480	52.3	9.5	12.7	822	654	27	93
2H-5, 140-150	8.90	7.77	8.144	35.5	558	549	25.19	482	51.5	9.5	12.5	808	858	28	93
2H-6, 140-150	10.40	7.41	10.504	35.5	558	553	25.00	483	52.1	9.2	13.0	826	885	44	93
3H-1, 140-150	12.40	7.83	13.039	35.5	557	553	22.10	481	51.0	9.0	12.9	768	1265		94
3H-2, 140-150	13.90	7.20	14.514	35.5	559	556	20.65	484	50.2	8.8	13.4	764	1273		95
3H-3, 140-150	15.40	7.82	15.601	35.5	559	555	17.70	483	49.3	8.0	12.6	750	1312		96
3H-5, 140-150	18.40	7.92	21.715	35.0	562	557	13.55	484	48.9	7.6	13.1	359	1575		97
3H-6, 140-150	19.90	7.99	22.418	35.0	563	562	12.14	484	49.0	7.4	13.2	781	1703	46	100
4H-1, 140-150	21.90	7.81	26.647	35.0	566	563	9.55	488	48.9	6.6	12.7	766	1847	44	102
4H-2, 140-150	23.40	8.50	28.342	35.0	564	562	7.34	485	48.1	6.6	12.7	638	1975		104
4H-3, 140-150	24.90	7.96	29.976	35.0	563	566	5.57	485	47.4	6.3	12.4	764	1726	67	106
4H-4, 140-150	26.40	8.00	32.495	35.0	564	563	3.88	483	47.7	6.4	12.8	739	1854	26	107
4H-5, 140-150	27.90	8.02	34.615	35.0	563	567	2.71	484	47.1	6.1	12.6	759	1901	64	108
4H-6, 140-150	29.40	7.97	36.021	35.0	566	565	1.35	487	46.5	5.9	12.5	759	2073	62	112
5H-1, 140-150	31.40	8.20	37.027	34.5	567	560	0.08	490	45.4	5.3	12.5	772	2194		118
5H-2, 140-150	32.90	7.90	36.518	35.0	565	561	0.00	486	46.2	5.5	12.4	786	2141	61	120
5H-3, 140-150	34.40	7.98	37.827	35.0	565	565	0.00	488	45.6	5.5	12.6	793	2156	76	122
5H-4, 140-150	35.90	7.94	37.028	35.0	567	564	0.01	490	45.5	5.3	12.4	775	2254	72	124
5H-5, 140-150	37.40	7.56	35.159	35.0	567	560	0.00	487	45.4	5.5	13.1	768	2699		125
5H-6, 140-150	38.90			35.0	565	567	0.00	452	44.7	5.5	13.1	806	2669		120
6H-1, 140-150	40.90	8.02	37.965	35.0	573	567	0.00	497	45.4	5.4	12.7	790	2473	61	124
6H-2, 140-150	42.40	8.11	40.033	35.0	568	564	0.28	493	45.7	5.4	12.9	777	2669	36	120
6H-3, 140-150	43.90	7.84	38.094	35.0	565		0.00					705	2556		123
6H-4, 140-150	45.40	7.46	37.989	34.5	565	564	0.00	492	44.0	5.1	12.9	815	3001	102	124
6H-5, 140-150	46.90	7.49	37.362	34.5	564	569	0.00	489	44.1	5.6	13.2	788	2556	97	121
6H-6, 140-150	48.40	8.12	38.301	34.5	566	552	0.00	491	44.7	5.2	12.9	797	2578	100	122
7H-1, 140-150	50.40	7.60	37.752	34.5	563	569	0.00	487	44.8	5.6	13.0	902	2903	133	118
7H-2, 140-150	51.90	7.79	37.710	34.5	565	566	0.31	489	45.3	5.7	12.6	802	2888	125	117
7H-3, 140-150	53.43	7.78	38.727	34.5	561	562	0.39	488	44.4	5.6	13.1	831	2910	120	123
7H-4, 140-150	54.97	8.15	39.312	34.5	566	571	0.00	491	44.6	6.0	13.1	835	3582	124	124
7H-5, 140-150	56.47	7.77	39.583	34.5	558	572	0.00	486	43.7	5.5	13.4	828	3522	133	123
7H-6, 140-150	57.97	7.86	37.508	34.5	564	571	0.06	489	44.2	5.6	12.9	857	2933	134	121
8H-3, 140-150	62.95	7.77	40.446	34.5	561	561	0.00	488	44.1	5.6	13.3	824	3212	122	123
9H-3, 140-150	72.40	7.59	41.518	34.5	564	572	0.00	492	43.8	5.7	13.9	848	3386	95	123
10H-3, 120-130	81.70	7.42	41.382	34.5	564	568	0.00	496	42.4	5.6	13.7	875	3839	77	123
11H-3, 120-130	90.88	7.70	41.148	34.5	565	561	0.00	495	43.1	6.0	13.5	866	3952	72	126
12H-3, 150-160	101.00	7.76	40.225	34.5	563	564	0.00	493	42.2	5.8	13.6	877	4246	68	127
15H-3, 120-130	128.08	7.23	36.349	34.5	564	559	0.19	497	39.5	5.8	13.6	882	4805	51	126
18H-3, 120-130	157.70	7.70	34.575	34.0	568	565	0.00	502	37.0	6.2	13.8	1038	5295	88	126
21H-6, 140-150	190.90	7.56	34.828	34.0	568	574	0.00	508	34.0	6.5	13.7	1003	6087	54	128

Notes: Cl⁻ (titr) = analyzed by titration; Cl⁻ (IC) = analyzed by ion chromatography. Empty cells = not analyzed.
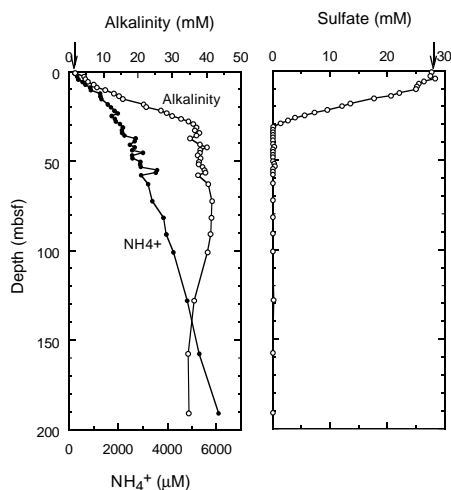

Figure 26. Downcore profiles of dissolved alkalinity, sulfate, and ammonium at Hole 1075A. Arrows = mean ocean-bottom-water values taken from Millero and Sohn (1992).
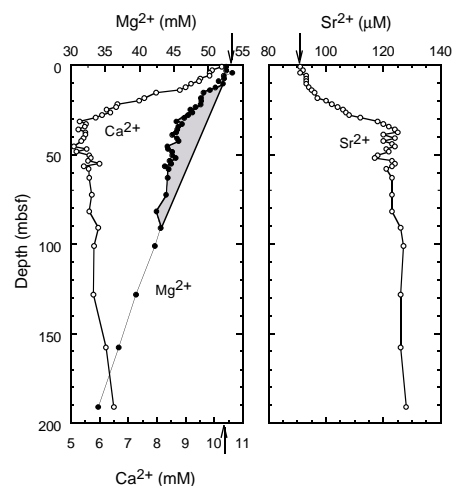

Figure 27. Downcore profiles of Ca^{2+}, Mg^{2+}, and Sr^{2+} at Hole 1075A. Shaded region associated with Mg^{2+} profile = the removal of Mg^{2+}, suggested to be caused by dolomite formation. Arrows = mean ocean-bottom-water values taken from Millero and Sohn (1992).
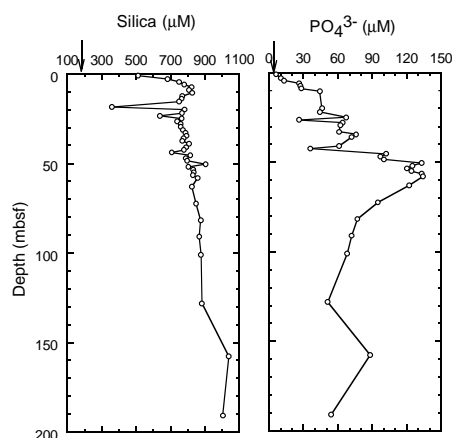
Figure 28. Downcore profiles of dissolved silica and phosphate at Hole 1075A. Arrows = mean ocean-bottom-water values taken from Millero and Sohn (1992).
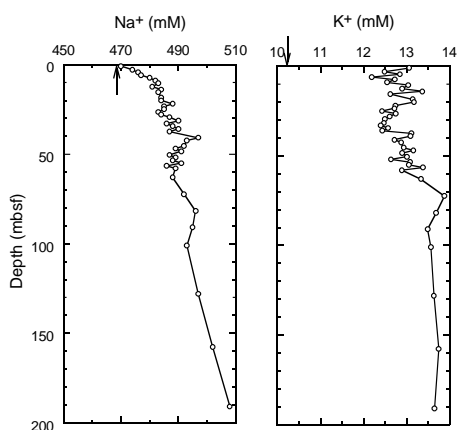

Figure 29. Downcore profiles of dissolved Na$^+$ and K$^+$ at Hole 1075A. Arrows = mean ocean-bottom-water values taken from Millero and Sohn (1992).
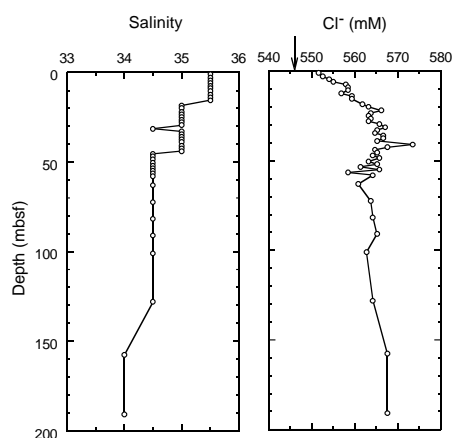

Figure 30. Downcore profiles of salinity and dissolved Cl$^-$ at Hole 1075A. Arrows = mean ocean-bottom-water values taken from Millero and Sohn (1992).

Vane Shear Strength

Measurements were taken according to the procedure outlined in the "Explanatory Notes" chapter (this volume). The results are displayed in Figure 36C, together with magnetic susceptibility (Fig. 36A) and thermal conductivity (Fig. 36B). On average, values increase gradually down to a depth of 95 mbsf, with larger fluctuations within the gas-bearing interval from 60 to 95 mbsf. A significant decrease occurs below 115 mbsf, but no data are available for the depth range between 95 and 115 mbsf. One possible explanation for these unusual characteristics is failure of the sediment matrix caused by high pressure and/or deformation, or expansion of large amounts of dissolved gas during core retrieval.

Index Properties

Index properties, calculated from the weight and volume data using the pycnometer (see "Explanatory Notes" chapter, this volume), are wet bulk density, porosity, and moisture content. The density data correlate very well with the GRAPE data and can be used to calibrate and correct the GRAPE density (Fig. 34). Water content varies between 55% and 80% (Fig. 37C), porosity between 70% and 90% (Fig. 37B), and density values range between 1.200 and 1.450 kg/m^3 (Fig. 37A; also see Table 14 on CD-ROM, back pocket, this volume).

Summary

The intensive physical properties program measured at this site will be used for the detailed high-resolution analyses of cycles and temporal changes in sediment composition and for the construction of synthetic seismograms after thorough data processing. Detailed studies connecting these parameters with the physical and chemical state of the sediment and the responsible paleoceanographic events will be conducted on shore. Coring disturbance in the upper sections of the cores is apparent in most measurements, which will require careful evaluation of core and data quality before applying numerical methods on these data sets.

REFERENCES

Bé, A.W.H., and Tolderlund, D.S., 1971. Distribution and ecology of living planktonic foraminifera in surface waters of the Atlantic and Indian Oceans. *In* Funnel, B.M., and Riedel, W.R. (Eds.), *The Micropaleontology of Oceans:* Cambridge (Cambridge Univ. Press), 105–149.

Berger, W.H., 1970. Planktonic foraminifera: selective solution and the lysocline. *Mar. Geol.,* 8:111–138.

Berggren, W.A., Kent, D.V., Swisher, C.C., III, and Aubry, M.-P., 1995. A revised Cenozoic geochronology and chronostratigraphy. *In* Berggren, W.A., Kent, D.V., Aubry, M.-P., and Hardenbol, J. (Eds.), *Geochronology, Time Scales and Global Stratigraphic Correlation.* Spec. Publ.—Soc. Econ. Paleontol. Mineral. (Soc. Sediment. Geol.), 54:129–212.

Bleil, U., and Shipboard Scientific Party, 1995. Report and preliminary results of SONNE cruise SO 86. *Ber. Fachber. Geowiss., Univ. Bremen,* 51.

Blow, W.H., 1969. Late middle Eocene to Recent planktonic foraminiferal biostratigraphy. *In* Brönnimann, P., and Renz, H.H. (Eds.), *Proc. First Int. Conf. Planktonic Microfossils, Geneva, 1967:* Leiden (E.J. Brill), 1:199–422.

Claypool, G.E., and Kvenvolden, K.A., 1983. Methane and other hydrocarbon gases in marine sediment. *Annu. Rev. Earth Planet. Sci.,* 11:299–327.

Droz, L., Rigaut, F., Cochonat, P., and Tofani, R., 1996. Morphology and recent evolution of the Zaire turbidite system (Gulf of Guinea). *GSA Bull.,* 108:253–269.

Eisma, D., and Kalf, J., 1984. Dispersal of Zaire River suspended matter in the estuary and the Angola Basin. *In* Jansen, J.H.F., McCave, I.N., Postma, H., Nienhuis, P.H., and Weber, R.E. (Eds.), *Quaternary Geology*

and Oceanography of the Zaire Deep-sea Fan and Adjacent Atlantic. Neth. J. Sea Res., 17:385–411.

Eisma, D., and van Bennekom, A.J., 1978. The Zaire River and Estuary and the Zaire outflow in the Atlantic Ocean. *Neth. J. Sea Res.* 12:255–272.

Emerson, S., and Hedges, J.I., 1988. Processes controlling the organic carbon content of open ocean sediments. *Paleoceanography,* 3:621–634.

Emery, K.O., Uchupi, E., Phillips, J., Bowin, C., and Mascle, J., 1975. Continental margin off Western Africa: Angola to Sierra Leone. *AAPG Bull.,* 59:2209–2265.

Froelich, P.N., Klinkhammer, G.P., Bender, M.L., Luedtke, N.A., Heath, G.R., Cullen, D., Dauphin, P., Hammond, D., Hartman, B., and Maynard, V., 1979. Early oxidation of organic matter in pelagic sediments of the eastern equatorial Atlantic: suboxic diagenesis. *Geochim. Cosmochim. Acta,* 43:1075–1090.

Gartner, S., 1977. Calcareous nannofossil biostratigraphy and revised zonation of the Pleistocene. *Mar. Micropaleontol.,* 2:1–25.

Hays, J.D., 1965. Radiolaria and late Tertiary and Quaternary history of Antarctic seas. *In* Llano, G.A. (Ed.), *Biology of the Antarctic Seas II.* Antarct. Res. Ser., 5:125–184.

Hays, J.D., and Opdyke, N.D., 1967. Antarctic radiolaria, magnetic reversals, and climate change. *Science,* 158:1001–1011.

Heezen, B.C., Menzies, R.J., Schneider, E.D., Ewing, W.M., and Granelli, N.C.L., 1964. Congo submarine canyon. *AAPG Bull.,* 48:1126–1149.

Jansen, J.H.F., 1985. Middle and Late Quaternary carbonate production and dissolution, and paleoceanography of the eastern Angola Basin, South Atlantic Ocean. *In* Hsü, K.J., and Weissert, H.J. (Eds.), *South Atlantic Paleoceanography:* Cambridge (Cambridge Univ. Press), 25–46.

————, 1990. Glacial-interglacial oceanography of the southeastern Atlantic Ocean and the paleoclimate of west central Africa. *In* Lanfranchi, R., and Schwartz, D. (Eds.), *Paysages Quaternaires de l'Afrique Centrale Atlantique:* Paris (Editions ORSTOM), 110–123.

Jansen, J.H.F., Alderliesten, C., Houston, C.M., De Jong, A.F.M., Van der Borg, K., and Van Iperen, J.M., 1989. Aridity in equatorial Africa during the last 225,000 years: a record of opal phytoliths/freshwater diatoms from the Zaire (Congo) deep-sea fan (northeast Angola basin). *Radiocarbon,* 31:557–569.

Jansen, J.H.F., Kuijpers, A., and Troelstra, S.R., 1986. A mid-Brunhes climatic event: long-term changes in global atmospheric and ocean circulation. *Science,* 232:619–622.

Jansen, J.H.F., and Van Iperen, J.M., 1991. A 220,000-year climatic record for the east equatorial Atlantic Ocean and equatorial Africa: evidence from diatoms and opal phytoliths in the Zaire (Congo) deep-sea fan. *Paleoceanography,* 6:573–591.

Jansen, J.H.F., van Weering, T.G.E., Gieles, R., and van Iperen, J., 1984. Middle and late Quaternary oceanography and climatology of the Zaire-Congo fan and the adjacent eastern Angola Basin. *Neth. J. Sea Res.,* 17:201–241.

Kling, S.A., 1973. Radiolaria from the eastern North Pacific, Deep Sea Drilling Project, Leg 18. *In* Kulm, L.D., von Huene, R., et al., *Init. Repts. DSDP,* 18: Washington (U.S. Govt. Printing Office), 617–671.

Lombari, G., and Boden, G., 1985. Modern radiolarian global distributions. *Spec. Publ. Cushman Found. Foraminiferal. Res.,* 16A.Martini, E., 1971. Standard Tertiary and Quaternary calcareous nannoplankton zonation. *In* Farinacci, A. (Ed.), *Proc. 2nd Int. Conf. Planktonic Microfossils Roma:* Rome (Ed. Tecnosci.), 2:739–785.

McIver, R.D., 1975. Hydrocarbon occurrences from JOIDES Deep Sea Drilling Project. *Proc. Ninth Petrol. Congr.,* 269–280.

Meyers, P.A., 1994. Preservation of elemental and isotopic source identification of sedimentary organic matter. *Chem. Geol.,* 144:289–302.

————, 1997. Organic geochemical proxies of paleoceanographic, paleolimnologic, and paleoclimatic processes. *Org. Geochem.,* 27:213–250.

Meyers, P.A., and Brassell, S.C., 1985. Biogenic gases in sediments deposited since Miocene times on the Walvis Ridge, South Atlantic Ocean. *In* Caldwell, D.E, Brierley, J.A., and Brierley, C.L. (Eds.), *Planetary Ecology:* New York (Van Nostrand Reinhold), 69–80.

Meyers, P.A., and Shaw, T.J., 1996. Organic matter accumulation, sulfate reduction, and methanogenesis in Pliocene–Pleistocene turbidites on the Iberian Abyssal Plain. *In* Whitmarsh, R.B., Sawyer, D.S., Klaus, A., and Masson, D.G. (Eds.), *Proc. ODP, Sci. Results,* 149: College Station, TX (Ocean Drilling Program), 705–712.

Meyers, P.A., and Snowdon, L.R., 1993. Sources and migration of methane-rich gas in sedimentary rocks on the Exmouth Plateau: northwest Austra-

lian continental margin. *In* Oremland, R.S. (Ed.), *Biogeochemistry of Global Change:* New York (Chapman and Hall), 434–446.

Millero, F.J., and Sohn, M.L., 1992. *Chemical Oceanography:* Boca Raton (CRC Press).

Mix, A.C., Rugh, W., Pisias, N.G., Veirs, S., Leg 138 Shipboard Sedimentologists (Hagelberg, T., Hovan, S., Kemp, A., Leinen, M., Levitan, M., Ravelo, C.), and Leg 138 Scientific Party, 1992. Color reflectance spectroscopy: a tool for rapid characterization of deep-sea sediments. *In* Mayer, R., Pisias, N., Janecek, T., et al., *Proc. ODP, Init. Repts.,* 138 (Pt. 1): College Station, TX (Ocean Drilling Program), 67–77.

Moore, T.C., Jr., 1995. Radiolarian stratigraphy, Leg 138. *In* Pisias, N.G., Mayer, L.A., Janecek, T.R., Palmer-Julson, A., and van Andel, T.H. (Eds.), *Proc. ODP, Sci. Results,* 138: College Station, TX (Ocean Drilling Program), 191–232.

Müller, P.J., 1977. C/N ratios in Pacific deep sea sediments: effect of inorganic ammonium and organic nitrogen compounds sorbed by clays. *Geochim. Cosmochim. Acta,* 41:765–776.

Müller, P.J., and Schneider, R., 1993. An automated leaching method for the determination of opal in sediments and particulate matter. *Deep-Sea Res.,* 40:425–444.

Nigrini, C., 1991. Composition and biostratigraphy of radiolarian assemblages from an area of upwelling (northwestern Arabian Sea, Leg 117). *In* Prell, W.L., Niitsuma, N., et al., *Proc. ODP, Sci. Results,* 117: College Station, TX (Ocean Drilling Program), 89–126.

Okada, H., and Bukry, D., 1980. Supplementary modification and introduction of code numbers to the low-latitude coccolith biostratigraphic zonation (Bukry, 1973; 1975). *Mar. Micropaleontol.,* 5:321–325.

Olausson, E., 1984. Oxygen and carbon isotope analyses of a Late Quaternary core in the Zaire (Congo) fan. *Neth. J. Sea Res.,* 17:276–279.

Parker, F.L., 1971. Distribution of planktonic foraminifera in Recent deep–sea sediments. *In* Funnell, B.M., and Riedel, W.R. (Eds.), *The Micropaleontology of Oceans:* Cambridge (Cambridge Univ. Press), 289–308.

Peters, J.J., 1978. Discharge and sand transport in the braided zone of the Zaire Estuary. *Neth. J. Sea Res.,* 12:273–292.

Peters, K.E., 1986. Guidelines for evaluating petroleum source rock using programmed pyrolysis. *AAPG Bull.,* 70:318–329. Pujos, A., 1988. Spatio-temporal distribution of some Quaternary coccoliths. *Oceanol. Acta,* 11:65–77.

Schneider, R.R., Müller, P.J., Ruhland, G., Meinecke, G., Schmidt, H., and Wefer, G., 1996. Late Quaternary surface temperatures and productivity in the east-equatorial South Atlantic: response to changes in trade/monsoon wind forcing and surface water advection. *In* Wefer, G., Berger, W.H., Siedler, G., and Webb, D. (Eds.), *The South Atlantic: Present and Past Circulation:* Berlin (Springer-Verlag), 527–551.

Schneider, R.R., Müller, P.J., and Wefer, G., 1994. Late Quaternary paleoproductivity changes off the Congo deduced from stable carbon isotopes of planktonic foraminifera. *Palaeogeogr., Palaeoclimatol., Palaeoecol.,* 110:255–274.

Schneider, R.R., Price, B., Müller, P.J., Kroon, D., and Alexander, I., 1997. Monsoon related variations in Zaire (Congo) sediment load and influence of fluvial silicate supply on marine productivity in the east equatorial Atlantic during the last 200,000 years. *Paleoceanography,* 12:463–481.

Shepard, F.P., and Emery, K.O., 1973. Congo submarine canyon and fan valley. *AAPG Bull.,* 57:1679–1691.

Shipboard Scientific Party, 1990. Site 767. *In* Rangin, C., Silver, E.A., von Breymann, M.T., et al., *Proc. ODP, Init. Repts.,* 124: College Station, TX (Ocean Drilling Program), 121–193.

Singer, A., 1984. The paleoclimatic interpretation of clay minerals in sediments: a review. *Earth-Sci. Rev.,* 21:251–293.

Thierstein, H.R., Geitzenauer, K., Molfino, B., and Shackleton, N.J., 1977. Global synchroneity of late Quaternary coccolith datum levels: validation by oxygen isotopes. *Geology,* 5:400–404.

Uenzelmann-Neben, G., Spiess, V., and Bleil, U., 1997. A seismic reconnaissance survey of the Congo Fan. *Mar. Geol.,* 140:283–306.

van Bennekom, A.J., 1996. Silica signals in the South Atlantic. *In* Wefer, G., Berger, W.H., Sieder, G., and Webb, D.J. (Eds.), *The South Atlantic: Present and Past Circulation:* Berlin (Springer-Verlag), 345–354.

van der Gaast, S.J., and Jansen, J.H.F., 1984. Mineralogy, opal, and manganese of Middle and Late Quaternary sediments of the Zaire (Congo) deep-sea fan: origin and climatic variation. *Neth. J. Sea Res.,* 17:313–341.

van Weering, T.C.E., and van Iperen, J., 1984. Fine-grained sediments of the Zaire deep-sea fan, southern Atlantic Ocean. *In* Stow, D.A.V., and Piper,

D.J.W. (Eds.), *Fine-Grained Sediments: Deep Water Processes and Facies:* Oxford (Blackwell), 95–113.

Weaver, P.P.E., 1993. High resolution stratigraphy of marine Quaternary sequences. *In* Hailwood, E.A., and Kidd, R.B. (Eds.), *High Resolution Stratigraphy.* Geol. Soc. Spec. Publ. London, 70:137–153.

Zachariasse, W.J., Schmidt, R.R., and van Leeuwen, R.J.W., 1984. Distribution of foraminifera and calcareous nannoplankton in Quaternary sedi-

ments of the eastern Angola basin in response to climatic and oceanic fluctuations. *Neth. J. Sea Res.*, 17:250–275.

Ms 175IR-103

NOTE: Core-description forms ("barrel sheets") and core photographs can be found in Section 4, beginning on page 581. Forms containing smear-slide data can be found on CD-ROM. See Table of Contents for material contained on CD-ROM.

Table 11. Percentages of inorganic and total carbon, total nitrogen, and total sulfur in sediment samples from Hole 1075A.

Core, section, interval (cm)	Depth (mbsf)	IC (wt%)	CaCO$_3$ (wt%)	TC (wt%)	TOC (wt%)	TN (wt%)	TS (wt%)	C/N (atomic)
175-1075A-								
1H-1, 51-52	0.51	0.11	0.88	2.85	2.74	0.24	0.88	13.3
2H-1, 46-47	1.96	0.67	5.60	3.25	2.58	0.20	1.81	15.0
2H-3, 46-47	4.96	0.17	1.40					
2H-5, 46-47	7.96	0.29	2.39	4.14	3.85	0.30	2.56	15.0
2H-7, 47-48	10.97	0.17	1.39					
3H-1, 47-48	11.47	0.08	0.66	3.13	3.05	0.26	2.56	13.2
3H-3, 47-48	14.47	0.12	1.02					
3H-5, 47-48	17.47	0.12	0.99	3.49	3.37	0.30	1.66	13.1
4H-1, 47-48	20.97	1.51	12.57	4.69	3.18	0.27	1.61	13.7
4H-3, 47-48	23.97	0.87	7.28					
4H-5, 47-48	26.97	0.09	0.75	3.08	2.99	0.26	2.05	13.4
5H-1, 47-48	30.47	0.20	1.64	4.23	4.04	0.31	2.25	15.2
5H-3, 47-48	33.47	0.58	4.80	4.58	4.00	0.22	2.83	21.2
5H-5, 47-48	36.47	2.08	17.32					
6H-1, 47-48	39.97	1.83	15.22	3.41	1.59	0.15	3.74	12.3
6H-3, 47-48	42.97	0.22	1.84	2.32	2.09	0.17	2.02	14.3
6H-5, 47-48	45.97	0.12	0.98					
7H-1, 47-48	49.47	1.86	15.46	4.36	2.50	0.19	2.54	15.4
7H-3, 47-48	52.50	0.05	0.43					
7H-5, 47-48	55.54	0.11	0.94	2.30	2.19	0.19	2.21	13.4
8H-1, 47-48	58.97	0.14	1.16					
8H-3, 47-48	62.02	0.08	0.65	4.50	4.42	0.33	2.71	15.6
8H-5, 47-48	65.06	0.17	1.39					
9H-1, 47-48	68.47	0.27	2.23					
9H-3, 47-48	71.47	0.34	2.85	3.14	2.79	0.22	2.26	14.8
9H-5, 47-48	74.55	0.25	2.04					
10H-1, 47-48	77.97	0.21	1.71					
10H-3, 47-48	80.97	0.42	3.50	2.33	1.91	0.15	2.16	14.9
10H-5, 47-48	83.70	0.78	6.46	3.42	2.65	0.21	2.07	14.7
11H-1, 47-48	87.47	0.53	4.43					
11H-3, 47-48	90.15	1.21	10.07	2.17	0.96	0.17	2.20	6.6
11H-4, 47-48	91.55	0.20	1.67					
12H-1, 47-48	96.97	0.15	1.25					
12H-3, 47-48	99.97	0.17	1.41	3.08	2.91	0.26	2.16	13.1
12H-5, 47-48	103.13	0.15	1.23					
13H-1, 47-48	106.47	0.16	1.34					
13H-3, 47-48	109.47	0.18	1.47	1.91	1.73	0.16	1.54	12.6
13H-5, 47-48	112.47	0.07	0.55					
14H-1, 47-48	115.97	0.25	2.07					
14H-3, 47-48	118.97	0.23	1.92	1.99	1.76	0.17	2.26	12.1
14H-5, 47-48	121.97	0.11	0.89					
15H-3, 47-48	127.35	0.23	1.93	2.81	2.58	0.23	2.19	13.1
15H-5, 47-48	129.95	0.08	0.70					
16H-1, 47-48	134.97	0.32	2.63	1.70	1.38	0.15	2.54	10.7
16H-3, 47-48	137.97	0.09	0.74					
16H-5, 47-48	140.97	0.22	1.84					
17H-1, 47-48	144.47	0.14	1.13					
17H-3, 47-48	147.47	0.13	1.10	1.64	1.51	0.16	11.0	2.79
17H-5, 47-48	150.47	0.23	1.92					
18H-1, 47-48	153.97	0.24	2.03	3.08	2.84	0.23	3.74	14.4
18H-3, 47-48	156.97	0.17	1.41					
18H-5, 47-48	159.70	0.28	2.35					
19H-1, 47-48	163.47	0.15	1.24					
19H-3, 47-48	166.47	0.07	0.56	2.16	2.09	0.19	3.48	12.8
19H-5, 47-48	169.47	0.06	0.51					
20H-3, 47-48	174.88	0.05	0.44	1.70	1.65	0.18	3.08	10.7
20H-5, 47-48	177.88	0.07	0.54	3.74	3.68	0.28	2.92	15.3
21H-1, 47-48	182.47	0.06	0.46					
21H-3, 47-48	185.47	0.07	0.59	3.61	3.54	0.29	3.45	14.2
21H-5, 47-48	188.47	0.07	0.56					
22H-1, 47-48	191.97	0.05	0.39					
22H-3, 47-48	194.97	0.04	0.30	1.47	1.43	0.16	2.53	10.4
22H-5, 47-48	197.97	0.06	0.48					

Notes: IC = inorganic carbon; CaCO$_3$ = calcium carbonate; TC = total carbon; TOC = total organic carbon; TN = total nitrogen; TS = total sulfur; and C/N = carbon/nitrogen ratio. TOC concentrations are calculated from the difference between IC and TC concentrations. C/N ratios are calculated from TOC and TN concentrations and are given as atom/atom ratios.
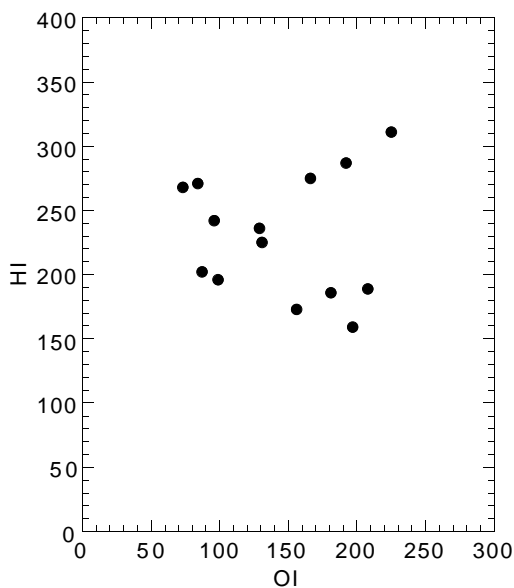
Figure 31. Rock-Eval Van Krevelen–type diagram of sediments from Hole 1075A. Organic matter appears to be a mixture of type II algal material that has been variably oxidized and type III continental or detrital organic matter. HI = milligrams of hydrocarbons per gram of organic carbon; OI = milligrams of CO_2 per gram of organic carbon.

Table 12. Results of Rock-Eval pyrolysis analyses of sediments from Hole 1075A.

Core, section, interval (cm)	Depth (mbsf)	TOC (wt%)	S_1	S_2	S_3	T_{max} (°C)	HI	OI
175-1075A-								
1H-1, 51-52	0.51	2.74	0.76	5.38	2.73	479	196	99
2H-5, 46-47	7.96	3.85	0.86	7.80	3.38	419	202	87
3H-5, 47-48	17.47	3.37	0.81	9.14	2.84	442	271	84
5H-1, 47-48	30.47	4.04	0.71	9.81	3.88	420	242	96
7H-1, 47-48	49.47	2.50	0.50	3.99	4.93	419	159	197
8H-3, 47-48	62.02	4.42	0.89	11.87	3.27	420	268	73
9H-3, 47-48	71.47	2.79	0.67	5.20	5.07	408	186	181
11H-3, 47-48	90.15	0.96	0.28	2.63	4.53	ND	273	471
12H-3, 47-48	99.97	2.91	0.60	6.57	3.83	421	225	131
13H-5, 47-48	112.47	1.73	0.24	3.27	3.61	479	189	208
15H-3, 47-48	127.35	2.58	0.38	4.47	4.03	425	173	156
18H-1, 47-48	153.97	2.84	0.57	6.72	3.67	417	236	129
19H-3, 47-48	166.47	2.09	0.44	5.75	3.49	421	275	166
20H-3, 47-48	174.88	1.65	0.33	4.75	3.17	460	287	192
22H-3, 47-48	194.97	1.43	0.26	4.46	3.22	476	311	225

Notes: TOC = total organic carbon; HI = hydrogen index; and OI = oxygen index. Units of the various Rock-Eval parameters are given in the "Organic Geochemistry" section of the "Explanatory Notes" chapter (this volume).

Table 13. Results of headspace gas analyses of sediments from Hole 1075A.

Core, section, interval (cm)	Depth (mbsf)	C_1 (ppmv)	$C_2=$ (ppmv)	C_2 (ppmv)	C_1/C_2	CO_2 (ppmv)
175-1075A-						
1H-1, 0-5	0.05	2	0.0	0.0		
2H-2, 0-5	3.05	2	0.0	0.0		
2H-3, 0-5	4.55	3	0.0	0.0		
2H-4, 0-5	6.05	4	0.0	0.0		
2H-5, 0-5	7.55	4	0.0	0.0		
2H-6, 0-5	9.05	8	0.0	0.0		
2H-7, 0-5	10.55	5	0.0	0.0		
3H-2, 0-5	12.55	360	0.4	0.2	1,802	
3H-3, 0-5	14.05	445	0.6	0.3	1,485	
3H-4, 0-5	15.55	148	0.4	0.0		
3H-5, 0-5	17.05	734	0.6	0.3	2,448	
3H-6, 0-5	18.55	44	0.2	0.0		
3H-7, 0-5	20.05	228	0.6	0.7	326	
4H-2, 0-5	22.05	56	0.2	1.1	51	
4H-3, 0-5	23.55	36	0.0	0.6	61	
4H-4, 0-5	25.05	531	0.2	1.1	482	
4H-5, 0-5	26.55	399	0.3	1.5	266	
4H-6, 0-5	28.05	92	0.0	1.0	92	
4H-7, 0-5	29.55	228	0.1	1.5	152	
5H-2, 0-5	31.55	4,366	0.7	4.0	1,092	
5H-3, 0-5	33.05	8,012	0.9	4.9	1,635	
5H-4, 0-5	34.55	3,858	0.4	1.8	2,143	
5H-5, 0-5	36.05	4,277	0.3	1.4	3,055	11,884
5H-6, 0-5	37.55	14,706	0.6	4.9	3,001	
5H-7, 0-5	39.05	24,166	0.2	6.6	3,656	
6H-2, 0-5	41.05	14,707	0.7	4.2	3,535	
6H-3, 0-5	42.55	9,991	0.3	2.7	3,700	
6H-4, 0-5	44.05	17,375	0.9	4.5	3,861	
6H-5, 0-5	45.55	12,311	0.4	3.0	4,104	
6H-6, 0-5	47.05	34,767	1.0	7.6	4,575	
6H-7, 0-5	48.55	38,647	0.0	7.5	5,153	
7H-2, 0-5	50.55	26,519	1.0	6.7	3,940	
7H-3, 0-5	52.08	29,415	0.9	7.2	4,085	
7H-4, 0-5	53.62	30,011	0.9	6.7	4,479	
7H-5, 0-5	55.12	37,317	1.1	8.9	4,193	
7H-6, 0-5	56.62	30,739	0.2	6.9	4,455	
7H-7, 0-5	58.12	19,625	0.0	4.4	4,460	
8H-4, 0-5	63.10	57,927	0.2	10.0	5,822	6,106
9H-4, 0-5	72.59	52,587	0.4	9.1	5,779	
10H-4, 0-5	81.85	49,241	0.4	10.1	4,875	18,524
11H-4, 0-5	91.13	48,153	0.4	10.8	4,459	
12H-4, 0-5	101.15	28,591	0.4	7.3	3,917	
13H-7, 0-5	115.05	26,532	0.2	6.5	4,082	
14H-7, 0-5	124.55	23,030	0.4	7.1	3,244	
15H-4, 0-5	128.23	12,717	0.4	4.6	2,765	
16H-7, 0-5	143.55	13,946	0.4	5.6	2,490	
17H-7, 0-5	153.05	22,930	0.4	8.7	2,636	29,209
18H-4, 0-5	157.85	30,732	0.5	10.1	3,043	
19H-7, 0-5	172.05	7,617	0.2	2.9	2,627	7,670
20H-7, 0-5	180.46	12,644	0.8	5.5	2,299	
21H-7, 0-5	191.05	8,805	0.2	4.6	1,914	26,743
22H-7, 0-5	200.55	15,895	1.3	7.1	2,239	

Notes: C_1 = methane; $C_2=$ = ethene; C_2 = ethane; and CO_2 = carbon dioxide. Dominance of C_1 over C_2 indicates that the gases originate from in situ microbial degradation of organic matter.
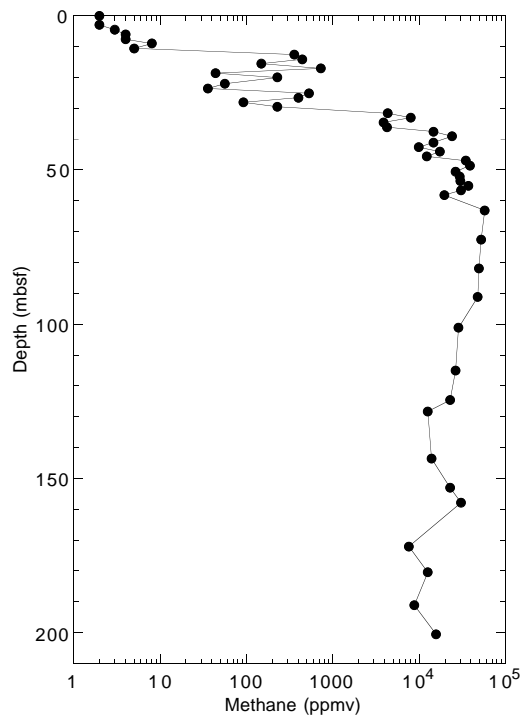
82

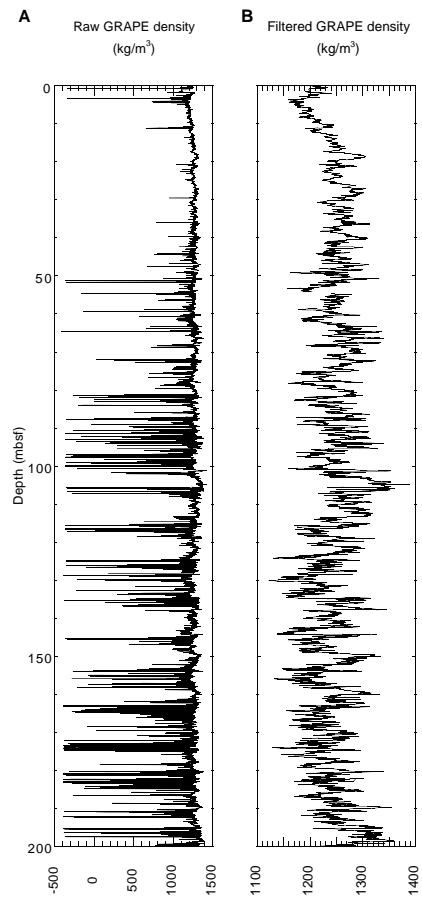Figure 32. Headspace methane concentrations in sediments from Hole 1075A.

Figure 33. Comparison of (**A**) raw GRAPE density data with (**B**) despiked and smoothed data used for further analyses and displays.
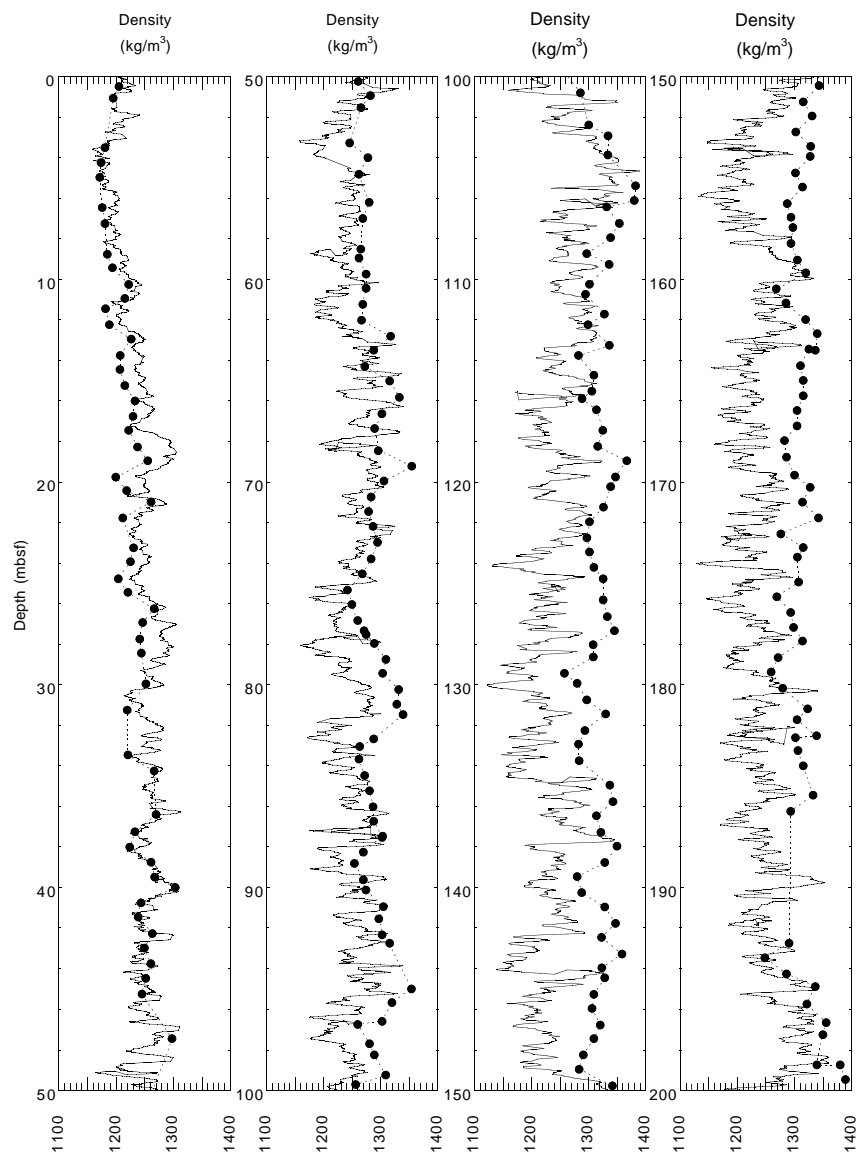
Figure 34. Filtered GRAPE density data (solid line) compared with wet bulk density values (solid circles) obtained from index properties measurements for Hole 1075A.
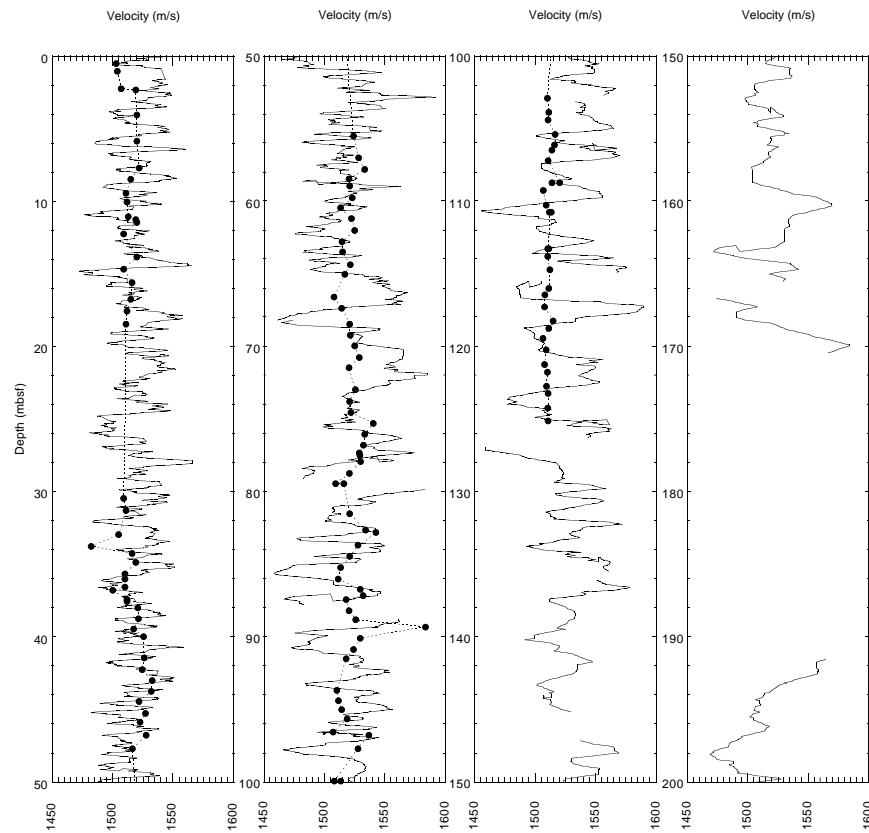
Figure 35. Velocity profiles obtained from MST (solid line) compared with discrete measurements (solid circles) for Hole 1075A.
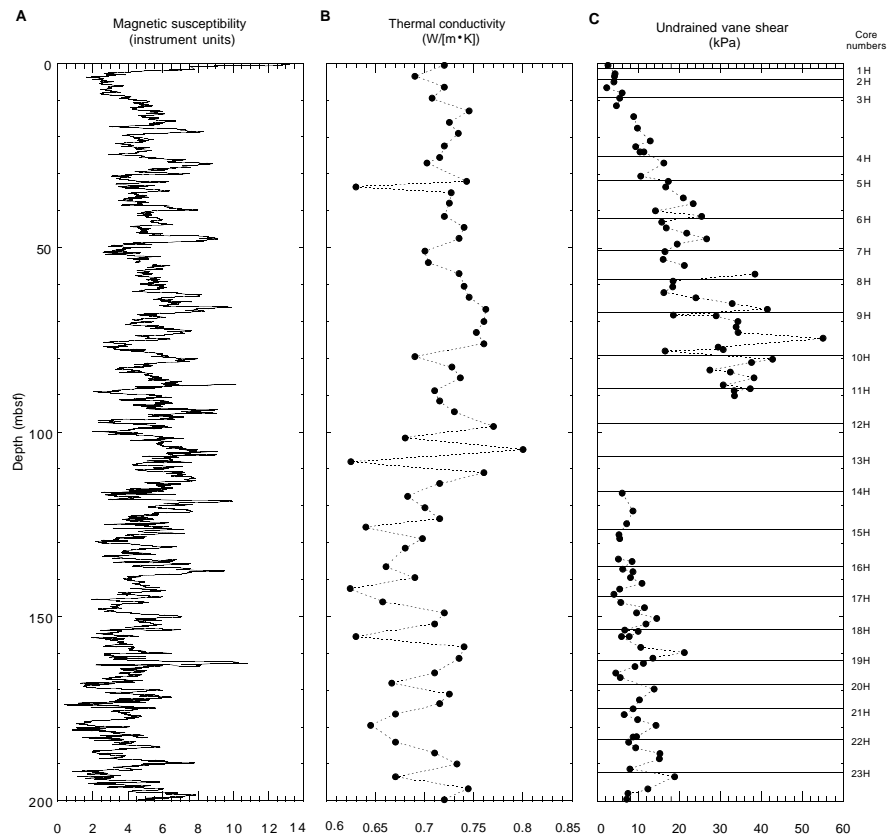

Figure 36. Plots of (**A**) magnetic susceptibility from MST measurements, (**B**) thermal conductivity, and (**C**) vane shear strength for Hole 1075A.
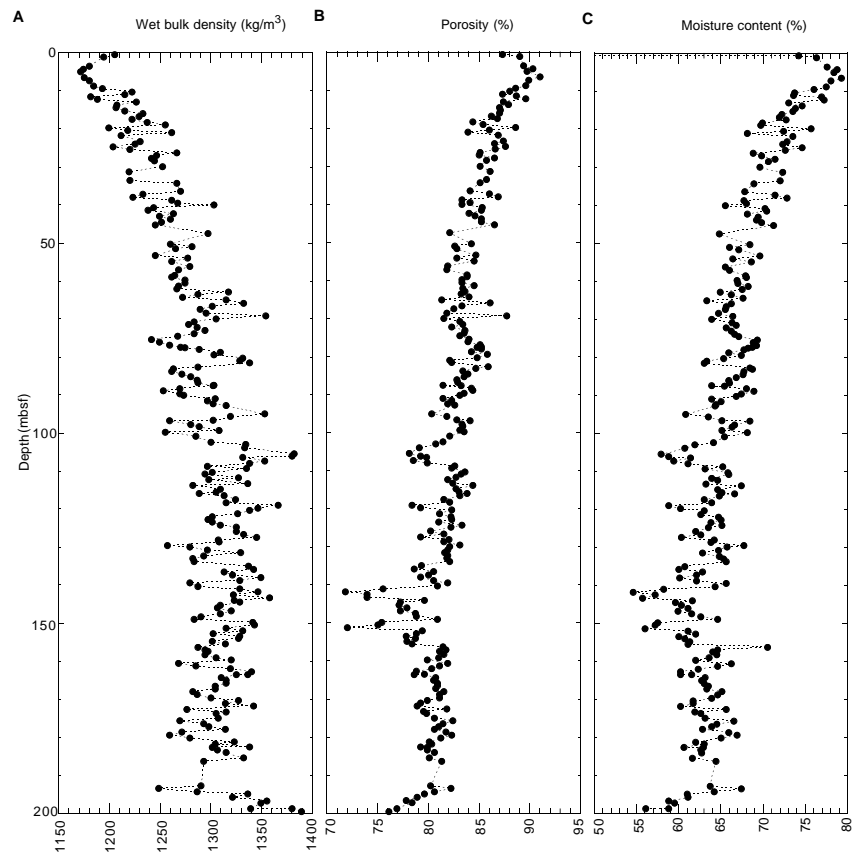
Figure 37. Plots of (**A**) wet bulk density, (**B**) porosity, and (**C**) moisture content derived from index properties measurements for Hole 1075A.